EFFECTS OF PRESSURE GRADIENTS
ON TURBULENT BOUNDARY LAYER FLOW
OVER A FLAT PLATE WITH RIBLETS

THESIS

Franklin L. Dement, Jr., Captain, USAF

AFIT/GAE/ENY/99M-9

Approved for public release; distribution unlimited

19990409 010

The views expressed in this thesis are those of the author and do not reflect the official

policy or position of the Department of Defense or the U. S. Government.

AFIT/GAE/ENY/99M-9

EFFECTS OF PRESSURE GRADIENTS ON TURBULENT BOUNDARY LAYER

FLOW OVER A FLAT PLATE WITH RIBLETS

THESIS

Presented to the Faculty of the Graduate School of Engineering

of the Air Force Institute of Technology

Air Education and Training Command

In Partial Fulfillment of the Requirements for the

Degree of Master of Science in Aeronautical Engineering

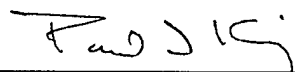Franklin L. Dement, Jr., B.S.A.E.

Captain, USAF

March 1999

EFFECTS OF PRESSURE GRADIENTS ON TURBULENT BOUNDARY LAYER

FLOW OVER A FLAT PLATE WITH RIBLETS

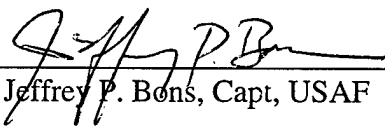Franklin L. Dement, Jr., B.S.A.E.
Captain, USAF

Approved:

_____
Paul I. King, Chairman

_____2/26/99_____
date

_____
Jeffery K. Little, Lt Col, USAF

_____
date

_____
Jeffrey P. Bons, Capt, USAF

_____2/26/99_____
date

occasions. Above all, I must thank my wife, Cynthia, for her endless patience, support, love and encouragement during my AFIT experience. I could have accomplished little without her steadying influence, hard work and personal sacrifices.

This work is dedicated to the most important engineer in my life, Franklin L. Dement, Sr., and to my undergraduate mentor, Dr. George E. Weeks of the University of Alabama Aerospace Engineering Department.

Franklin L. Dement, Jr.

Table of Contents

List of Tables

List of Symbols

<u>Acronyms</u>

AFIT	Air Force Institute of Technology
BLRF	Boundary Layer Research Facility
BSA	Burst Spectrum Analyzer
LDA	Laser Doppler Anemometry
PM	Photo-Multiplier
1-D	One-Dimensional
2-D	Two-Dimensional
3-D	Three-Dimensional

<u>English Symbols</u>

a_x	Acceleration in the x direction (m/s^2)
b	Logarithmic law constant
BW	Bandwidth (kHz)
c_f	Local Skin-Friction Coefficient
$[C]^{-1}$	Laser Probe Alignment Matrix
$[D]$	Optical Misalignment Matrix
d_p	Mean seeding particle diameter (μm)
$[E]$	Optical to Test Section transformation matrix
f_c	Center frequency (kHz)
f_s	Sampling frequency (kHz)
H	Shape factor
h	Riblet height (cm)

h^+	Non-dimensional riblet height
k	Von Karman constant
K	Arbitrary constant
m	Power-law parameter
N	Record length a.k.a. number of samples
p	Pressure (Pa)
P	Laboratory Pressure (Pa)
R	Ideal gas constant for air (kJ/kg·°K)
R_i	Record interval a.k.a. total sampling time (s)
Re_x	Local Reynolds number (based on streamwise coordinate)
Re_θ	Local Reynolds number (based on momentum thickness)
s	Riblet spacing (cm)
s^+	Non-dimensionalized riblet spacing
T	Laboratory Temperature (°F)
T_s	Sampling time (s)
Tu	Turbulence intensity
U	Local freestream velocity (m/s)
u	Streamwise velocity component, test section coordinate system (m/s)
u/U	Velocity ratio
u'	Streamwise velocity fluctuation (m/s)
u_i	Velocity component of the ith particle (m/s)
u_p	Streamwise velocity component, probe coordinate system (m/s)

u_t	Streamwise velocity component, traverse coordinate system (m/s)
$\overline{u}_{weighted}$	Residence time-weighted mean velocity component (m/s)
u^+	Dimensionless inner-law streamwise velocity
$\overline{u}$	Local mean streamwise velocity component (m/s)
v	Normal velocity component, test section coordinate system (m/s)
v'	Normal velocity fluctuation (m/s)
v_p	Normal velocity component, probe coordinate system (m/s)
v_t	Normal velocity component, traverse coordinate system (m/s)
v^*	Friction velocity (m/s)
w	Spanwise velocity component, test section coordinate system (m/s)
w'	Spanwise velocity fluctuation (m/s)
w_p	Spanwise velocity component, probe coordinate system (m/s)
w_t	Spanwise velocity component, traverse coordinate system (m/s)
x	Streamwise coordinate/direction, test section coordinate system (m)
x_p	Streamwise coordinate/direction, probe coordinate system (m)
x_t	Streamwise coordinate/direction, traverse coordinate system (m)
y	Normal coordinate/direction, test section coordinate system (m)
y/δ	Non-dimensional normal distance
y_p	Normal coordinate/direction, probe coordinate system (m)
y_t	Normal coordinate/direction, traverse coordinate system (m)
y^+	Dimensionless inner-law normal coordinate
z	Spanwise coordinate/direction, test section coordinate system (m)
z_p	Spanwise coordinate/direction, probe coordinate system (m)

| z_t | Spanwise coordinate/direction, traverse coordinate system (m) |

Greek Symbols

α	Rotation angle about z_t axis (°)
β	Rotation angle about y_t axis (°), Falkner-Skan pressure gradient parameter
γ	Rotation angle about x_t axis (°)
Δt_i	Transit time of the ith particle (sec)
δ	Boundary layer thickness (mm)
$\delta*$	Displacement thickness (mm)
$\delta_{99\%}$	Boundary layer thickness: y at u = 0.99U (mm)
μ	Dynamic viscosity (μPa·s)
η	Blasius similarity parameter
ρ	Fluid Density (kg/m^3)
θ	Momentum thickness (mm)
θ_1	1-D probe angle (°)
θ_2	2-D probe angle (°)
τ_w	Wall shear stress (μPa)
ν	Kinematic viscosity (m^2/s)

AFIT/GAE/ENY/99M-9

Abstract

The Air Force Institute of Technology Boundary Layer Research Facility test section was modified to create controlled non-zero streamwise pressure gradients. The capability of the modified facility to reproduce theoretical laminar boundary layer velocity profiles and to create a self-preserving flow with an adverse streamwise pressure gradient was verified with three-dimensional laser Doppler anemometry. The effects of streamwise adverse and favorable pressure gradients on turbulent boundary layer flow characteristics (velocity profiles, turbulence and skin friction) and vortex formation over a flat plate with riblets at low speed (U = 5 m/s) were studied.

Normal and spanwise velocity profiles for both pressure gradients showed the presence of paired counter-rotating vortices nested within the riblet valleys. These flow structures increased drag and significantly altered near-wall flow compared to a smooth plate turbulent boundary layer. The adverse pressure gradient tended to degrade these vortices as the flow progressed.

EFFECTS OF PRESSURE GRADIENTS ON TURBULENT BOUNDARY LAYER FLOW OVER A FLAT PLATE WITH RIBLETS

I. Introduction

1.1 Background

A primary, on-going research goal of the aerospace community has been to develop methods to reduce the viscous drag on flight vehicles. Viscous, or skin-friction, drag is a key limiting factor in aircraft performance and fuel economy. Bushnell (1990) indicates, in fact, that viscous drag makes up on the order of 50% of the aerodynamic drag on transport aircraft and 30% to 40% of the aerodynamic drag on high-speed aircraft and missiles. One promising technology to reduce the high toll of viscous drag is riblets. These passive flow control devices are grooves applied to or machined in aerodynamic (or hydrodynamic) surfaces parallel to the flow direction. Research has shown that riblets can reduce viscous drag on the order of 6% to 8% (Walsh, 1990). Although this amount of drag reduction does not initially appear significant, Bushnell (1990) states that the annual potential savings for the domestic airline fleet could be on the order of half a billion dollars.

The majority of riblet research to date has focused on the application of riblets to viscous drag reduction on external surfaces of aircraft and marine vessels. With the exception of research work at the Air Force Institute of Technology (AFIT), little emphasis has been placed on the use of riblets for internal flow control. Heat transfer, transition, flow separation and skin-friction drag over internal engine surfaces such as

diffusers, stators, nozzles and compressor and turbine blades are affected by boundary layer flow structure. The application of riblets to alter boundary layer flow structure for the reduction of engine secondary flow losses has been the motivation for riblet research at AFIT. This research is a continuation of this line of interest.

Recent research at AFIT by Rothenflue (1996) has examined the effects of riblets on the formation of Görtler vortices over a constant-radii, concave surface in laminar and transitional flows. Görtler vortices are weak streamwise vortices that develop close to concave surfaces as a result of centrifugal instabilities. These disturbances, although weak, can profoundly affect boundary layer heat transfer, transition location and skin-friction drag. Rothenflue (1996) found that riblets, which introduce a spanwise periodic disturbance into the boundary layer, can accelerate or delay the formation of these vortices. Consequently, riblets can be used to control Görtler vortex formation and positively impact boundary layer characteristics, flow losses and drag.

The work of Rothenflue (1996) was an important first step toward the use of riblets to reduce engine flow losses. His experiments were performed with flat and constant radii concave test surfaces subjected to a zero streamwise pressure gradient. These conditions, however, do not fully model the complex surface geometries and flow characteristics present in an actual engine. Out of necessity, his experiments were simplified to examine boundary layer effects as a result of only variations in flow velocity. The purpose of this project was to extend this line of inquiry to examine how non-zero pressure gradient flows over a riblet surface affect turbulent boundary layer flow. In order to examine only pressure gradient effects, only flow over a flat, riblet plate

2

was examined. In addition, self-preserving flows were incorporated to examine flow effects independent of streamwise coordinate.

1.2 Project Objectives

This research had four objectives. The first objective was to modify the AFIT Boundary Layer Research Facility (BLRF) to produce specific non-zero streamwise pressure gradients. The second objective was to verify the ability of the modified facility to successfully produce theoretical boundary layer profiles and useful streamwise pressure gradients. The third objective of this research was to use the modified facility to perform initial studies on the effects of pressure gradients on turbulent flow over a flat, riblet plate. The final objective was to recommend future research directions as well as facility and procedural improvements.

To facilitate comparisons and to meet research time constraints, much of the apparatus of Rothenflue (1996) was used. Common hardware included the flat, riblet and flat, smooth test plates, the majority of the BLRF hardware, the AFIT 100-psi laboratory air supply and the three dimensional (3-D) laser Doppler anemometry (LDA) system. Since the original test section was not well suited for the creation of streamwise pressure gradients, a new test section was designed and built. Streamwise pressure gradients were produced through the adjustment of the new flexible test section sidewalls.

The capabilities of the new test section were validated through the duplication of the Blasius solution for a smooth plate and the production of a self-preserving adverse pressure gradient flow. The self-preserving adverse pressure gradient flow was chosen with a streamwise power-law velocity distribution that corresponded to a Falkner-Skan pressure gradient parameter, β, of -0.15. Also as part of the facility verification process,

the turbulence generation characteristics of the sidewall laser passage slot were studied as recommended by Rothenflue (1996).

The effects of pressure gradients on turbulent boundary layer flow characteristics, nested riblet-valley vortex formation, and skin-friction drag over the riblet test plate surface were examined through the acquisition and analysis of velocity and turbulence profiles. These profiles were acquired and processed with a non-intrusive 3-D laser Doppler anemometry (LDA) system. The LDA traverse system combined with the 3-D off-axis LDA probe configuration provided the high spatial resolution needed for detailed descriptions of boundary layer and riblet-valley vortical flow structures.

Velocity and turbulence data were collected at two streamwise stations for favorable and adverse pressure gradient flows over the riblet test plate. Test section inlet velocity was approximately 5 m/s for both cases. Flow characteristics of interest included boundary layer thickness, boundary layer flow state, normal and spanwise velocity distributions, local skin-friction coefficients, and vortex size, shape and strength. Riblet plate turbulent flow characteristics were compared to smooth plate turbulent flow characteristics. The comparisons included an examination of the near-wall flow region and skin-friction drag performance.

The four objectives of this research were met.

1.3 Thesis Overview

This research is presented in several sections. First, the effects of riblets on boundary layer flow are presented. This section includes discussion of riblet effects in the presence and absence of pressure gradients, the findings of Rothenflue (1996), characteristics of nested riblet-valley vortices and expected observations for this research.

The experimental apparatus and procedures are then presented followed by a discussion of the acquired data. The final section of the thesis contains the conclusions drawn from the data and recommendations for future research. Appendices to the thesis include detailed discussions on test equipment and configuration, low laser power and steady flow problems, acquisition software parameters and data post-processing.

II. Riblet-Boundary Layer Interactions

2.1 Overview

In this chapter, riblets and their effects on turbulent boundary layer flow and skin-friction drag are discussed along with the anticipated effects from non-zero pressure gradients.

2.2 Riblet Description

Riblets are passive flow control devices applied to or machined into aerodynamic and hydrodynamic surfaces. A variety of riblet shapes, as shown in the cross-sectional view of Figure 1, have been studied. In the figure, s is the riblet spacing and h is the riblet height. Of these shapes, the V-groove (the uppermost example) is the most common and most widely tested (Walsh, 1990). This configuration was used by Rothenflue (1996) and in this research and is subsequently the main subject in the following discussion.

2.3 Riblet-Boundary Layer Interactions

Flows over surfaces with riblets exhibit significant differences in near-wall boundary flow structure and characteristics than flows over smooth surfaces. A significant source of the differences, as observed by Rothenflue (1996), can be the formation and sustained presence of pairs of counter-rotating streamwise vortices nested within the riblet valleys. This phenomenon is illustrated in the cross-sectional view of Figure 2. The formation of these vortices is a result of the interaction of viscous effects and, for curved surfaces, centrifugal effects, close to the riblet surface. Suzuki and

Kasagi (1994) observed similar phenomena in their particle tracking velocimetry measurements of zero pressure gradient flow over drag-augmenting riblets. The formation of these vortices is significantly influenced by riblet geometry and flow conditions such as velocity and pressure gradient. The vortices promote the transport of fluid particles within the boundary layer. This transport causes increased mixing and transfer of momenta and the resultant differences from smooth plate flow in boundary layer flow structure and characteristics.

The presence of paired, counter-rotating riblet-valley vortices, however, is not universal for flows over riblet surfaces. As described by Walsh (1990), streamwise vortices are virtually absent in turbulent flows where skin-friction is reduced compared to smooth plate flows. The effects of riblets on skin-friction drag are discussed in Section 2.3.2, <u>Riblet Effects on Drag</u>.

2.3.1 <u>Riblet-Görtler Vortex Interactions</u>. The nested vortices illustrated in Figure 2 are of interest due to their similarity to Görtler vortices. Görtler vortices are the weak pairs of counter-rotating streamwise vortices that develop over concave surfaces in response to centrifugal instabilities. Despite their weak nature, these vortices adversely affect boundary layer characteristics. Görtler vortices destabilize the laminar boundary layer in the upwash region between two counter-rotating vortices through momentum transport (Floryan, 1991). This destabilization results in premature boundary layer transition and increased skin-friction drag. Barlow and Johnson (1985) found that Görtler vortices can increase local skin-friction drag by up to 20% to 40% over flat plate values. In addition, Görtler vortices can also develop in turbulent boundary layers over walls of relatively high curvature similar to those on the pressure surfaces of turbine

blades (Floryan, 1991). Consequently, the delay of Görtler vortex formation would be beneficial to the reduction of losses over internal engine surfaces.

Due to their ability to limit the formation of longitudinal vortices, riblets are one possibility for the control of Görtler vortex formation over curved internal engine surfaces. The influence of riblets on longitudinal vortex formation is a result of their effects on near-wall flow structure. Coustols and Savill (1992) state that the spanwise movement of low speed fluid characterizes flow within the turbulent boundary layer laminar sublayer. Walsh (1990) states that the development of longitudinal vortices is constrained by the ability of riblets to resist this spanwise fluid movement near the wall. This has been experimentally verified by Suzuki and Kasagi (1994).

The riblet research discussed above was conducted with flat plates (zero wall curvature). In fact, the majority of riblet research to date has involved flat plates. Recent research at AFIT by Rothenflue (1996) with a curved riblet plate has shown the relevance of riblets to internal engine flows. He found that riblets introduce a spanwise periodic disturbance in the boundary layer that can interact with the Görtler instability. Given the appropriate flow conditions and riblet geometry, Görtler vortex formation can be either accelerated or delayed with riblets.

The conclusions regarding riblet effects and Görtler vortex formation were reached through the study of zero pressure gradient flows. Floryan (1991) notes that most Görtler vortex research to date has been performed with zero pressure gradient flows over a wall with constant curvature in order to minimize the number of experimental variables. Realistic applications of riblets, however, will involve pressure gradients. Görtler vortex formation in non-zero pressure gradients has been studied by

8

Kalburgi et al. (1989). He found that the de-stabilizing effects of adverse pressure gradients cause Görtler vortices to develop more rapidly and the stabilizing effects of favorable pressure gradients tend to inhibit Görtler vortex development. Unfortunately, no information is currently available on the effects of riblets on Görtler vortex formation in non-zero pressure gradients. It is anticipated that the ability of riblets to affect Görtler vortex formation will depend on both riblet geometry (shape and dimensions) and flow conditions such as boundary layer state, flow velocity and pressure gradient magnitude.

Prior to examination of Görtler vortex formation in a non-zero pressure gradient flow over a curved riblet plate, it is beneficial to study the effects of non-zero pressure gradient flows on the nested riblet-valley vortices that form over a flat plate. This is necessary to examine the effects of non-zero pressure gradients independent of the centrifugal instabilities created by non-zero wall curvature. Results of this study should qualitatively presage the results to be expected for Görtler vortex formation in a non-zero pressure gradient flow over a curved riblet surface.

2.3.2 Effects on Skin-Friction Drag. Riblets were not initially developed as a mechanism for Görtler vortex formation control. The main motivation for riblet research has been the reduction of skin-friction drag in turbulent boundary layers. Walsh (1990) provides an excellent synopsis on this subject. In comparison, comparatively little emphasis has been placed on viscous drag reduction in laminar boundary layers. This is a result of the increase of skin-friction drag by nearly an order of magnitude in a turbulent boundary layer compared to a laminar boundary layer (White, 1991).

The magnitude of turbulent flow skin-friction drag reduction available with riblets is variable. Walsh (1990) states that drag reduction is highly dependent on riblet shape

9

and dimensions and the boundary layer state. With regards to size, drag reduction decreases as the height and spacing of the riblets increase in wall units due to the overwhelming penalty associated with the increase in wetted surface area. With V-grooves, Walsh (1990) estimates the maximum available drag reduction as approximately 6% to 8%. Riblets sized for optimum drag reduction, according to Young (1989) have an aspect ratio (s/h) of approximately 1 to 2 with a non-dimensional riblet height (h^+) of approximately 10 to 15. Non-dimensional wall height, as presented by Young (1989), is

$$h^+ = \frac{h v^*}{v} \qquad (1)$$

where v^* is the friction velocity and v is the kinematic viscosity. The friction velocity, v^*, as presented by White (1991), is defined as

$$v^* = \left(\frac{\tau_w}{\rho} \right)^{\frac{1}{2}} \qquad (2)$$

The wall shear stress, τ_w, as presented by White (1991), is defined as

$$\tau_w = \mu \frac{\partial u}{\partial y} \bigg|_{y=0} \qquad (3)$$

At full-scale Reynolds number, riblets sized for viscous drag reduction are on the order of 0.05 mm in height (Young, 1989). In this experiment, non-dimensional riblet height was found to fall within the range $32.89 \leq h^+ \leq 54.96$. As a result, drag reduction was not anticipated.

Walsh (1982) indicates that optimal skin-friction drag reduction is also dependent on dimensionless riblet spacing, s^+. As presented by Young (1989), this is defined as

10

$$s^+ = \frac{sv^*}{v} \qquad (4)$$

Specifically, optimum drag reduction is obtained with $s^+ \leq 25$. As indicated by Bechert and Bartenwerfer (1989), riblets sized with this s^+ are almost completely embedded in the viscous sublayer. They further indicate that drag augmentation will occur if the riblets protrude too far into the boundary layer. In this experiment, non-dimensional riblet spacing was found to fall within the range $37.29 \leq s^+ \leq 63.42$. Consequently, drag reduction was not anticipated.

Shape is also an important contributor to the skin-friction drag reduction capabilities of riblets. To date, various researchers have tested a wide variety of riblet configurations with varying degrees of success. These have included rectangular, V-grooved, razor blades, semi-circular grooved, alternating transverse curvature, trapezoidal-grooved and U-grooved configurations. Both Walsh (1982) and Bechert and Bartenwerfer (1989) state that optimal drag reduction is achieved with riblets possessing sharp peaks and significant valley curvature. The majority of riblet research, however, has been conducted with the V-grooved configuration due to its good drag reduction performance and ease of fabrication.

Turbulent flow skin-friction drag reduction with riblets is accomplished by the adjustment of the near-wall flow to the riblet surface (Djenidi and Antonia, 1996). With appropriately sized riblets, turbulent flow over a riblet surface is essentially two-dimensional (2-D) and can be modeled by a relatively thick turbulent layer that slides along a much thinner viscous region. This essentially is a removal of the no-slip condition for the turbulent layer. This description agrees with the discussion of Walsh (1990) who states that the presence of riblets can create regions of low speed, low skin-

11

friction flow in the riblet valleys. In order to be effective, however, this local skin-friction reduction in the riblet valley area must more than offset the drag penalties from the relatively large shear stress observed at the riblet peaks and the increased wetted surface area (Vukoslavcevic et al., 1992).

As implied above, riblets do not universally reduce skin-friction drag. Flows for which vortices are present near the riblet surface are more likely to increase skin-friction drag. As mentioned previously, particle tracking velocimetry measurements by Suzuki and Kasagi (1994) showed the presence of vortical flow structure nested in the riblet valleys for drag-augmenting riblets. These vortices increased momentum transport within the lower strata of the boundary layer and negated any potential drag reduction. This is contrasted by the observations for drag-reducing riblets where vertical flux of streamwise momentum is significantly reduced within the riblet valley (Park and Wallace, 1994). Djenidi and Antonia (1996) also observed counter-rotating vortices in the vicinity of the riblets and found the vortical motion to be more intense for drag-augmenting riblets.

Rothenflue (1996) observed a similar phenomenon in transitional and laminar boundary layers. Specifically, he observed that skin-friction was increased in all his flat plate test cases by the addition of riblets. He attributed the increase in skin-friction drag to the increase in wetted surface area of the riblet plate compared to a smooth surface. Given that this experiment was conducted with the same riblet plate at similar flow velocities, increases in skin-friction drag compared to a flat plate were anticipated.

The majority of skin-friction measurements for riblet plate flows have been obtained in flat plate, zero pressure gradient flows. This has been the result of the need to

12

reduce the number of experimental variables. In fact, the only existing theoretical predictions for riblet flows are for zero pressure gradient flows (Floryan, 1990). The limited amount of viscous drag reduction data for non-zero pressure gradients, according to Walsh (1990), is contradictory due to measurement difficulties and the inherent inaccuracy in using momentum thickness to calculate skin-friction drag. Recent studies have indicated, however, that riblets are significantly more effective in adverse pressure gradients. For example, Sundaram et al. (1996) have demonstrated a skin-friction drag reduction of as much as 16% at moderate angles of attack for riblets (h = 0.152 mm) applied to a NACA 0012 airfoil. In their experiment, riblets were applied to both the pressure and suction sides of the airfoil. Mean velocity profiles showed that a larger contribution to drag reduction resulted from the suction (adverse pressure gradient) side of the airfoil. In addition, Debisschop and Nieuwstadt (1996) observed a 13% skin-friction drag reduction for symmetric V-grooved riblets (h = 0.36 mm) in a moderate adverse pressure gradient.

2.3.4 <u>Near-Wall Flow Effects</u>. To date, the flow structure near riblet surfaces and inside riblet valleys is not well understood. This is a result of the focus to measure skin-friction drag reductions, the size of riblets under study and the measurement techniques. As discussed above, riblets sized for optimum drag reduction are generally extremely small and the measurement of velocity profiles within their riblet valleys has been impractical with intrusive techniques. In recent research, measurement of flow over riblet surfaces has been accomplished with methods more sophisticated than traditional pitot tubes and hot-wire anemometers. Besides Rothenflue (1996), Djenidi and Antonia (1996) acquired velocity measurements over a flat, riblet plate with 3-D LDA. In

addition, Suzuki and Kasagi (1994) conducted particle tracking velocimetry measurements over a riblet surface.

From the results of Rothenflue (1996), the near-wall flow structure for a drag-augmenting riblet surface differs significantly from flow over a smooth plate. The results of Djenidi and Antonia (1996) agree with this conclusion. They found that the structural changes in the drag-augmenting regime extend some distance into the flow and should reflect the vortical strength in the wall region.

In contrast, Djenidi and Antonia (1996) also found little boundary layer flow changes between smooth and riblet surfaces in the drag reduction regime, with the exception of the viscosity-dominated near-wall region. In fact, this observation is well documented by a number of researchers. Sundaram et al. (1996), Suzuki and Kasagi (1994), Hooshmand et al. (1983) and others have observed a noticeable reduction in turbulence intensity in the wall region for drag-reducing riblets. In this research, significant near-wall structural changes were anticipated based on the drag-augmenting characteristics of the given riblets.

In order to compare the anticipated flow structure differences between the riblet flows under consideration and smooth plate turbulent flow, the acquired velocity profiles were compared to the Law of the Wall. For smooth plate turbulent flow, Young (1989) states that the flow structure consists of an inner viscous sublayer, a buffer layer, and an outer layer. These regions are not sharply distinct and their boundaries vary with flow conditions such as pressure gradients. The inner viscous sublayer consists approximately of the 1% of the boundary layer closest to the flow surface and is dominated by viscous shear stresses. In this region, the mean velocity is practically linear with y (normal

distance). Immediately above the viscous sublayer is the buffer layer. In this region, according to White (1991), the velocity profile is neither linear nor logarithmic but a smooth merge between the two. In this region, the flow structure is impacted both by viscous and eddy, or Reynolds, stresses. Together, the viscous sublayer and buffer layer are known as the Law of the Wall region.

Empirical relations such as Spalding's (1961) equation can accurately describe the smooth plate turbulent flow velocity profile in the Law of the Wall region:

$$y^+ = u^+ + e^{-kb}\left[e^{ku^+} - 1 - ku^+ - \frac{\left(ku^+\right)^2}{2} - \frac{\left(ku^+\right)^3}{6}\right] \qquad (5)$$

In this equation, k is the Von Karman constant and b is the logarithmic constant. The values used for the Von Karman constant, k, and the logarithmic constant, b, were 0.41 and 5.0, respectively. The quantities y^+ and u^+ are dimensionless versions of the normal distance from the wall and the local freestream velocity, respectively. These inner-law variables, as presented by White (1991), are

$$u^+ = \frac{\overline{u}}{v*} \qquad (6)$$

and

$$y^+ = \frac{yv*}{v} \qquad (7)$$

where v* is the friction velocity as previously defined. The quantity $\overline{u}$ is the local mean streamwise velocity component. Spalding's (1961) equation provides a good fit to smooth plate experimental data in the region $35 \leq y^+ \leq 350$ (White, 1991).

The near-wall non-zero pressure gradient flow for a riblet surface should differ significantly from that described by Spalding's (1961) equation when riblet-valley

vortices or Görtler vortices are present. The presence of vortices implies vigorous mixing, transfer of momenta and the influence of eddy stresses nearer the surface than that experienced over a smooth, flat plate. These flow structure differences are implied by Walsh (1990) who states that flow structure changes are not dramatic when riblets operate in drag-reduction regimes where no vortices are present. Non-dramatic flow structure above riblets in drag-reduction regimes appears intuitive since the action of riblets in a viscous drag reduction mode is to create a low-speed, low viscous drag near-wall flow. Walsh (1990) also states that flow structure changes often appear greater in regimes where the riblets increase drag. To facilitate comparison, the u and y values acquired in this experiment recast in non-dimensional form with Equations (6) and (7), respectively.

Vortical flow structure including size, shape, strength and rotational flow pattern is also of interest. With regards to the rotational flow pattern, Rothenflue (1996) was able to determine that the rotational flow pattern illustrated in Figure 2 is not random. Specifically, he observed that the nested vortices rotated such that a local upwash was generated near the riblet peaks and a local downwash occurred directly above the riblet valleys. This pattern is confirmed by Suzuki and Kasagi (1994) and Djenidi and Antonia (1996). Rothenflue (1996) deduced this rotational pattern from the regular variations of cross-flow velocity components (v and w) in profiles acquired in the spanwise direction. He found the v component to vary spanwise in a periodic fashion with a wavelength equal to the riblet spacing. Maximum upwash (+v) occurred at the riblet peak and maximum downwash (-v) occurred at the riblet valley. The w component exhibited a similar periodic pattern but was shifted in phase by 90°. The value of w approaches zero

at the peaks and valleys and indicates the turning of the flow within the vortex to the normal (y) direction. This rotational pattern was further supported by v profiles acquired in the normal direction at the valley and peak spanwise locations. These profiles consistently showed an upwash at the peak and a downwash at the valley location.

Less is known with regards to the size, shape and strength of riblet-valley vortices. Rothenflue (1996) observed sustained riblet-valley vortices that extended approximately 1.5-2.0 mm above the plane of the riblet peaks. These vortices were observed to remain a constant size as the flow progressed. The physically unconstrained upper portion of the vortices appears to be influenced by riblet shape and size. Based on the dimensions of his riblets, the upper portion of the nested vortices he observed appeared to be oval-shaped. Rothenflue (1996) unfortunately did not acquire data to indicate the shape of the vortices within the riblet valleys. However, this portion of the vortices is physically constrained by the riblet valley and, consequently, the flow structure should explicitly depend on riblet geometry and follow the given contour. This agrees with the vortices observed by Suzuki and Kasagi (1994).

With regards to riblet-valley vortex strength, Rothenflue and King (1995) found that maximum v and w components were approximately 4% of the freestream velocity. The riblet-valley vortices observed by Suzuki and Kasagi (1994) reached a maximum strength of 0.8% of the freestream velocity. This data, as well as that on vortex shape, was acquired in a zero pressure gradient flow. No data was available on vortex strength in a non-zero pressure gradient.

17

III. Experimental Apparatus and Procedures

3.1 Overview

The experimental apparatus consisted mainly of two systems: the AFIT Boundary Layer Research Facility (BLRF) and a DANTEC 3-D laser Doppler anemometry (LDA) system. Since this project was an extension of Rothenflue (1996), the following discussion focuses on those components that were subsequently added or modified. A detailed list of equipment is found in Appendix A, Test Apparatus.

The experimental procedure consisted of the initial configuration of the test hardware, the establishment of test conditions and the acquisition and reduction of data. The test procedures accomplished on a daily basis are discussed in this chapter. The initial configuration of the test hardware and associated problems are primarily discussed in the appendices.

3.2 Boundary Layer Research Facility

The BLRF created the desired flow conditions and provided a mount for the injection of seeding particles for velocity measurements. The BLRF was designed and fabricated by Rothenflue (1996) and consisted of three main components: the air supply, the stilling chamber and the test section. A representation of the BLRF is shown in Figure 3. The design of the tunnel is thoroughly discussed by Rothenflue (1996). The BLRF could achieve local Reynolds numbers, Re_x, of up to 430,000 at the exit of the 1 m test section, a maximum steady test section inlet velocity of 6.5 m/s and a maximum steady mass flow rate of approximately 0.45 kg/s (1 lbm/s).

3.2.1 <u>Air Supply</u>. The AFIT shop air system supplied air to the BLRF. The shop air system consisted of two Atlas air compressors and their accompanying reservoir tanks, the flow control hardware and the inlet plumbing. Surging flow was avoided by keeping both compressors in continuous operation and venting the excess mass flow rate above that required for the desired test condition. Both compressors began operation when the pressure in the reservoir tanks fell below 634.3 kPa (92 psi) and discontinued operation at a pressure of approximately 827.4 kPa (120 psi).

3.2.1.1 <u>Flow Control Hardware</u>. The flow control hardware consisted of a flow regulator, a vent valve, a purge valve, an air filter and gate valves for the air supply and feedback pressure lines. The flow regulator established and maintained the desired flow rate to the test section. The vent and purge valves were used in conjunction with the flow regulator to maintain steady flow conditions. These valves vented mass flow in excess of that required for test conditions so as to keep the compressors continuously running and minimize pressure fluctuations upstream of the flow regulator. The vent valve was used for gross adjustments to the amount of flow vented. The purge valve was used to fine-tune the amount of flow vented as well as to drain water, rust and compressor lubricant from the inlet plumbing lines. The air filter trapped water, compressor lubricant and rust upstream of the flow regulator. The cleanliness of the filter had a significant impact on test conditions, as discussed in Appendix B, <u>Impacts of the Air Filter</u>. These components are schematically represented in Figure 3.

3.2.1.1 <u>Inlet Plumbing</u>. The inlet plumbing connected the compressors, flow control hardware and stilling chamber. The major change to the inlet plumbing configuration made from that of Rothenflue (1996) was the de-coupling of the air feed

line to the BLRF from the cascade test facility. Whereas Rothenflue (1996) directed the flow from the cascade facility to the BLRF, for this project the delivery pipes fed both facilities in parallel. As a result of this change, maximum mass flow rate was decreased to 0.45 kg/s (1 lbm/s), a new seeding particle injection method was required and flow control was augmented due to passage of the entire flow through the flow regulator. In addition, the change in inlet plumbing configuration required a new diffuser cone to connect the inlet plumbing line to the inlet aperture of the stilling chamber. The diffuser is shown in Figure 3. The cone was designed with an included divergence angle of 8° to prevent inlet flow separation.

3.2.2 <u>Stilling Chamber</u>. The chamber provided uniform, seeded, straightened flow to the test section. The stilling chamber is shown in Figure 3. Internal details and design requirements for the chamber are given by Rothenflue (1996). Initial configuration of the test hardware required the leveling of the stilling chamber in conjunction with the test section, as discussed in Appendix C, <u>Stilling Chamber and Test Section Leveling</u>.

The major modification to the stilling chamber was the addition of a top-mounted seeder plenum. The seeder plenum can be seen in Figure 3. A removable access panel on the top of the plenum provided access to the particle generator and injection tubes. The two injection tubes, fabricated from PVC pipe, extended downward from the plenum into the low-speed, turbulent region downstream of the stilling chamber's inlet diffuser plug. To facilitate seeding particle injection into the stilling chamber, the seeder plenum was pressurized with a feed line from the shop air system. The supplied pressure forced the seeding particles through the injector tubes and into the stilling chamber through a

series of holes drilled in the tubes. These injection holes were located near the spanwise center of the test section and were oriented to face upstream to reduce possible turbulence generation.

Seeding particles were generated with a TSI Model 9306 6-jet atomizer. A shop air supply line routed into the seeder plenum provided the pressure required to operate the atomizer. As recommended by Luker (1995), olive oil was used as the seeding particle material. A full atomizer reservoir of olive oil could support approximately eight hours of testing. Maximum seeding particle flux, as judged by visual observation, was obtained through the adjustment of the atomizer flow regulator, bypass air valve and jet on/off switches. A discussion of the factors involved in the selection of the atomizer as the seeding particle generator for this experiment is contained in Appendix D, Seeding Particle Generator.

3.2.3 Test Section. A new test section was built for this experiment. Compared with the test section of Rothenflue (1996), the new test section had flexible sidewalls and larger, rigid top and bottom plates to accommodate the diffusion needed to create adverse pressure gradients. Figure 3 shows a top view of the new test section. This test section was designed with the same basic dimensions as that used by Rothenflue (1996): 1 m in length with a 16 cm wide by 40 cm tall inlet. The new test section also used the same stilling chamber attachment points. As part of the initial configuration of the test hardware, the test section was leveled and attached to the stilling chamber. This process is discussed in Appendix C, Stilling Chamber and Test Section Leveling.

Figure 3 shows the test section coordinate system. An orthogonal, right-hand rule system identical to that of Rothenflue (1996) was used. The positive x axis was in the

21

streamwise flow direction. The leading edge of the test plate was defined as x = 0. The positive y-axis was normal to the test plate through the right side of the test section, i.e., the right side as viewed downstream from the stilling chamber. The surface of the test plate was defined as y = 0 for the smooth plate. For the riblet plate, the top of a riblet peak was defined as y = 0. The positive z-axis was in the spanwise direction toward the floor of the laboratory. The z = 0 point was arbitrarily chosen near the middle of the test plate.

3.2.3.1 <u>Test Plates</u>. Rothenflue's (1996) smooth and riblet test plates were used for this project. The riblet test plate is shown in Figure 4. The riblets were V-shaped with a riblet height of 2.6 mm and a riblet spacing of 3.0 mm. The riblets spanned the middle 25.4 cm of the plate and extended the entire 1 m length of the plate. The leading edge of the plate was a 30° wedge. The smooth plate was identical to the riblet plate with the exception of the riblets. Both plates were fabricated from 1.27 cm (0.5 in) thick plexiglass sheet.

3.2.3.2 <u>Sidewalls</u>. Streamwise pressure gradients were created through the manipulation of sidewall curvature. Flexibility was the primary sidewall design requirement. Based on flexibility, transparency and availability, 0.3175 cm (0.125 in) thick plexiglass sheet was used to make the sidewalls. The sidewalls were held in place with hinge clamps and plexiglass L-shaped brackets. Pins at the top and bottom of each sidewall leading edge fixed leading edge location and allowed sidewall rotation toward and away from the test plate. Figure 3 shows the sidewalls and L-shaped brackets.

The right sidewall featured a 5.1 cm wide slot located in the spanwise center of the sidewall. This slot extended streamwise from near the leading edge of the

sidewall to approximately the streamwise mid-point of the sidewall. The purpose of this slot was to provide an unobstructed line of sight between the measurement probes and the test plate. The geometry of the slot and optics hardware limited data acquisition to between the 95 and 570 mm streamwise stations on the test plate. Preliminary tests were conducted with this slot unmasked in order to characterize slot-generated turbulence. In order to reduce turbulence, as recommended by Rothenflue (1996), the remainder of the tests were conducted with the laser slot masked except for two small laser passage windows.

3.2.3.3 <u>Top and Bottom Plates</u>. The top and bottom plates held the test plate in position, provided attachment points for the sidewall hinge clamps and constrained the spanwise movement of the flow. These plates, 50 cm wide and 1 m in length, were constructed from 1.9 cm (0.75 in) thick Plexiglass sheets. Four threaded steel rods located at the corners of the plates fastened the two plates together, supported the weight of the top plate and kept the two plates a constant distance apart. A 1.27 cm (0.5 in) wide slot cut into the internal face of the plates held the test plate in position. The plates can be seen in Figure 3.

3.3 <u>Laser Doppler Anemometry System</u>

The DANTEC 3-D LDA system acquired, processed and reduced boundary layer velocity measurements. The three main subsystems of this LDA system were the FiberFlow® system, the data processing system and the 3-D traverse system. Basic laser Doppler anemometry principles and the operating instructions and characteristics of this DANTEC LDA system are thoroughly discussed in the DANTEC FiberFlow® User's Guide, the BSA User's Guide and the Burstware 2.0® User's Manual. Specific

application of this system for low-speed velocity measurements over a riblet plate is discussed in Rothenflue (1996). Additional perspective on the operation and characteristics of this system can be found in Luker (1995).

3.3.1 FiberFlow® System. The FiberFlow® system consisted of five major components: the laser, transmitter, beam manipulators, measurement probes and photo-multiplier (PM) tubes. The FiberFlow® system generated three pairs of laser beams, maximized beam intensity, transmitted the beams, focused the beams to form a measurement volume, collected reflected laser light and transformed the reflected light into electrical signals for data processing. A thorough description of the components and their functions can be found in the FiberFlow® User's Guide.

3.3.1.1 Laser. The FiberFlow® system laser was an Ion Laser Technology, Inc. argon-ion 300 mW air-cooled unit. It was mounted on a bench with the transmitter, as represented schematically in Figure 3. The laser produced three principal wavelengths: 476.5 nm (purple), 488 nm (blue) and 514.5 nm (green). The three wavelengths exited the laser head in one coincident beam and passed through a beam shield and into the transmitter. The cylindrical, telescoping beam shield, which can be seen in Figure 3, prevented beam scatter, beam degradation and internal transmitter damage from airborne particles and eliminated the safety hazard of an exposed beam.

As part of initial hardware configuration, the laser was aligned with the mounting bench centerline and the laser's power output was measured and maximized. Alignment of the laser is discussed in Appendix E, Laser and Transmitter Alignment. The procedures used to measure and maximize laser output power are discussed in Appendix F, Reduced Laser Power Levels. The actual maximum output power of the

24

laser was found to be approximately 70% of its nominal 300 mW level. The negative effects of this reduced power level on data acquisition were partially mitigated by the use of the TSI 6-jet atomizer as a particle generator and the redistribution of available power between the three wavelengths. Appendix F, Reduced Laser Power Levels, contains a discussion on the investigation of and corrective actions for the reduced power levels.

3.3.1.2 Transmitter. The FiberFlow® transmitter performed three functions. First, it split the input laser beam into two beams and shifted one of the beams in frequency by 40 MHz with an internal Bragg cell. The frequency shift was required to resolve reverse velocities. The Bragg cell was also used to balance the power levels between the shifted and unshifted beams. Second, the transmitter separated the two output beams from the Bragg cell into the 514.5 nm, 488.0 nm and 476.5 nm wavelengths. Last, the transmitter directed the six resulting beams to the beam manipulators. Beam splitting and direction to the manipulators was accomplished with internal prisms.

As part of the initial hardware configuration process, the transmitter was aligned with the input beam from the laser. This was done to produce a well-specified beam path between the its input aperture and the beam manipulators. According to the FiberFlow® User's Guide, a well-specified beam path was required to maximize beam intensity. Proper alignment of the transmitter was achieved through the systematic adjustment of the transmitter's three legs until maximum beam intensity was achieved. The details of the process are described in Appendix E, Laser and Transmitter Alignment, and the FiberFlow® User's Guide.

3.3.1.3 <u>Beam Manipulators</u>. Six beam manipulators were mounted on the transmitter. The beam manipulators tuned, or adjusted, the angle and position of the six transmitter output beams to match the axis of the optical transmission fibers attached between the probes and the manipulators. The optical fibers and probes are schematically represented in Figure 3. As discussed in the FiberFlow® User's Guide, a precise beam position with respect to the optical axis of the transmission fiber was required to obtain maximum beam intensity and prevent damage to the transmission fibers.

Beam tuning was accomplished with the four high-resolution adjustment knobs on each manipulator body. The process was complete once a maximum intensity had been achieved for each of the six beams. Beam tuning was done daily and after transmitter alignment. The details of the process are presented in Appendix G, <u>Beam Focusing, Tuning and Balancing</u>.

3.3.1.4 <u>Fiber Plugs</u>. Six fiber plugs attached to the manipulators focused and balanced the six manipulator output beams into their respective fiber optics transmission lines. These lines connected with a distribution unit that routed the beams into two cable bundles attached to the measurement probes. The distribution unit is schematically represented in Figure 3. Focusing of the beams into the transmission lines was required to maximize beam intensity. Balancing, or equalization, was required for beams of the same wavelength in order to maximize contrast between the probe volume fringes and dark bands (Weissman, 1996). Balancing was the process of de-focusing the maximum strength beam of each wavelength pair to match the power level of the weaker beam. Focusing and balancing were done in conjunction with beam tuning and were

26

accomplished with the focusing ring located on each of the fiber plugs. The two processes are discussed in Appendix G, Beam Focusing, Tuning and Balancing.

3.3.1.5 Measurement Probes. Two DANTEC measurement probes focused the six beams to form a measurement volume (or probe volume) and gathered reflections from the measurement volume for velocity data processing. The probes were mounted on the traverse bench and are schematically shown in Figure 3.

The measurement probes were configured to operate in the off-axis, back-scatter mode. In this mode, each probe gathered reflections from the wavelength(s) transmitted by the other probe. For this experiment, the 1-D probe transmitted the 476.5 nm (purple) beams and received reflections from the 488 nm (blue) and 514.5 (green) nm beams. The 2-D probe transmitted the 488 nm and 514.5 nm beams and received reflections from the 476.5 nm beams. This configuration produced a significantly smaller probe volume than the on-axis mode. The smaller probe volume reduced particle location ambiguity, provided the higher spatial resolution required to describe boundary layer flows and allowed data acquisition closer to the test surface. Particle location ambiguity, as discussed in the DANTEC BSA User's Guide, refers to the uncertainty of the location of a given particle in relation to the probe volume.

The hardware and geometry of the measurement probes were configured as done by Rothenflue (1996). Specifically, each measurement probe was fitted with a beam expander and a 600 mm focal length front lens to produce the smallest possible measurement volume. The angle included between the transmission axes of the probes was set at 70°. This reduced the size of the measurement volume compared to the 35° included angle typically used for 3-D velocity experiments (Weissman, 1996). With this

27

hardware and geometry configuration, the probes produced an ellipsoidal measurement volume approximately 150 μm in diameter and 250 μm in length (Rothenflue, 1996).

The measurement volume was formed by the movement of the focal points of the six beams in relation to each other until all six precisely coincided. For rough positioning, the locations of the focal points were adjusted with the movement of the probes upon the traverse bench and the rotation of each probe on its mounting base. For precise positioning, focal point locations were adjusted with the three micrometer knobs located on the 1-D probe base. These knobs were used to precisely adjust the rotation, tilt and translation of the 476.5 nm (purple) beam pair. The details of probe volume formation are presented in Appendix H, Probe Volume Formation.

The probes captured Doppler bursts reflected from particles in the measurement volume. These bursts were focused on the probes' internal receiver optics by the front lenses and beam expanders. The bursts were carried from the receiver optics to the distribution unit through cable bundles and then routed to the appropriate photo-multiplier tube for processing.

3.3.1.6 Photo-Multiplier Tubes. Three DANTEC model 57X08 photo-multiplier (PM) tubes converted the reflected light from the laser probes into voltage signals. The PM tubes are shown in Figure 3. Each PM tube was used for one wavelength. In the off-axis, back-scatter mode used in this experiment, reflections gathered by the 2-D probe were directed to the 476.5 nm PM tube and the reflections gathered by the 1-D probe were directed to the 514.5 nm and 488 nm PM tubes. According to the BSA User's Guide, each PM tube had a current limitation of 1.6 mA. The maximum input voltage for each PM tube was 2040 V (Weissman, 1996). Voltage

signals from the PM tubes were transmitted to the Burst Spectrum Analyzers (BSAs) for velocity data processing.

3.3.2 <u>3-D Traverse System</u>. The 3-D traverse system provided precise location of the probe volume in the streamwise, normal and spanwise (x, y and z) directions. The system consisted of a bench moveable in three mutually perpendicular axes, a stepper motor for each axis and a control unit. The bench, as well as the traverse coordinate system, is shown in Figure 3. The three stepper motors were controlled with the Burstware® program. As determined by Rothenflue (1996), the stepper motors provided precision movement in each axis in steps of as small as 0.05 mm. This precision allowed acquisition of velocity profiles inside the riblet valleys. As part of the initial configuration of the test hardware, the traverse was positioned and aligned with the test section as discussed in Appendix I, <u>Traverse Positioning and Alignment</u>.

3.3.3 <u>Data Processing System</u>. The data processing system consisted of three BSAs connected to a personal computer equipped with the Burstware® data acquisition control program. Each BSA received electrical signals from one PM tube and transformed the signals into velocity components in the axes of the probe coordinate system. The probe coordinate system is shown in Figure 5. Burstware® set the BSA processing parameters, positioned the probe volume, performed coincidence filtering and accomplished coordinate transformation on velocity components. A thorough description of the program can be found in the Burstware 2.0® User's Manual.

To control data acquisition, the Burstware® program used a variety of programmable processing parameters. These parameters were divided into optical, front panel, soft key and program sets. A thorough description of all parameters can be found

29

in the DANTEC BSA User's Guide and the Burstware 2.0® User's Manual. The

significant parameters for this experiment are quantified and discussed in Appendix J,

Data Acquisition Parameters.

3.4 Test Procedures

The daily test procedure consisted of the maximization of data acquisition rates,

the location of the probe volume with respect to the test plate surface, acquisition

programming, the establishment of test conditions, data acquisition and data reduction.

3.4.1 Maximization of Data Acquisition Rates. Data acquisition rates were

maximized daily through beam focusing, tuning and balancing and the fine tuning of the

probe volume. These processes are discussed in Appendix G, Beam Focusing, Tuning

and Balancing and Appendix H, Probe Volume Formation. Maximization of rates was

critical to the timely, efficient acquisition of data.

3.4.2 Measurement Volume Location. The location of the measurement volume

with respect to the test plate surface was critical for an accurate description of the flow

field. The measurement volume was located prior to the establishment of test conditions.

The process was accomplished daily to compensate for thermal expansion of test

hardware and FiberFlow® components. The process was also accomplished for each new

streamwise acquisition location and each time the test plate was removed and re-installed.

The proximity of the probe volume with the test plate during this process required

that PM tube high voltage values be reduced to ≤ 900 V to prevent PM tube damage from

strong surface reflections. Also, the saturation level of the PM tubes was diligently

monitored throughout the process. To protect against damage, PM tube high voltage

values were reduced if saturation levels of greater than 50% were observed.

The first step in the location of the measurement volume was to mark the point of interest on the test surface. For the smooth test plate, a thin line was drawn with a felt-tipped pen directly on the plate at the desired streamwise coordinate. No particular spanwise coordinate had to be specified for the smooth plate. For the riblet plate, a line was drawn along a riblet peak near the center of the laser slot. The desired streamwise station was then marked on the peak with a small dot.

The probe volume was maneuvered in the streamwise and spanwise directions with the traverse system until the probe volume coincided with the point of interest marked on the test plate. This coincidence was verified visually through the transparent top plate from above the test section and from the right side of the test section with a small telescope. Laser goggles were required for visual verification to filter harmful reflections from the test plate surface and to pinpoint the strongest, central portion of the probe volume. Seeding particles were injected into the test section to make the beams visible and facilitate the process.

The final step in the process was to move the probe volume in the normal direction until its brightest, central point was incident on the test plate surface. The end result of this step was the location of the $y = 0$ point. The process began with the movement of the probe volume to a point inside the test plate $(y < 0)$. This was done to eliminate potential position errors associated with traverse system gear slop. The gear slop appeared as position error each time the traverse direction along a given axis was reversed. The magnitude of the slop was quantified by Rothenflue (1996) to be on the order of 0.05 mm. The probe volume was typically moved into the test surface a distance of at least 0.5 mm.

The probe volume was moved in the positive y direction, typically in increments of 0.05 mm, until the test plate surface (y = 0) was located. The test plate surface was indicated by maximum reflection intensity, as measured by an oscilloscope connected to the Doppler output of the 488.0 nm (blue) BSA. The low power of this wavelength minimized the possibility of PM tube damage. In addition, this wavelength tended to most accurately locate the test surface due to the beam pair's vertical orientation.

In most instances, more than one y location could be interpreted as the coincidence of the central portion of the probe volume with the test surface. In these situations, the largest y coordinate was chosen as the test plate surface location. With the test surface located, the origin of the traverse system was reset with the Burstware® program to aid in traverse programming.

3.4.3 <u>Acquisition Programming</u>. After the probe volume was located, the system was programmed with the coordinates of the desired data acquisition locations, the acquisition parameters for each point and the data acquisition mode.

For profiles in the streamwise direction, data was typically acquired every 50 mm between x = 200 mm and x = 500 mm. Streamwise profiles were acquired to help establish and verify a given streamwise pressure distribution in the test section. The y coordinate for each point in these profiles was 30 mm. This y coordinate was used to ensure that the data acquisition locations were outside the test surface and sidewall boundary layers. Due to the need to move the masked slot's laser windows for each new streamwise location, the system was programmed to acquire the desired number of bursts and wait for user input prior to proceeding to the next acquisition location.

32

For spanwise profiles, velocity data was typically acquired every 0.25 mm across a 6 mm span, equal to twice the riblet spacing, s. The height above the test surface at which the spanwise profiles were acquired was varied between 0.5 mm to 0.8 mm. This range was chosen so that noticeable v and w values could be measured as based on the anticipated size of the riblet-valley vortices. The vortices were expected to be roughly circular in shape with a diameter no greater than one-half the riblet spacing, s. For spanwise profiles, the system was programmed in the fully automatic acquisition mode. In this mode, the system automatically proceeded to the next acquisition location after the desired number of bursts had been collected.

For normal profiles, the probe volume was moved incrementally outward from the test plate surface until a point was reached where harmful surface reflections were no longer acquired. This point was subsequently defined as the first data acquisition location in the profile. This search was accomplished with the on-line data acquisition feature of the Burstware® program where data was processed and displayed on-screen but not digitally recorded. Harmful surface reflections appeared in the BSA histograms as abnormally large spikes, multiple spikes or irregular, non-continuous distributions. The location of the first point in the profile varied daily as well as with spanwise and streamwise location due to test plate machining imperfections (highly reflective flat spots at peaks and valleys), variations in beam intensity and probe volume alignment and thermal effects.

Within the expected thickness of the boundary layer, data acquisition locations for normal profiles were evenly spaced. Outside the boundary layer, the increment between data points was increased since detailed flow field descriptions were less important in this

area. Up to approximately 1.0 mm above the test plate surface, acquisition parameters (such as PM high voltage, gain and time-out) were individually programmed for each location due to the variability of particle flux and the impacts on data quality from surface reflections. To conveniently reset acquisition parameters, data acquisition at each point was manually controlled. Above $y = 1.0$ mm, particle flux was relatively constant and the amount of light reflected from the test plate was negligible. Consequently, the system was programmed to acquire data in the automatic mode for this region.

3.4.4 <u>Establishment of Test Conditions</u>. Establishment of test conditions included the establishment of steady flow at the desired freestream velocity and the establishment of the desired streamwise pressure gradient. This process was time-consuming and highly iterative since changes in flow velocity and streamwise pressure gradient mutually affected each other.

3.4.4.1 <u>Steady Flow Freestream Velocity</u>. Steady flow was established with the flow regulator and vent and purge valves. For all test cases, the freestream test section inlet velocity was set at approximately 5 m/s. The LDA system was used to verify the desired freestream velocity.

3.4.4.2 <u>Streamwise Pressure Gradient</u>. Variation of sidewall curvature was used to establish streamwise pressure gradients within the test section. Sidewall curvature was adjusted with the spring clamps and L-shaped brackets in a trial and error process until the desired streamwise pressure gradient was obtained. Through streamwise velocity measurements, the LDA system was used to verify the presence of the desired streamwise pressure gradient. Once obtained, no sidewall curvature adjustments were made for subsequent tests with the same pressure gradient. Instead, the pressure gradient

was recreated simply by the duplication of the test section inlet velocity used to first obtain it.

As part of this process, additional adjustment of the back-side (or left side) sidewall curvature was accomplished to eliminate flow separation at the test plate leading edge. Flow separation, also encountered by Rothenflue (1996), was due to the abrupt change in flow direction on the back-side of the test plate caused by the wedge-shaped leading edge, as shown in Figure 4. The back-side sidewall curvature was adjusted to change the effective angle of attack of the test plate and keep the flow attached to the test side leading edge (Rothenflue, 1996).

Attached flow was qualitatively verified through flow visualization with cotton ball tufts. A group of tufts extended in the upstream direction was attached near the test plate leading edge on the test side at different spanwise and streamwise stations. The tufts exhibited distinctly different behavior for attached and separated flows. For attached flow, the tufts remained stationary and exhibited small displacement oscillatory motion. Separated flow caused the tufts to move randomly with large displacements.

3.4.5 Data Acquisition. After steady test flow conditions were established and acquisition parameters were appropriately set for the given profile, velocity data at each programmed location was acquired. The laboratory air temperature and pressure were recorded at the beginning of each profile. Key parameters were monitored during testing to ensure the acquisition of quality data.

To ensure that steady flow conditions were maintained, pressure upstream of the flow regulator and flow regulator feedback pressure were monitored for the duration of each profile. A test re-start was required for any profile with upstream pressure

fluctuations of $\geq \pm 6.9$ kPa (± 1.0 psi) or with any feedback pressure fluctuations. In addition, the local freestream velocity, U, was recorded before and after each profile. As with Rothenflue (1996), any profile for which the pre-test and post-test U values varied by more than 0.05 m/s was repeated.

In addition to upstream pressure, feedback pressure and U, the real-time histograms and data acquisition rates for each BSA were monitored during data acquisition. Inspection of real-time histograms was accomplished for all points in the range $y \leq 1.0$ mm to ensure that detrimental surface reflections were not accidentally recorded. Above $y = 1$ mm, surface reflections were rarely observed. Histograms were also inspected for excessive noise and inappropriate shapes. Valid histograms showed measured velocities clustered closely about one central value with little accompanying noise across the programmed bandwidth. Acquisition rates were observed to evaluate the quality of probe volume alignment, the quantity of seeding particles as a function of time and to determine the appropriate time-out value for the desired number of bursts.

3.4.6 <u>Data Reduction</u>. Data reduction consisted of the averaging and weighting of velocity measurements, the calculation of turbulence intensities and the transformation of velocity measurements to the test section coordinate system. These tasks were accomplished with the Burstware® program. Calculation of turbulence intensities is discussed in Section 4.2.3, <u>Laser Slot Turbulence</u>.

3.4.6.1 <u>Weighting and Averaging</u>. As discussed in the Burstware 2.0® User's Manual, the velocity component measurements from all bursts acquired at each location were averaged to produce one representative mean velocity value for each BSA component direction. As done by Rothenflue (1996), residence time-weighting was

incorporated into the calculation of each mean velocity component. As discussed in the

Burstware 2.0® User's Manual, residence time-weighting was a process through which

the contribution of each burst to the calculated mean velocity component was weighted

by the burst's transit time. The residence time-weighted mean velocity components were

calculated by the Burstware® program with

$$\overline{u}_{weighted} = \frac{\sum (u_i \Delta t_i)}{\sum \Delta t_i} \tag{8}$$

In this equation, u_i is the ith recorded velocity component and Δt_i is its corresponding

transit time.

The net effect of residence time-weighting was to reduce the contribution

of high speed particles to the calculated mean velocity components. Without residence

time-weighting, the calculated mean velocity values would have been erroneously high

due to the larger number of high speed particles that passed through the probe volume.

The speed of these particles, as opposed to their density within the flow, was the reason a

larger number of them were anticipated to pass through the probe volume.

3.4.6.2 Coordinate System Transformation. As discussed in the

DANTEC BSA User's Guide, the LDA system acquired velocity data in the non-

orthogonal probe coordinate system shown in Figure 5. To produce meaningful results,

the velocity data was converted from this system to the orthogonal test section coordinate

system shown in Figure 3. The conversion of velocity data was accomplished by the

Burstware® program with a user-defined transformation matrix. Development of this

transformation matrix is presented in Appendix K, Coordinate System Transformation.

Numerical values used in this matrix were derived from the angles included between the

37

two laser probes and the measured rotation angles between the traverse and test section

coordinate systems.

IV. Discussion of Results

4.1 Overview

Three test cases were conducted. The first test case, a zero pressure gradient applied to a smooth test plate, was used to validate the test procedure, verify the accuracy of the LDA system, verify the capabilities of the new BLRF test section and provide turbulence generation characteristics of the laser slot. The second test case, a favorable pressure gradient applied to a riblet test plate, used the same sidewall curvature as the smooth plate case. This case provided additional data on the turbulence generation characteristics of the laser slot. The third test case was a moderate adverse pressure gradient applied to the riblet test plate. The second and third test cases were used to examine turbulence boundary layer characteristics and the formation of riblet-valley vortices. All three test cases were conducted with a test section inlet velocity of approximately 5 m/s. The data for each case is presented in the Figures section.

The three test case flows were studied through the acquisition and analysis of velocity profiles. Streamwise velocity variations, acquired in the freestream 30 mm above the test plate surface, were used to verify the pressure gradient for each case. Normal velocity profiles were acquired to examine boundary layer characteristics. For the riblet test plate, normal velocity profiles were also used to examine the formation of vortices. These profiles were acquired above riblet peaks, riblet valleys and the mid-points of the riblet slopes. Spanwise velocity variations were also acquired to study the formation of vortices for the riblet plate cases. Normal and spanwise velocity profiles

were acquired at streamwise stations 200 mm and 400 mm downstream from the leading edges of the test plates.

4.2 Smooth Plate, Zero Pressure Gradient Case

Data for this case was acquired with open and masked laser slots in order to examine the slot's turbulence generation characteristics.

4.2.1 Freestream Velocity Profile. Figure 6 shows the variation of U, the local freestream velocity, with x for an open laser slot. A zero pressure gradient was produced with the open slot by the adjustment of sidewall curvature until a constant U was obtained through the test section. Figure 6 also shows data acquired with a masked test slot and the same sidewall curvature. The masked slot data shows an increase in velocity through the test section. A streamwise flow acceleration, as described by White (1991), indicates the presence of a favorable pressure gradient. The magnitude of the pressure gradient was estimated with a modified form of Euler's equation:

$$-\frac{\partial p}{\partial x} = \rho a_x \qquad (9)$$

where p is pressure, ρ is fluid density and a_x is the acceleration in the x direction. The acceleration term was estimated with

$$a_x = U\frac{\partial U}{\partial x} \qquad (10)$$

In Equation (10), the term $\partial U/\partial x$ was approximated with $\Delta U/\Delta x$. The pressure gradient magnitude calculated with Equation (9) and (10) was approximately -2.727 Pa/m ($-1.2\cdot10^{-4}$ psi/ft). This pressure gradient resulted from the reduction of effective exit area of the test section by the masking of the slot.

4.2.2 <u>Blasius Solution Re-creation</u>. Re-creation of the Blasius solution, as presented by White (1991), was used to verify test procedures, verify the capability of the new test section to produce known flow conditions and assess the accuracy of the LDA system. Data acquired with open and masked laser slots are super-imposed on the Blasius solution in Figures 7 and 8, respectively. These figures display the variation of the dimensionless velocity, u/U, with the similarity variable, η. The dimensionless velocity was calculated from measured values of the local velocity, u, at each acquisition point and the local freestream velocity, U. The similarity variable, η, as presented by White (1991), was calculated with

$$\eta = y\left(\frac{U}{2vx}\right)^{\frac{1}{2}} \tag{11}$$

The kinematic viscosity, v, as presented by Roberson and Crowe (1985), is defined as

$$v = \frac{\mu}{\rho} \tag{12}$$

The fluid density, ρ, was found with the Ideal Gas Law:

$$\rho = \frac{P}{RT} \tag{13}$$

In Equation (13), P and T are the measured laboratory pressure and temperature, respectively, and R is the ideal gas constant for air. In Equation (12), the dynamic viscosity, μ, was interpolated from a table of temperature and viscosity values in White (1988).

As seen in Figure 7, the Blasius solution was successfully re-created with an open laser slot at three different freestream velocities at the 200 mm station. The small amount of scatter evident in the data is attributed to the difficulty in maintaining steady flow

41

conditions in the test section. Figure 8 shows data acquired with a masked slot at the 200 mm and 400 mm stations. The data in Figure 8 also agrees closely with the Blasius solution. Slight deviations from the Blasius solution between u/U = 0.6 and u/U = 0.9 are observed in this figure. These deviations are consistent with the presence of a favorable pressure gradient in the test section, as discussed in Section 4.2.1, Freestream Velocity Profile. The deviations from the Blasius solution in Figure 8 are most noticeable in the 200 mm station data. In the 400 mm station data, the deviations are almost negligible.

4.2.3 Laser Slot Turbulence. The velocity data collected for the re-creation of the Blasius solution was used to examine the effects of the laser slot on turbulence in the freestream and boundary layer. Figures 9 and 10 show the variation of turbulence intensity, Tu, with y at the 200 mm and 400 mm stations, respectively. As presented by White (1991), the turbulence intensity was calculated with the 3-D mean-squared velocity fluctuation values with

$$Tu = \left(\frac{1}{U}\right)\sqrt{\frac{\overline{u'^2} + \overline{v'^2} + \overline{w'^2}}{3}} \qquad (14)$$

where the primed quantities are the velocity fluctuations.

The calculated Tu levels were used to assess the flow state of the boundary layer. As applied by Rothenflue (1996), a boundary layer peak Tu below 3% was indicative of an essentially laminar boundary layer. A peak turbulence intensity between 3% and 9% indicated a transitional boundary layer and a peak intensity $\geq$ 9% indicated a fully turbulent boundary layer.

A comparison of Figures 9 and 10 shows the influence of the laser slot on turbulence intensity in the boundary layer. In Figure 9 the peak open slot Tu is slightly

42

over 4%, approximately 0.8% greater than the masked slot peak Tu. Thus, the open slot influenced the boundary layer flow state at only 200 mm downstream from the test plate leading edge. Both curves also show a similar shape. In Figure 10, the open slot Tu levels are significantly larger than the masked slot levels. In addition, the differences in shape between the curves in Figure 10 indicate that transitional behavior is present over a greater area in the boundary layer for the open slot case. Clearly, the mixing region caused by the open slot generates turbulence within the boundary layer and promotes transition.

The flow states of the boundary layers in Figures 9 and 10 are similar to those observed by Rothenflue (1996) for a zero pressure gradient flow at U = 7.5 m/s and an open laser slot. According to the boundary layer flow state criteria previously stated, the turbulence intensity levels in Figure 9 indicate essentially laminar boundary layers at the 200 mm station. The open slot data may indicate some transitional behavior. Rothenflue (1996) found a laminar boundary layer at the 200 mm station. The masked slot turbulence intensities of Figure 10 indicate an essentially laminar boundary layer at the 400 mm station with some possible transitional behavior. None of the possible transitional behavior in Figures 9 or 10, however, appeared to affect the duplication of the Blasius solution. For the open slot case, the boundary layer is clearly transitional. For an open slot, Rothenflue (1996) also observed a transitional boundary layer at the 400 mm station.

In both Figures 9 and 10, turbulence intensity continues to increase as y approaches zero (test plate surface). From Rothenflue (1996), the characteristic turbulence intensity profile shape displays an increase from the Tu freestream level to a

43

peak value in the boundary layer followed by a reduction toward zero near the test plate surface. The expected reduction to zero does not appear in Figures 9 and 10. Data acquisition near the test plate surface was difficult due to low laser power levels, as discussed in Appendix F, Reduced Laser Power Levels, combined with low particle flux near the surface. Had data acquisition been possible closer to the test plate, it is believed that the characteristic reduction in turbulence intensity would have been observed.

A comparison of Figures 9 and 10 also shows the impact of the laser slot on freestream turbulence. In Figure 9, the median freestream turbulence intensities for the masked and open cases are approximately 2.3% and 2.5%, respectively. In Figure 10, the median freestream turbulence intensity for the masked slot case remained near 2.3%. The median freestream turbulence intensity for the open slot case, however, increased to approximately 3.2%. This qualitatively agrees with the smooth plate, open slot results of Rothenflue (1996). At $U = 7.5$ m/s, Rothenflue (1996) found turbulence intensity increased between the 200 mm and 400 mm stations from approximately 2.2% to approximately 4.8%. Clearly, an open laser slot generates freestream turbulence.

4.2.4 Normal Velocity Profiles. Figures 11-13 show the variation of u, v and w with y at the 200 mm and 400 mm streamwise stations. The data in these figures was acquired with a masked laser slot.

Figure 11 shows the variation of u with y (a re-plot of Figure 8 in natural coordinates). The growth of the boundary layer with x is evident by the increase in velocity defect for a given y coordinate. This growth is indicative of the expected propagation of viscous effects outward from the test plate surface as the flow travels through the test section. The boundary layer thickness, $\delta_{99\%}$, is defined as the point above

44

the surface where u reaches 99% of U. From the figure, $\delta_{99\%}$ is approximately 3.94 mm and 5.43 mm at the 200 mm and 400 mm stations, respectively. Last, the similarity in shape of the two profiles was expected since the flow was very nearly self-preserving flow as evidenced by the proximity of the recast data to the Blasius solution in Figure 8.

Figure 12 shows the variation of v with y. The 200 mm station data shows a growth of v from close to zero near the test surface to a maximum upwash (or +v) of approximately 0.7% near 6 mm above the test plate. Above 6 mm, the v component drops to and holds steady at about 0.5%. The 400 mm station data shows a similar upwash from the surface of the plate. However, the magnitude of the upwash is roughly half of that at the 200 mm station. This upwash is believed to have had two primary sources. First, as stated by White (1991), non-zero v values are expected in smooth plate flow due to the deflection of flow away from the plate surface to satisfy conservation of mass. This implies that, as the flow travels downstream, the growth of the boundary layer requires a larger upwash to satisfy mass conservation. Outflux through the masked slot's two small laser passage windows caused by the favorable pressure gradient may have also been a source of upwash. This outflux may also account for the reduced upwash observed at the 400 mm station. The drop in static pressure between the 200 mm and 400 mm stations caused by the favorable pressure gradient would have resulted in a reduced outflux at the 400 mm station and an accompanying reduction in upwash.

Figure 13 shows the variation of w with y at the 200 mm and 400 mm stations. Several observations can be made from the figure: the w component grew from zero near the test plate surface to a maximum and then decayed to zero in the freestream, the 400 mm w values were approximately 50% of those at the 200 mm station and the velocity

45

magnitudes were comparable to those in Figure 12. Since this flow was expected to be 2-D in nature, the presence of a spanwise drift was unexpected. The primary factors believed to have caused this spanwise drift were the flow deflection away from the plate to satisfy conservation of mass and outflux through the masked slot's two small laser passage windows. It is of interest to note, however, that the spanwise drift in the figure is in the positive z direction, towards the bottom of the test section. This could be the result of a slight spanwise pressure gradient in the tunnel caused by the seeding particle injection apparatus. Branam (1997) later verified the susceptibility of the test section to spanwise pressure gradients.

Measurement uncertainty in the angles used for velocity component transformation is not believed to have contributed to the upwash and spanwise drift observed in Figures 12 and 13, respectively. Specifically, the shape of the curves in Figure 13 is not indicative of any gross angle measurement errors. Measurement errors would have appeared as a complete positive or negative shift in the location of all data points. As evidenced by the zero velocities acquired near the plate surface, especially those of Figure 13, no shifts in the profiles were present.

4.3 Riblet Plate, Favorable Pressure Gradient Case

For this case, sidewall curvature was left unchanged from that used for the smooth plate case. No changes in curvature were implemented since the two test plates were switched several times during a series of preliminary tests. Except as noted, the data for this case was acquired with a masked laser slot to reduce turbulence levels.

4.3.1 Freestream Velocity Profile. Figure 14 shows the variation of U with x for the riblet test plate and a masked laser slot. The masked laser slot combined with the

46

sidewall curvature used in the smooth plate case resulted in a favorable streamwise pressure gradient. The magnitude of the pressure gradient was estimated to be approximately -2.826 Pa/m ($-1.2 \cdot 10^{-4}$ psi/ft) with Equations (9) and (10). The magnitude of the pressure gradient is comparable to the masked slot data in Figure 6 and indicates that the riblets did not have a significant impact on external flow conditions.

 4.3.2 <u>Turbulence Profiles</u>. Figure 15 shows the variation of Tu with y at the 200 mm station for a masked laser slot. At this station, data was acquired directly above a riblet peak. The freestream turbulence intensity of approximately 2% is comparable to the smooth plate data in Figure 9. Besides this similarity, the Tu levels of Figure 15 are significantly higher than those of the smooth plate case. In fact, the boundary layer peak Tu of approximately 9.6% indicates the presence of a fully turbulent boundary layer. The fully turbulent boundary layer is most likely the result of flow structure changes caused by the riblets and turbulence generated by the presence of riblets at the leading edge of the plate. Walsh (1990), in fact, implies that careful leading edge fairing is required to avoid premature transition of the boundary layer over a riblet surface. The test plate used had no such fairing. Another possible source of upstream turbulence was the seeding particle injection tubes. Turbulence generated by the presence of the tubes as well as the injection of seeding particles, however, is believed to have been slight, if any. The basis for this position is that the injection holes faced upstream and flow straightening screens were located between the injection tubes and the test section.

 Figure 16 shows the variation of turbulence intensity with y at the 400 mm station. Data was acquired both with an open and masked laser slot in order to examine the turbulence generated by the laser slot. With the slot masked, data was acquired

directly above a riblet peak, a riblet valley and a mid-slope point. With the slot open, data was acquired only above a riblet peak. In the figure, negative y values indicate points in the riblet valleys below the level of the riblet peaks. The masked slot freestream Tu level of approximately 2.0% is comparable to the 200 mm station data of Figure 15. Comparable levels between the two stations were expected since masking of the laser slot eliminated the primary source of additional freestream turbulence.

Just as in Figure 15, the masked slot peak boundary layer turbulence intensity in Figure 16 indicates a fully turbulent boundary layer. The suspected sources for a fully turbulent boundary layer are the same as presented above: flow structure changes caused by the riblets and turbulence generated by riblets at the leading edge. Figure 16 also shows that the largest masked slot Tu value occurs in the profile acquired directly above the riblet peak. This agrees with the findings of Nakagawa and Nezu (1982) and Vukoslavcevic et al. (1992) regarding the spanwise location of maximum turbulence intensity over a riblet surface.

The open slot data in Figure 16 shows noticeably higher Tu levels than the masked slot data both in and above the boundary layer. This trend was expected given the analogous results for the smooth plate data shown in Figure 10. In addition, the open slot freestream Tu level (3.5%) compares favorably, as expected, with the smooth plate open slot data in Figure 10 and with the Rothenflue's (1996) open slot test data discussed earlier. These increased Tu levels further demonstrate the undesired turbulence generated by an open laser slot.

4.3.3 Normal Velocity Profiles. Figure 17 shows the variation of u with y for both streamwise locations. The growth of the boundary layer is evident by the increase in

48

velocity defect for a given y at the 400 mm station. The 200 mm station $\delta_{99\%}$ is approximately 5.81 mm, 1.87 mm greater than the corresponding thickness for the smooth plate case. For the 400 mm station the $\delta_{99\%}$ is approximately 11.12 mm; an increase of 5.69 mm compared to the corresponding thickness for the smooth plate case. The increase in boundary layer thickness at both stations, as compared to the smooth plate case, results from the more turbulent nature of the boundary layer flow. White (1991) indicates that the boundary layer thickens considerably due to turbulence. The riblets are also believed to have contributed to the increase in boundary layer thickness through the presence of nested riblet-valley vortices. These vortices, which promote greater mixing and momenta transfer, are further discussed in this section with regards to Figures 20 through 27.

Figure 17 also shows that the riblets did not have a significant spanwise impact on u. Within 1 mm above the riblet peak, or about 0.1δ, the profiles acquired at the 400 mm station are coincident. Only in the immediate vicinity of the riblets can any differences between the profiles for each spanwise station be discerned. Differences between the velocity defect for each profile were directly related to the distance from the test surface. For instance, at a given y, the velocity defect for the valley spanwise location is less than those of the remaining two profiles. This is a result of the reduction in viscous effects at the valley spanwise location due to the greater distance from the test plate.

Figure 17 also provides information on the local skin friction coefficient, c_f. This quantity was estimated for each normal velocity profile with

$$c_f = \frac{\tau_w}{\frac{1}{2}\rho U^2} \tag{15}$$

The wall shear stress, τ_w, in this equation was found with Equation (3)

$$\tau_w = \mu \frac{\partial u}{\partial y}\bigg|_{y=0} \qquad (3)$$

The quantity $\partial u/\partial y$ was approximated for each profile with $\Delta u/\Delta y$ between the test surface and the first data acquisition location. The c_f estimates for the 200 mm and 400 mm stations are shown in Table 1.

Table 1. Favorable Pressure Gradient Local Skin-Friction Coefficients.

Station	Smooth Plate	Riblet Peak			Mid-Slope	Valley
	c_f	c_f	s^+	h^+	c_f	c_f
200 mm	0.0035	0.005605	48.3	41.86	-----	-----
400 mm	0.004828	0.00917	63.42	54.96	0.001908	0.001003

The c_f estimates in Table 1 show an increase in magnitude with x and, at the 400 mm station, with spanwise location from the riblet valley to the riblet peak. The increase in c_f with x at the riblet peaks is a non-intuitive result that does not conform to expectations. The increase from the valley location to the peak location agrees with the differences between the profiles in Figure 17 seen below y = 1 mm. The profiles clearly show a noticeable increase in $\partial u/\partial y$ between the valley and peak spanwise locations. The larger skin friction coefficient at the riblet peak also agrees with the larger shear stress at the riblet peak observed by Vukoslavcevic et al., (1992).

Also shown in Table 1 are local skin friction estimates for smooth plate, turbulent flow. These were obtained with

$$c_f = \frac{0.3e^{-1.33H}}{(\log_{10} Re_\theta)^{1.74+0.31H}} \qquad (16)$$

This equation represents a curve-fit of results obtained by White (1991) for Coles wall-wake law used in conjunction with the Karman Integral Relation. The quantity Re_θ is the Reynolds number based on momentum thickness and is defined by

$$Re_\theta = \frac{U\theta}{\nu} \tag{17}$$

The shape factor, H, is the ratio of displacement thickness to momentum thickness. Displacement thickness is defined by

$$\delta^* = \int_0^{y\to\infty} (1 - \frac{u}{U})dy \tag{18}$$

and momentum thickness is defined by

$$\theta = \int_0^{y\to\infty} \frac{u}{U}(1 - \frac{u}{U})dy \tag{19}$$

Momentum thickness and displacement thickness were calculated with velocity data acquired at each station over a riblet peak through numerical integration. The numerical integration technique used sectioned the area under the curves described by the integrands in Equations (18) and (19) into trapezoids. The quantity Re_θ was calculated with the resultant momentum thickness as well as the test flow U and kinematic viscosity. Consequently, the smooth plate local skin friction coefficients in Table 1 approximate those that would occur for smooth plate turbulent flow with the same u profiles as those observed in the tests. For the 200 mm and 400 mm stations, Re_θ was calculated to be 221.58 and 409.31, respectively. For the 200 mm and 400 mm stations, H was calculated to be 1.86 and 1.51, respectively.

Comparison of the smooth plate and riblet peak c_f values show that the riblet surface in the given flow conditions tends to increase skin friction drag compared to a

51

similar smooth plate flow. This result was expected given the non-dimensional riblet height and spacing for the two stations. These values, also shown in Table 1, were calculated with Equations (1) and (4) and the data acquired directly over the riblet peaks. As discussed in Section 2.3.2, Effects on Skin- Friction Drag, drag augmentation is expected for riblets with $h^+ > 15$ and $s^+ > 25$. As discussed below, only c_f estimates derived from data acquired over riblet peaks were compared due to the levels of uncertainty perceived for each spanwise location.

The accuracy of the c_f estimates for each spanwise station was limited by two factors. First, as stated by Young (1989), Equation (15) is applicable only to 2-D flows and can not account for the 3-D nature of flow in the vicinity of the riblets. Second, the use of $\Delta u / \Delta y$ to approximate $\partial u / \partial y$ is believed to have produced an estimate that was too small. This assumes a smooth variation of u with y directly adjacent to the riblet plate surface analogous to that for a smooth plate. The smaller estimate, in turn, could produce a smaller wall shear stress and a smaller estimate of c_f. In the calculations for s^+ and h^+, a smaller estimate of $\partial u / \partial y$ would have reduced s^+ and h^+ compared to their actual values. The amount of uncertainty in $\Delta u / \Delta y$ varied for each profile due to the differences in distance between the test surface and the closest data acquisition points. This is especially true at the 200 mm station and is directly responsible for the non-intuitive increase in c_f with x for the riblet peak profiles. Acquisition of data closer to the test surface would have produced a more accurate $\partial u / \partial y$ estimate for each profile. This, unfortunately, was not possible due to surface reflections, low seeding particle flux, steady flow problems and low laser power.

52

The assumption of a smooth variation of u with y adjacent to the riblet plate surface analogous to that of a smooth plate appears to best apply to the riblet peak spanwise location. This is based on the belief that the velocity profile directly above the riblet peak is less affected by the possible presence of vortical motion and more closely resembles that of a smooth plate than do the profiles above the valley and mid-slope locations. For the valley location, it appears intuitive that the velocity profile, and thus the wall shear stress estimate, will be impacted by viscous effects caused by the proximity of the sides of the valley. For the mid-slope profile, additional uncertainty is associated with the estimate of wall shear stress. Specifically, the use of Equation (3) implies that the variation of velocity $\partial u/\partial y$ will be found in a direction perpendicular to the surface. The data acquisition locations for the mid-slope spanwise location were not perpendicular to the surface.

Uncertainty is also present in the local skin-friction coefficient estimates for the smooth plate. This is seen in the non-intuitive increase in c_f with x. Three factors impact the accuracy of the local skin-friction coefficients for the smooth plate. First, the calculations of displacement and momentum thickness were impacted due to the relative lack of data immediately adjacent to the test plate surface. This lack of data resulted in an overestimation of the shape factor, and thus c_f, at the 200 mm station. Had data acquisition closer to the plate been possible, the resultant increase in accuracy of H at the 200 mm station may have reversed the non-intuitive trend in c_f. The second factor to impact the smooth plate c_f estimates is the fidelity of the numerical integration technique used. Last, White (1991) states that the curve-fit provided by Equation (16) is accurate to within $\pm 3\%$.

The velocity profiles of Figure 17 do not indicate the presence or absence of self-preserving flow. To assess flow similarity, the variation of measured velocity ratio, u/U, with non-dimensional normal distance, y/δ, was plotted for both streamwise stations. These profiles are shown in Figure 18. In the figure, the 200 mm station profile is similar to, but does not coincide with, the 400 mm station profile. This indicates that the flow was not self-preserving. As a result, it is difficult to distinguish between effects on boundary layer flow structure from nested vortical motion and pressure gradient and those caused by the variation of x. The absence of self-preserving flow was the direct result of the use of the same sidewall curvature as for the smooth plate case.

As discussed in Section 1.2, <u>Project Objectives</u>, the riblet plate turbulent flow was compared to the Law of the Wall region for a smooth plate, 2-D attached turbulent boundary layer. This was accomplished to examine flow differences due to the presence of riblets and nested riblet-valley vortices. To facilitate comparison, the measured u and y values were non-dimensionalized. The u values were non-dimensionalized with

$$u^+ = \frac{\overline{u}}{v*} \tag{6}$$

and the y values were non-dimensionalized with

$$y^+ = \frac{yv*}{v} \tag{7}$$

The friction velocity, v*, was calculated with

$$v* = \left(\frac{\tau_w}{\rho}\right)^{\frac{1}{2}} \tag{2}$$

where the wall shear stress was found with

$$\tau_w = \mu \frac{\partial u}{\partial y}\bigg|_{y=0} \qquad (3)$$

As before, the quantity $\partial u/\partial y$ was approximated for each profile with $\Delta u/\Delta y$ between the test surface and the first data acquisition location. To avoid negative y^+ values for data acquisition locations inside the riblet valley, 1.3 mm was added to all mid-slope y coordinates and 2.6 mm was added to all valley y coordinates. The non-dimensional velocity profiles are shown in Figure 19.

As discussed by White (1991), the Law of the Wall region for a smooth plate turbulent flow spans approximately the $0 \leq y^+ \leq 100$ range. This region consists of three subsections: the viscous sublayer ($0 \leq y^+ \leq 5$), the buffer layer ($5 \leq y^+ \leq 30$) and the inner portion of the overlap layer. The velocity profile in the law of the wall region for a smooth plate turbulent flow is described by the empirical equation of Spalding (1961), as shown by Equation (5). This equation is plotted in Figure 19 along with the linear velocity relationship of the viscous sublayer. This relationship is defined, as presented by White (1991), as

$$u^+ = y^+ \qquad (20)$$

The viscous sublayer for smooth plate turbulent flow is dominated by viscous shear stresses (White, 1991). In this region, flow structure is dependent on the wall shear stress, proximity to the surface and fluid properties and is independent of freestream parameters. Unfortunately, as seen in Figure 19, no data fell within this region due to the limited capability to acquire data near the test surface. The convergence of the various profiles toward the linear relationship of Equation (20) at low values of y^+, however, implies the presence of a viscous sublayer in the flow under study.

The velocity profile in the smooth plate buffer layer is a smooth merge between linear and logarithmic relationships between u^+ and y^+ (White, 1991). With the exception of the profiles acquired directly above riblet peaks, Figure 19 shows that the measured velocity profiles differed significantly from the smooth plate profile in the buffer layer. Some agreement between the linear behavior described by Equation (20) and the 400 mm mid-slope and 400 mm valley profiles does occur. This behavior, unexpected for a smooth plate buffer layer, implies the importance of viscous stresses to the riblet plate turbulent flow structure in this region. This trend, however, is contradicted by the 200 mm peak and 400 mm peak velocity profiles that more closely approximate the logarithmic relationship between u^+ and y^+ described by Spalding's (1961) equation. These profiles imply the increasing importance of eddy stresses in this region. Based on their similarity to the data of Debisschop and Nieuwstadt (1996), the profiles acquired above the riblet peaks are believed to be more indicative of the actual flow structure.

A primary factor for the differences between the measured profiles and the smooth plate velocity profile is the 3-D nature of the observed riblet boundary layer. As discussed previously, the velocity profile described by Spalding's (1961) equation, see Equation (5), applies only to a smooth plate 2-D attached turbulent boundary layer. Also, Equations (6) and (7) can not take into account the 3-D flow structure near the riblet surface. This 3-D structure, characterized for this test plate and flow by nested riblet-valley vortices, is discussed in detail in conjunction with Figures 20 through 27. In addition, the transfer of momenta and mixing induced by riblet-valley vortices is believed to have affected the boundary layer velocity profile adjacent to the test plate.

A second source for the differences between the riblet and smooth plate velocity profiles are limitations associated with Equation (3). Assuming that the behavior of $\partial u/\partial y$ for the riblet plate is similar to that for a smooth plate, the use of $\Delta u/\Delta y$ to approximate $\partial u/\partial y$ produces an estimate that is too small compared to expectations. This carries through the calculation of friction velocity with Equation (2) and, in turn, produces a u^+ value that is larger than expected. As discussed in regards to c_f estimates, the amount of uncertainty in $\partial u/\partial y$ estimate varied for each profile due to the differences in distance between the test surface and the closest data acquisition point. Acquisition of data closer to the test surface would have produced more accurate $\partial u/\partial y$ estimates and possibly profiles with a relationship between u^+ and y^+ more like that of the smooth plate.

A third factor that is believed to have created differences between the riblet and smooth plate velocity profiles is the difficulty in the definition of the $y = 0$ point for a riblet plate. This can clearly be seen in the differences in the three 400 mm station profiles in Figure 19. Differences in the vicinity of the riblets, such as those in Figures 17 and 18, were expected for profiles at the same streamwise station. Above the near-wall region, the profiles were expected to coincide. As stated previously, the valley and mid-slope y coordinates were shifted to avoid the creation of negative y^+ values for acquisition locations inside the riblet valleys. This shift produced y^+ values erroneously large. Bechert and Bartenwerfer (1980), Suzuki and Kasagi (1994), Walsh (1982) and others have expressed uncertainty as to an appropriate y origin for a riblet plate.

As presented by White (1991), the flow structure in the smooth plate overlap layer ($35 \leq y^+ \leq 350$) is influenced by both viscous and eddy stresses. In Figure 19, the profiles only show a qualitative agreement with the smooth plate profile. Specifically, each curve

57

contains a straight portion comparable to the logarithmic relationship between u^+ and y^+ exhibited for a flat plate. However, the slope of the straight line portions of each curve, with the exception those corresponding to riblet peaks, are significantly different from the slope shown in Spalding's (1961) equation. Based on the work of Debisschop and Nieuwstadt (1996), the curves for each spanwise location were expected to approximate Spalding's (1961) equation for much of the overlap layer. The differences among the profiles and between the profiles and Spalding's (1961) equation are attributed to the sources discussed above: the inability of Equations (6) and (7) to include the 3-D nature of the riblet boundary layer, uncertainty in the estimates of $\partial u/\partial y$ used in Equation (3) and the difficulty in the definition of the $y = 0$ location for a riblet surface.

Figures 20 and 21 show the variation of v with y directly above a riblet peak at the 200 mm and 400 mm streamwise stations, respectively. The riblet peak was located at $y = 0$ mm on both figures. The primary feature of these figures is the positive v values, or upwash, near the test plate surface. This is consistent with Rothenflue's (1996) observations of upwash near riblet peaks with riblet-valley vortices present. Vortical motion, however, is confirmed only with the presence of the appropriate cross-stream velocity components. Thus, the figures indicate the possibility that riblet-valley vortices have formed or begun to form.

For both Figures 20 and 21, the upwash decays with increasing y from a peak value near the test surface. In Figure 20, the upwash spans over 50% of the boundary layer and decays to zero at approximately 3.5 mm. In Figure 21, the upwash decays to zero at about 1.5 mm, slightly more than 10% of the boundary thickness at that streamwise station. This may indicate the upper boundary of vortical motion and is

consistent with the vortex dimensions observed by Rothenflue (1996). In addition, the data from these two figures indicates that the riblet-valley vortices may be oval-shaped. The larger upwash at the 200 mm station may be indicative of the flow structure prior to or during vortex formation. Alternatively, the reduced upwash at x = 400 mm may be the result, as discussed previously, of the reduced outflux through the masked slot's laser windows at that station.

Two additional observations can be made about Figures 20 and 21. First, both figures display peak upwashes of approximately 2.5 %. This may be indicative of constant vortex strength. Also, both figures possess a small, relatively constant upwash in the freestream. This freestream upwash is believed to be due to an outflux through the masked slot's laser windows. The freestream upwash is slightly stronger at the 200 mm station, indicative of the greater outflux that would be expected at that streamwise location for a favorable pressure gradient.

Figure 22 shows the variation of v with y directly above a riblet valley at the 400 mm station. The local downwash, or negative v values, into the valley in the vicinity of y = 0 mm is consistent with Rothenflue's (1996) observations of vortical flow at this spanwise location. As discussed previously, this downwash, in and of itself, does not conclusively prove the presence of vortical motion. The boundaries of the upwash are approximately y = 1.5 mm and y = -1 mm, respectively. The upper boundary is consistent with the vortex dimensions observed by Rothenflue (1996). The decay to v = 0 at y = -1 mm indicates an area of low-speed flow adjacent to the test plate surface. In addition, the peak local downwash (approximately -2 %) located at approximately y = 0.5 mm may indicate the y coordinate of the center of the nested vortices. Figure 22

59

also shows a freestream upwash believed to be the result of outflux through the laser windows. The magnitude of the upwash agrees well with that of Figure 21.

Figure 23 shows the variation of v with y at the 400 mm station directly above the mid-slope point, halfway between the riblet peak and riblet valley. Although Rothenflue (1996) acquired no data at this spanwise location, the velocity data below y = 3 mm is consistent with his observations of nested vortical flow structure. Specifically, below y = 0.5 mm, the suspected center of the vortex, a local upwash develops to an approximate peak value of 2 % at y = -0.5 mm. This peak upwash subsequently decays as the y coordinate decreases to -1.3 mm, the location of the test plate surface. Combined with the w profiles in Figure 27, this trend indicates the flow followed the contour of the riblet from the valley to the peak spanwise location. This agrees with the vortical motion shown in Figure 2. In addition, a local downwash is observed between y = 0.5 mm and y = 3 mm. The maximum downwash is approximately -1.0 % at approximately y = 1 mm. The downwash decays to v = 0, the approximate upper boundary of the vortex at this spanwise location, near y = 3 mm. This trend also agrees with the vortical motion described in Figure 2.

Figure 24 shows the variation of w with y at the 200 mm station directly above a riblet peak. This profile does not directly indicate the presence of vortical motion. From the observations of Rothenflue (1996), no spanwise velocity component was expected directly above a riblet peak. Figure 24 shows a peak spanwise velocity component of approximately 0.75% above the peak that decays to zero and then increases negatively to a -1 % peak at approximately y = 2.0 mm. In turn, this negative spanwise component decays to zero at approximately 4.0 mm. This unexpected flow structure may be the

60

result of turbulence or may indicate that nested vortical motion has not fully developed at this station. Another potential source is the possible presence of a spanwise pressure gradient. Branam (1997) found that the test section was susceptible to spanwise pressure gradients that produced v and w components of approximately 1% to 3%. Potential sources for this spanwise pressure gradient include the flow entering the top of the stilling chamber from the pressurized seeder plenum and curvature in the flexible sidewall. Above y = 4.0 mm, a positive spanwise drift develops and then decays further into the freestream. This drift may be the result of the same sources.

Figure 25 shows the variation of w with y at the 400 mm station directly above a riblet peak. In this figure, the unexpected, secondary flow structure seen in Figure 24 is repeated to a lesser extent. Specifically, the development and decay of a negative spanwise shear of -0.75 % is present between y = 1 mm and y = 3 mm. With the exception of this secondary flow structure, no indications contrary to the presence of nested vortices are observed. Above y = 4 mm, virtually no spanwise shear is present, as expected.

Figure 26 shows the variation of w with y directly above a riblet valley at the 400 mm station. This profile shows a negative shear bubble between y = 2 mm and y = 4 mm similar to that seen in Figures 24 and 25. Below approximately y = 2 mm, virtually no spanwise shear is present. This is consistent with the observations of Rothenflue (1996) for vortical flow behavior at this spanwise location. As before, no significant spanwise shear is present above y = 4 mm, as expected.

Figure 27 shows the variation of w with y directly above the mid-slope location at the 400 mm station. Although Rothenflue (1996) did not acquire data at this spanwise

location, the flow behavior adjacent to the test surface in this figure strongly agrees with his description of nested riblet-valley vortices. For this profile, the nearest riblet peak was in the negative z direction. Thus, the negative spanwise shear located below y = 0 mm indicates flow toward the riblet peak as would be expected for nested vortical motion. The negative spanwise shear reaches a peak of about -1.25% at approximately y = -0.5 mm. Above this y coordinate, the shear decays to zero at approximately y = 0.5 mm, the suspected center of vortical motion at this spanwise location. Above y = 0.5 mm, the spanwise velocity component increases to a peak of about 0.75% at y = 1.0 mm and indicates a reversal of flow toward the valley spanwise location. Above this y coordinate, the spanwise shear decays and develops the same secondary flow structure between y = 2.0 mm and y = 4.0 mm seen in Figures 24 through 26. The upper edge of the vortex at this spanwise location occurred at approximately y = 2 mm. Above y = 4.0 mm, little spanwise shear is observed, as expected.

4.3.4 Spanwise Velocity Profiles. Figures 28 through 33 show the variation of u, v and w with z at both streamwise stations. Velocity distributions were acquired at y = 0.6 mm and 0.8 mm above the riblet peaks at the 200 mm station and at y = 0.5 mm and 0.8 mm above the riblet peaks at the 400 mm station. These locations were chosen based on an assumed vortex diameter of approximately 1.5 mm (1/2 the riblet spacing, s) and to coincide with locations where vortical flow patterns in v and w were anticipated. The figures are constructed so that riblet peaks correspond to z values of 3.0 mm, 0 mm and -3.0 mm. Riblet valleys correspond to z values of -1.5 and 1.5 mm.

Figures 28 and 29 show the spanwise variation of u for the two streamwise stations. The sine wave-like appearance of the profiles indicates the viscous effects that

62

resulted from the proximity of the data acquisition point to the test plate surface. Minimum u values occurred directly above riblet peaks. This observation is consistent with the data of Hooshmand et al. (1983), who found minimum u values directly above riblet peaks for a zero pressure gradient turbulent flow. This trend was expected since the acquisition locations were closest to the test plate and subsequently experienced the greatest viscous effects. Maximum values of u occurred directly above riblet valleys, as expected, since their acquisition locations were farthest from the plate surface and experienced the least viscous effects. The data in both figures show, as expected, a reduction in velocity defect with increase in normal coordinate. In addition, a comparison between the y = 0.8 mm profiles of the two figures shows less variation of u with z at the 400 mm station. Rothenflue (1996) observed the same trend. This may be the result of mixing and momenta transfer induced by the formation of nested vortices.

Figures 30 and 31 show the spanwise variation of v at the two streamwise stations. Both figures show maximum upwash near the riblet peaks and maximum downwash near the riblet valleys. This influx at the riblet valley and outflux at the riblet peak agrees with Rothenflue's (1996) observations of vortical motion and supports the presence of vortices. A comparison of the profiles show that the peak velocity magnitudes at the 400 mm station decreased slightly compared to the peak 200 mm station velocities. The profiles also show abrupt changes and scatter not seen in Figures 28 and 29. This resulted from the combination of smaller velocities and turbulence. Greater scatter in the data was anticipated due to the magnitude of the velocity components compared to the magnitude of the velocity fluctuations due to turbulence. As discussed by Young (1989), turbulent flow velocity fluctuations can be on the order of

a tenth of the mean flow velocity. Scatter in the data, here and elsewhere, may have also resulted from particle location ambiguity and low data validation rates, as discussed in Appendix J, Data Acquisition Parameters.

Figures 32 and 33 show the spanwise variation of w at both streamwise stations. The figures show similar peak magnitudes and the characteristic variation in velocity expected for vortical motion (Rothenflue, 1996). Combined with the variations of v observed in Figures 30 and 31, these profiles indicate the presence of nested vortices. The presence of these nested vortices enhances momentum transfer near the wall and indicates drag-augmentation (Suzuki and Kasagi, 1994). The more clearly defined variation seen in Figure 33 implies that vortex formation is in process at the 200 mm station. In addition, the peak measured velocities of roughly ±1% are approximately 50% of the peak v component magnitudes in Figures 30 and 31. The smaller magnitudes may be the result of greater physical constraints on spanwise motion provided by the riblets and adjacent vortices. The maximum vortical strength is approximately 2.2% of the freestream velocity. Scatter in the profiles is attributed to the same causes discussed for Figures 30 and 31.

4.4 Riblet Plate, Adverse Pressure Gradient Case

To avoid undesired turbulence generation, data for this test case was acquired with a masked laser slot.

4.4.1 Freestream Velocity Profile. Figure 34 shows the variation of U with x for this case. An adverse pressure gradient was produced in the test section by the adjustment of sidewall curvature until the desired power-law freestream velocity distribution was obtained. The power-law freestream velocity distribution is described by

$$U = Kx^m \qquad \qquad (21)$$

The quantity m is the power-law parameter and is analogous to the Falkner-Skan power-law parameter (White, 1991). The quantity m was chosen to be approximately -0.07 in order to produce a moderate adverse pressure gradient corresponding to a Falkner-Skan pressure gradient parameter, β, of -0.15. A constant K of approximately 4.469 was required to produce a 5 m/s freestream velocity at a streamwise coordinate of 100 mm. The magnitude of the pressure gradient corresponding to this velocity distribution was estimated to be 6.616 Pa/m ($2.92 \cdot 10^{-4}$ psi/ft) with Equations (9) and (10). The velocity distribution calculated with Equation (21) is shown in Figure 34 along with the measured data. Excellent agreement between the two data sets was achieved. Production of this velocity distribution verified the capability of the modified BLRF to produce specific non-zero pressure gradients.

4.4.2 Turbulence Profile Results. Figures 35 and 36 show the variation of turbulence intensity at the 200 mm and 400 mm streamwise stations, respectively. Turbulence profiles were acquired directly above a riblet peak, a riblet valley and a mid-slope point at both stations. In the figures, negative y values indicate points in the riblet valleys below the level of the riblet peaks.

Several significant observations can be made from a comparison of Figures 35 and 36 to the analogous favorable pressure gradient figures, Figures 16 and 17. First, the adverse pressure gradient freestream Tu level is higher, approximately 2.5%, than the 2.0% level for the favorable pressure gradient case. Also, the adverse pressure gradient freestream data is more scattered. Both of these effects are attributed to flow through the masked slot's two open laser transmission windows. With the adverse pressure gradient,

these windows are believed to have induced an influx into the test section due to the static pressure differential with the laboratory. The mixing associated with this influx caused greater freestream velocity fluctuations and thus higher Tu levels and scatter. These effects are most noticeable in the 200 mm station data of Figure 35. The influx at that station was believed to be more pronounced due to the greater pressure differential with the laboratory air.

Similar to Figures 16 and 17, Figures 35 and 36 also show fully turbulent boundary layers at both streamwise stations. This is indicated by peak Tu values of approximately 9% at both stations. The fully turbulent boundary layer is attributed to the same sources as with the favorable pressure gradient case: flow structure changes due to the riblets and possible turbulence generation at the test plate leading edge due to the presence of riblets. Both Figures 35 and 36 also show the trend observed in Figure 16: peak Tu levels occurred directly above the riblet peak spanwise station. This agrees with the findings of Nakagawa and Nezu (1982), Vukoslavcevic et al. (1992) and others.

Figures 35 and 36 show the presence of thicker boundary layers than those observed in Figures 16 and 17. This trend is apparent at both streamwise stations. In addition, Figures 35 and 36 show a wider range of y coordinates inside the boundary layer with higher Tu values than in Figures 16 and 17. This is indicated by the profile shape and is especially prominent in Figure 36. The thicker, more turbulent boundary layers in Figures 35 and 36 are directly attributable to the presence of an adverse pressure gradient (Young, 1989).

4.4.3 Normal Velocity Profiles. Figure 37 shows the variation of u with y at both streamwise locations. The data in this figure was acquired directly above the mid-slope

66

point. The boundary layer growth with x is evident from the increased velocity defect at the 400 mm station. In the figure, $\delta_{99\%}$ is approximately 9.44 mm and 15.81 mm for the 200 mm and 400 mm stations, respectively. Compared to Figure 17, the boundary layer thickness increased by 3.63 mm and 4.69 mm at the 200 mm and 400 mm station, respectively. In addition, both profiles of Figure 37 show a slight, but noticeable, slope discontinuity near y = 5 mm. This change may be indicative of a boundary between strata within the riblet plate boundary layer. No such change was observed in Figure 17.

The profiles from Figure 37, along with those for the riblet peak and valley spanwise locations, were used to estimate local skin-friction coefficients. Equation (15) was used to estimate the c_f values at the 200 mm and 400 mm stations. The results are shown in Table 2.

Table 2. Adverse Pressure Gradient Local Skin-Friction Coefficients.

Station	Smooth Plate	Riblet Peak			Mid-Slope	Valley
	c_f	c_f	s^+	h^+	c_f	c_f
200 mm	0.003029	0.003462	37.29	32.89	0.001461	0.000986
400 mm	0.003822	0.006551	50.35	43.64	0.001663	0.000975

The results in Table 2 show the same trends as those in Table 1. Specifically, with the exception of the riblet valley spanwise location, local skin friction coefficient increased with x at the same spanwise location. As with the favorable pressure gradient case, this increase in c_f with x was a non-intuitive result. This is a direct result of the fact that data could not be acquired as close to the riblet surface at the 200 mm station as compared to the 400 mm station. The consequence of this lack of data was an underestimated value for wall shear stress. In addition, c_f values increased with

proximity to the riblet peak as was seen in the favorable pressure gradient case and by

Vukoslavcevic et al., (1992). Last, each c_f value in this case is less than the

corresponding value for the favorable pressure gradient case. Underestimated values of

wall shear stress for the adverse pressure gradient case are the source of this anomalous

trend. These underestimated values resulted from the fact that data could not be acquired

as close to the plate surface for this case, at either streamwise station, as could be done

for the favorable pressure gradient case.

Also shown in Table 2 are local skin friction estimates for smooth plate, turbulent

flow. These were obtained with the same equations and methodology used for the

favorable pressure gradient case. Consequently, they approximate turbulent flow over a

smooth plate with the same velocity profiles as those observed in the tests. For the 200

mm and 400 mm stations, Re_θ was calculated to be 357.85 and 629.28, respectively. For

the 200 mm and 400 mm stations, H was calculated to be 1.83 and 1.56, respectively.

Just as with the favorable pressure gradient case, comparison of the smooth plate and

riblet peak c_f values show that the riblet surface in the given flow conditions tended to

increase skin friction drag compared to a similar smooth plate flow. This result was

expected given the non-dimensional riblet height and spacing for the two stations, as

shown in Table 2. As discussed in Section 2.3.2, Effects on Skin- Friction Drag, drag

augmentation was expected for riblets with $h^+ > 15$ and $s^+ > 25$.

Uncertainty is present in the local skin-friction coefficient estimates for the

smooth plate. This is seen in the non-intuitive increase in c_f with x. Just as with the

favorable pressure gradient case, this trend was due to the impacts on displacement and

momentum thickness from the relative lack of data immediately adjacent to the test plate

surface. This lack of data resulted in an overestimation of the shape factor, and thus c_f, at the 200 mm station. Had data acquisition closer to the plate been possible, the resultant increase in accuracy of H at the 200 mm station may have reversed the non-intuitive trend in c_f. Additional sources of uncertainty include the fidelity of the numerical integration technique and the accuracy of Equation (16).

As with Figure 17, Figure 37 shows does not indicate the presence or absence of self-preserving flow. To examine flow similarity, the variation of velocity ratio, u/U, with non-dimensional normal distance, y/δ, was plotted for both streamwise stations. These profiles are shown in Figure 38. The close agreement between the profiles indicates a self-preserving flow. This allows for examination of effects on boundary layer flow structure by vortical motion and adverse pressure gradient independent of x.

As with the favorable pressure gradient case, the measured adverse pressure gradient velocity data was recast in terms of the dimensionless inner-law variables, u^+ and y^+, to compare the riblet flow to the Law of the Wall region for a smooth plate. The conversion was accomplished with Equations (6) through (7) and the same methodology used for the favorable pressure gradient case. Just as with the favorable pressure gradient case, the mid-slope and valley spanwise location y values were shifted upward to eliminate negative y^+ values. Figure 39 shows the non-dimensionalized velocity profiles along with Spalding's (1961) equation and the viscous sublayer velocity profile for the smooth plate, Equations (5) and (20), respectively.

Just as with the favorable pressure gradient data in Figure 19, difficulty with data acquisition near the test surface virtually precluded measurements below $y^+ = 5$. Only one point, from the 400 mm mid-slope location, was acquired in this region. Each

69

profile, however, did tend to converge toward the linear relationship of Equation (20) at small y^+ values. Again, the presence of a viscous sublayer for the riblet plate was implied.

In the buffer layer ($5 \leq y^+ \leq 30$), the same trends observed in the favorable pressure gradient data (Figure 19) are observed in Figure 39. Specifically, the peak profiles at both stations exhibit behavior indicative of a logarithmic relationship between u^+ and y^+ and the mid-slope and valley profiles tend toward the linear relationship of Equation (20). As with the favorable pressure gradient case, the similarity of the peak profiles to the data of Debisschop and Nieuwstadt (1996), imply that these profiles are more indicative of the actual flow structure.

The differences between the smooth plate and the riblet plate profiles in Figure 39 are again attributed to the 3-D nature of the riblet plate flow and uncertainty in the $\partial u/\partial y$ estimates. As in Figure 19, Figure 39 also shows significant differences between profiles at the same streamwise station. This is again attributed to the shift in y coordinates for the mid-slope and valley profiles and the uncertainty as to an appropriate y origin. Some variance with the smooth plate profile, however, is expected given the conclusion of Debisschop and Nieuwstadt (1996) that the standard logarithmic velocity law is not valid in an adverse pressure gradient.

Trends similar to those observed in Figure 19 for the overlap layer are also seen in Figure 39. Specifically, the profiles at each station differ significantly with each other and with Spalding's (1961) equation, given as Equation (5). Each curve, however, does exhibit a straight line portion like those seen in Figure 19. As with the curves in Figure 19, however, the slope of these straight portions vary substantially between the curves

70

and with Spalding's (1961) equation. The best agreement with Spalding's equation occurs for the two peak profiles. The differences are attributed to the same sources previously discussed: the inability of Equations (6) and (7) to include the 3-D nature of the riblet boundary layer, uncertainty in the estimates of $\partial u/\partial y$ used in Equation (3) and the difficulty in the definition of the y = 0 location. In addition, despite the presence of self-preserving flow, the corresponding profiles for the two stations did not collapse onto the same curve as was be expected. This indicates that the lack of self-preserving flow for the favorable pressure gradient case was not the source of the differences in profiles between streamwise stations.

A direct comparison between the profiles of Figure 19 and Figure 39 shows that profiles for the same spanwise location tend to be of the same shape. In addition, the best quantitative agreement occurs for profiles at the same spanwise and streamwise locations. This is noticeably evident for the 400 mm peak profiles and the 400 mm mid-slope profiles. Quantitative agreement, especially for the two 400 mm mid-slope profiles, extends almost to the outer edge of the boundary layer. Consequently, the results imply that a significant portion of the flow structure is independent of external pressure gradient. This is analogous to the known smooth plate turbulent boundary layer flow structure (White, 1991).

Figures 40 through 42 show the variation of v with y at the 200 mm streamwise station directly above a riblet peak, a riblet valley and the mid-slope point, respectively. Two significant observations can be made from these figures. First, each figure displays a significant amount of freestream downwash (-v component) onto the test plate surface. The downwash increases in magnitude with distance from the test plate and is very

similar above approximately y = 7 mm in all three figures. This tends to support the presence of an influx into test section through the masked slot's laser windows.

The second significant observation from Figures 40 through 42 is that data is consistent with the presence of riblet-valley vortices. In Figure 40, the downwash induced by the laser window decays to zero at approximately y = 2.0 mm. Between this point and the riblet peak, v is positive and indicates the local upwash expected above the riblet peak for vortical motion. The peak upwash magnitude is approximately 1.5%, significantly less than the 2.5% peak observed in Figure 20. In Figure 41, the downwash onto the plate decays to only -1% and indicates the local downwash expected above the riblet valley for vortical motion. This may indicate that the downwash affected vortex formation. Figure 42 shows a velocity profile with trends similar to those in Figure 23. Specifically, an upwash toward the riblet peak appears near the test plate surface. Directly above y = 0, a local downwash is present. The downwash decays to zero at y = 2 mm, the assumed upper boundary of the vortex at this spanwise location. This upper boundary is consistent with the vortex dimensions observed by Rothenflue (1996).

Figures 43 through 45 show the variation of v with y at the 400 mm streamwise station directly above a riblet peak, a riblet valley and a mid-slope point, respectively. As with Figures 40 through 42, each figure shows a noticeable downwash onto the test surface that increases with distance from the plate. Also, there is good agreement between the downwash of the three figures above approximately y = 6 mm. This downwash, however, is less severe than that seen in Figures 40 through 42. This is believed to the result of the smaller static pressure differential between the test section

72

and the laboratory at the 400 mm station. As a result, the assumed influx through the masked slot's laser windows was less than that at the 200 mm station.

Just as in Figure 40, the data trends in Figure 43 are consistent with nested vortical motion. Specifically, the observed downwash decays to zero at approximately the same $y = 2.0$ mm coordinate, below which a local upwash adjacent to the riblet peak is seen. This upper boundary is again consistent with the vortex dimensions observed by Rothenflue (1996). It is of interest to note that the magnitude of the peak local upwash, approximately 0.75%, is less than that observed at the 200 mm station despite the reduced downwash. With the assumption that the acquired peak upwash was the maximum actually present, this implies that the adverse pressure gradient degraded vortex formation as the flow progressed. This is consistent with the observations of Branam (1997) for the same riblet plate in similar flow conditions.

Figure 44 also shows flow behavior at the valley spanwise location consistent with the nested, counter-rotating vortices observed by Rothenflue (1996). Specifically, a local downwash was observed. The magnitude of the local downwash, however, was slightly less than that observed in the 200 mm station data of Figure 41. As discussed above, this indicates that the adverse pressure gradient degraded vortex formation as the flow traveled along the test plate.

Figure 45 shows the characteristic velocity variation adjacent to the riblets indicative of vortical motion at the mid-slope location. A local upwash adjacent to the test surface (below $y = 0$ mm) is observed as well as its decay to zero at approximately $y = 0.5$ mm, the approximate center of the nested vortical motion. A local downwash occurs above this point. This behavior, however, is not as defined as that observed in the

73

200 mm station data in Figure 42. Again, this indicates a degradation of vortical motion between the two stations attributable to the action of the adverse pressure gradient.

Figure 46 shows the variation of w with y at the 200 mm station directly above a riblet peak. Close to the test surface, the spanwise velocity component is zero, as expected at this spanwise location for nested vortical motion (Rothenflue, 1996). As y increases, the spanwise velocity component develops to a negative drift of approximately -0.5%. This drift remains virtually constant for the remainder of the profile. The cause of this drift is believed to be an influx through the masked slot's open laser windows or a spanwise pressure gradient. As discussed previously, Branam (1997) found the test section susceptible to spanwise pressure gradients. Potential sources for this spanwise pressure gradient include flow entering the top of the stilling chamber from the pressurized seeder plenum and sidewall curvature. No secondary flow structure, as observed in Figure 24, was observed.

Figure 47 shows the variation of w with y at the 200 mm station directly above the riblet valley spanwise location. The data in this figure shows no spanwise component near the test plate. This is consistent with Rothenflue's (1996) observations of vortical flow behavior at this spanwise station. A negative spanwise shear above the area of vortical motion is also present in this figure. Compared to Figure 46, however, this spanwise shear only begins to develop above y = 7 mm, never exceeds -0.25 % and virtually disappears in the freestream. The differences between this drift and that of Figure 46 combined with the fact that the two profiles were obtained in separate tests indicate that the drift is not a constant flow feature. As in Figure 46, there is no

secondary flow structure above the nested vortices as observed in the favorable pressure gradient case.

Figure 48 shows the variation of w with y at the 200 mm station directly above the mid-slope spanwise location. The variation of the spanwise velocity component near the test surface is similar to that of Figure 27. This behavior, consistent with the observations of Rothenflue (1996), indicates the presence of nested riblet-valley vortices. The size of the observed vortex is also similar to that seen in Figure 27. Specifically, the center of the vortical motion at this spanwise location was at approximately y = 0.5 mm and the upper limit of the observed vortical motion was approximately y = 2.0 mm. With the same riblet plate and similar flow conditions, Branam (1997) mapped vortex centers at approximately y = 0.4 mm. In addition, the magnitudes of the peak spanwise components for both figures are similar. These similarities may indicate that the fully formed vortices, regardless of external pressure gradient, develop to approximately the same size and strength. Also, the figure shows a nearly constant negative spanwise shear of -0.5 % above y = 2.0 mm. The possible causes of this drift are as previously discussed for Figure 46: influx through the laser windows and the presence of a spanwise pressure gradient. Last, no secondary flow structure above the riblet-valley vortices was observed as in the favorable pressure gradient case.

Figure 49 shows the variation of w with y directly above a riblet peak at the 400 mm station. Unlike Figure 46, the spanwise velocity near the test surface is non-zero. This is not strictly consistent with the expected flow behavior for nested vortical motion at this spanwise station (Rothenflue, 1996). For vortical motion, a zero spanwise velocity at this station would be expected. The spanwise component of approximately

0.5% decays with y and reaches zero at y = 12 mm. Above y = 12 mm, there is no spanwise velocity component present. This indicates that the cross-stream velocity component near the test plate is most likely associated with a spanwise pressure gradient instead of the influx through the laser windows. The observed velocity behavior, therefore, does not negate the presence of vortical motion.

Figure 50 shows the variation of w with y at the 400 mm station directly above the valley spanwise location. This profile displays similarities to Figure 49. Specifically, a positive spanwise velocity is present near the test surface that decays with y to zero at y = 12.0 mm. The peak spanwise drift in this case is approximately 1.5 % and is attributed to the presence of a spanwise pressure gradient. As with Figure 49, this spanwise drift does not strictly agree well with Rothenflue's (1996) observations of nested vortical flow behavior at this spanwise station. Near y = 0 mm, several locations have small cross-stream velocity components that could indicate flow conditions similar to nested vortical motion. The apparent spanwise drift effectively masks vortical motion indicators.

Figure 51 shows the variation of w with y directly above the mid-slope spanwise location at the 400 mm station. As with Figures 49 and 50, this profile shows a significant positive cross-stream velocity component near the test plate surface. This positive drift also decayed with y to zero near y = 12 mm. The peak local drift value is approximately 1.5 %. This profile, however, does show a flow structure somewhat indicative of vortical motion near the riblet surface. However, the indicated vortex is distorted and flattened compared to the vortex observed in Figure 48. The positive drift

and degraded vortical motion may have been the result of a spanwise pressure gradient, the effects of the adverse pressure gradient, or a combination of both.

4.4.4 Spanwise Velocity Profiles. Figures 52 through 57 show the variation of u, v and w with z at the 200 mm and 400 mm streamwise stations. Velocity distributions were acquired at y = 0.6 mm and 0.8 mm above the riblet peaks.

Figures 52 and 53 show the spanwise variation of u at the 200 mm and 400 mm stations, respectively. The sine wave-like variation of the velocity data in both figures indicates the expected variation of viscous effects with distance above the test plate surface. Specifically, the minimum u values occurred directly over riblet peaks and the maximum values occurred directly above riblet valleys. As with the favorable pressure gradient case, this observation is consistent with the data of Hooshmand et al. (1983), who found minimum u values located directly above riblet peaks and maximum u values directly above riblet valleys in a turbulent, zero pressure gradient flow. The data in both figures also shows the expected reduction in velocity defect with increase in normal coordinate. In addition, the peak u values at the 400 mm station are less than those observed at the 200 mm station. This is consistent with the increase in velocity defect between the two stations shown in Figure 37. As observed in the analogous favorable pressure gradient data (Figures 28 and 29), the figures show a reduction in the variation of u with z at the 400 mm station. This agrees with the data of Rothenflue (1996) and is assumed to have been caused by the mixing and momenta transfer induced by the riblets. For this case, the reduction in u variation was more pronounced than that observed for the favorable pressure gradient case.

77

Figures 54 and 55 show the spanwise variation of v at the two streamwise stations. Both figures show the characteristic spanwise variation of velocity expected for vortical motion: maximum upwash near the riblet peak and maximum downwash near the riblet valley. Compared to the analogous figures for the favorable pressure gradient case (Figures 30 and 31), the figures show similar peak magnitudes and a similar decrease in peak velocity magnitudes at the 400 mm station. The similarity in peak magnitudes may indicate that vortex strength is independent of pressure gradient. Just as with the favorable pressure gradient case, data quality was adversely affected by the combination of turbulence, small velocity magnitudes, particle location ambiguity and low data validation rates.

Figures 56 and 57 show the spanwise variation of w above the riblet peaks at both streamwise stations. Despite the degree of scatter present, both figures show the characteristic variation of w expected for vortical motion. Combined with the velocity variation observed in Figures 54 and 55, the profiles confirm the presence of nested vortices. As with the favorable pressure gradient case, presence of these nested vortices indicated drag-augmentation (Suzuki and Kasagi, 1994). Branam (1997) later confirmed this with the same riblet plate and similar flow conditions.

Compared to the analogous favorable pressure gradient data (Figures 32 and 33), however, the characteristic variation of w in Figure 57 is not as clearly defined. This may indicate that the adverse pressure gradient tends to degrade vortex formation as the flow progresses. With the same riblet plate and similar flow conditions, Branam (1997) experimentally verified this effect. The approximately ±1 % peak w magnitudes, however, are similar to those observed in Figures 32 and 33. This further indicates that

vortex strength may be independent of pressure gradient. As with the favorable pressure gradient case, the size of the peak w magnitude compared to the peak v magnitude (approximately 50 %) is attributed to the greater physical constraints in the spanwise direction. The maximum vortical strength for this case is also approximately 2.2% of the freestream velocity. Scatter in Figure 56 and 57 is attributed to the causes discussed above and was exacerbated by the smaller w velocity magnitudes.

V. Conclusions and Recommendations

5.1 Conclusions

5.1.1 Flow Study Conclusions.

1. In both riblet test cases, maximum boundary layer Tu levels occurred in the vicinity of riblet peaks. This concurs with the findings of Nakagawa and Nezu (1982), Vukoslavcevic (1992) and others.

2. Compared to Rothenflue's (1996) data, the overall freestream Tu levels were reduced. This resulted from the masking of the laser slot, a significant source of freestream turbulence.

3. In the adverse pressure gradient case, a discontinuity in the local u profile slope was observed near y = 5 mm at both streamwise acquisition stations. This discontinuity may indicate a boundary within the riblet boundary layer between strata subject to different flow influences. No such velocity profile slope discontinuity was observed for the favorable pressure gradient case.

4. For Law of the Wall comparisons, qualitative agreement with the findings of Debisschop and Nieuwstadt (1996) was achieved for velocity profiles acquired directly above riblet peaks. In addition, portions of all profiles showed a logarithmic relationship between u^+ and y^+. Similarities between the favorable and adverse pressure gradient dimensionless velocity profiles implied that a large portion of the riblet boundary layer flow structure was independent of external pressure gradient. This is analogous to the smooth plate case (White, 1991).

5. In comparisons with the smooth plate Law of the Wall region, trends in measured velocity profiles at low y^+ values for both the favorable and adverse pressure gradient cases implied the presence of a viscous sublayer for riblet plate turbulent boundary layer. An area of quiescent flow beneath the nested riblet-valley vortices was also implied in normal velocity profile data.

6. The non-dimensional velocity profiles for the riblet plate boundary layer differed significantly from the smooth plate Law of the Wall region. Differences between profiles and with Spalding's (1961) equation are attributed to three sources: the inability of the non-dimensional wall variables to account for the 3-D nature of the riblet boundary layer, uncertainties in the estimates of wall shear stress, and the difficulty in the definition of an appropriate $y = 0$ point for a riblet surface. For the adverse pressure gradient case, differences are also attributed to the inapplicability of the standard logarithmic velocity law to an adverse pressure gradient as stated by Debisschop and Nieuwstadt (1996).

7. The cross-stream and normal velocity components characteristic of nested vortical motion were observed in both the favorable and adverse pressure gradient cases. Incomplete vortex formation was observed at the 200 mm station for the favorable pressure gradient case. The presence of these riblet-valley vortices and the associated penetration of higher momentum fluid into the riblet valley were indicative of drag-augmentation (Suzuki and Kasagi, 1994). This was later experimentally verified by Branam (1997).

8. The more distinct vortical flow structures for the adverse pressure gradient case at the 200 mm station may have been aided by the influx of laboratory air through

the laser transmission windows. Spanwise and normal velocity profiles at the 400 mm station implied that the adverse pressure gradient degraded nested vortical motion as the flow progressed. Branam (1997) later experimentally verified this.

9. Velocity profiles for both cases showed that the nested, counter-rotating vortices were oval shaped. Specifically, both cases showed a vortex center at y = 0.5 mm with an observed outer vortex boundary at y = 2.0 mm. The upper boundary is consistent with the observations of Rothenflue (1996). Below the vortex center, both cases showed that the vortical motion tended to follow the contours of the riblet valley. The location of the vortex center agreed well with the findings of Branam (1997).

10. The negative shear bubble in favorable pressure gradient normal velocity profiles and noticeable spanwise drift in adverse pressure gradient normal profiles indicate the presence of an unknown, transient flow within the test section. Possible sources include flux through the laser transmission windows and a spanwise pressure gradient initiated upstream of the test section or by lack of sidewall spanwise symmetry. The pressurized seeder plenum added to the BLRF configuration is one possible upstream source of spanwise pressure gradient. Branam (1997) verified the susceptibility of the test section to spanwise pressure gradients.

11. The strength of the fully developed nested riblet-valley vortices observed in both cases was similar. These results imply that vortex strength is relatively independent of external pressure gradient magnitude. In addition, the spanwise velocity profiles for both the favorable and adverse pressure gradient cases showed that maximum w magnitudes were roughly 50% of maximum v magnitudes.

12. In both the favorable and adverse pressure gradient cases, the spanwise u and v profiles showed a reduced degree of variation with z at the 400 mm station. This reduction in variation was more pronounced for the adverse pressure gradient flow. This phenomenon, also observed by Rothenflue (1996), is believed to be the result of the mixing and momenta transfer induced by the nested vortices.

13. Calculations of the non-dimensional riblet height and spacing for both pressure gradients indicated the riblet plate, under the given flow conditions, increased skin-friction drag. This is consistent with the presence of vortical motion, agrees with the findings of Djenidi and Antonia (1996) and met initial expectations.

14. Riblet flow c_f values were found to increase in magnitude from the valley spanwise location to the riblet peak location. This agrees with the larger shear stress at the riblet peak observed by Vukoslavcevic et al., (1992).

5.1.2 Apparatus and Procedures Conclusions.

1. A new test section for the BLRF was designed, fabricated and assembled. The new test section provided the capability to create and study low-speed flows with specific non-zero streamwise pressure gradients. The capabilities of the test section and the accuracy of the LDA system were verified through the re-creation of the Blasius solution and the acquisition of a self-preserving adverse pressure gradient flow.

2. The BLRF was de-coupled from the AFIT cascade facility. This de-coupling provided greater flexibility in the use of both facilities and augmented the ability of the system's flow regulator to maintain steady conditions.

3. A new seeding particle injection method for the BLRF was implemented. The top-mounted seeder plenum and injection tubes provided a more controlled injection of

83

seeding particles into the area of interest compared to the method of Rothenflue (1996). As a result, fewer seeding particles had to be injected. The reduction in seeding particles reduced concerns with safety and equipment damage and facilitated the use of the LDA system's automatic data acquisition mode. Use of the automatic acquisition mode saved a significant amount of time and reduced procedural complexity.

4. The critical importance of the cleanliness of the air supply's air filter was identified. The original dirty filter caused such significant upstream pressure fluctuations that steady flow conditions could only be maintained for brief periods during the first two-thirds of the project.

5. A simple method to align the BLRF, test section and traverse with an inclinometer and a template was developed. This method provided a common, convenient coordinate system that eliminated complexity and potential errors in the velocity data transformation process.

6. A significant deficiency in laser power was discovered. The source of the deficiency was identified as contaminated internal laser mirrors. Although no hardware corrective action could be implemented, innovative procedures to compensate for the lack of power were identified and incorporated. These procedures included the exchange of fiber plugs to minimize line loss impacts, the redistribution of available laser power between wavelengths and power balancing with the Bragg cell and focusing rings. These innovative procedures were critical to produce acceptable data acquisition rates. With the exception of Bragg cell adjustment, none of these techniques were presented in any DANTEC system documentation.

7. A new method to form the measurement volume was developed. This technique relied upon visual observation for initial probe volume formation and used the actual seeded test flow for fine tuning. The new method required substantially less time to produce the same quality probe alignment as previous methods.

8. A new technique to locate the test surface was developed. For this technique, a telescope, laser safety goggles and test plate markings were used to visually align the probe volume in the streamwise and spanwise directions. This technique significantly reduced test surface location time.

9. A typographical error in the matrix multiplication order of the velocity transformation matrices presented by Rothenflue (1996) was identified and corrected.

10. A new combination of particle generator and seeding material was used for flow seeding. Compared to the DANTEC fogger/Rosco fog fluid combination previously used, the atomizer/olive oil combination used in this project significantly increased data acquisition rates. Without this new combination, acceptable acquisition rates would not have been possible. The atomizer/olive oil combination also facilitated the use of the LDA system's automatic data acquisition mode.

11. Power levels measured at the input and output of the fiber optics transmission cables revealed excessive line losses. These line losses exacerbated the low data acquisition rates produced by the deficiency in laser power.

5.2 Recommendations

5.2.1 Flow Study Recommendations.

1. The new capability of the BLRF to create specific non-zero streamwise pressure gradients provides a wealth of opportunities to study the effects of riblets on

boundary layers. Future flow studies should examine how different combinations of pressure gradients, riblet geometry and flow velocity affect turbulent boundary layer characteristics and vortex size, shape and strength. The pressure gradients to be studied should include self-preserving and realistic non-self-preserving non-zero pressure gradients.

2. Future projects should extend this research to examine pressure gradient-riblet effects on Görtler vortex formation over curved, riblet plates with constant and realistic non-constant wall curvatures.

3. Initial vortex formation in relation to the onset of flow transition should be studied. This would require that normal and spanwise velocity profiles be acquired at a greater number of streamwise stations than in this project. Acquisition of normal and spanwise profiles at a greater number of streamwise stations would also provide an opportunity to more fully characterize riblet boundary layer flow.

4. To better quantify riblet-valley vortex size, shape and strength, a comprehensive 2-D survey of the flowfield within and immediately above the riblet valleys should be conducted. An extensive survey would also provide data on the types and extent of subregions within the riblet turbulent boundary layer analogous to those present in smooth plate turbulent boundary layer. The survey could also facilitate the development of useful empiricisms to predict time-averaged flow characteristics such as skin-friction drag, velocity distribution, momentum thickness, displacement thickness and mean turbulence parameters.

5.2.2 Apparatus and Procedures Recommendations.

1. Low laser power was a significant problem encountered in this project. With increased laser power, data acquisition rates could possibly be maximized so that only the characteristics and number of injected seeding particles would limit acquisition rates. Increased acquisition speed would provide time for additional test runs to build confidence in repeatability, eliminate suspect measurements and obtain a more comprehensive description of the flows under study. With increased laser power, the quality factor, pedestal attenuation and software filters could be used to enhance data quality, increase data validation rates and reduce particle location ambiguity. Substitution of a higher power laser could allow a balanced power level fixed at the same value for each beam pair. Equal balanced power levels would eliminate the significant disparity in data acquisition rates between the three wavelengths and facilitate data acquisition closer to the riblet surface, a critical requirement for accurate skin-friction estimates.

2. Little research on seeding particle material was conducted. Research into the effects of seeding particle size and reflectivity properties could uncover an alternative material to further improve data acquisition rates and quality.

3. The new method for seeding particle injection resulted in the localized injection of particles near the test plate surface. However, most of the seeding particles injected with the new method did not pass through the measurement region. More precise injection could increase the flux of particles near the test surface and better facilitate data acquisition in the vicinity of the riblets. In addition, more precise injection would reduce the amount of seeding particles required and the associated costs and wear

on the particle generator and seeder plenum interior. Fewer seeding particles would also reduce the amount of particles ejected into the laboratory air and, in turn, reduce the risk of damage to test equipment, especially the laser. More precise injection could be accomplished with changes to the number, size and location of injection holes in the injection tubes, a re-positioning of the injection tubes or the replacement of the tubes with a smoke wand.

4. Precise adjustment of the amount of flow vented upstream of the flow regulator was difficult due to the external vent valve's poor operational condition and purge valve's relative lack of sensitivity. Repair or replacement of the external vent valve and the installation of a fine tuning vent valve would eliminate this difficulty. The fine tuning vent valve would be inserted into the system parallel with the external vent valve (Bowman, 1996). The improved ability to adjust the amount of vented flow would result in significant time savings for the establishment of steady flow test conditions.

5. Replacement of the air supply system's air filter required the work of two people over the course of several hours. A fast, simple method to replace the filter should be developed to facilitate frequent changes of this critical component.

6. During the early stages of the project, a drop in upstream pressure below the minimum 68 psi level damaged the air supply compressors. This was unintentionally caused by excessive venting. Several weeks of valuable test time were lost while the compressors were repaired. To prevent a recurrence of this situation, the air supply system should be equipped with a fail-safe switch to automatically stop flow to the laboratories in the event of an excessive drop in upstream pressure.

7. The installation of a fiber optics link between the laser and transmitter would significantly improve the optics alignment and optimization process. The link would replace the need to adjust the base of the laser and transmitter in favor of the adjustment of beam manipulator knobs. This would produce more precise laser and transmitter alignment in less time and with greater power transmitted to the probe volume. The link would also prevent possible damage to the transmitter from the influx of particles through the open beam entry port. A link of this type is currently available from DANTEC.

8. Alignment of the 3-D traverse system with the test section could be improved with the fabrication of a traverse base with individually adjustable corner legs. Individually adjustable legs could be used to minimize the α, β, and γ rotation angles and minimize velocity transformation errors.

9. The complete masking of the laser slot would eliminate the effects on the test section flow caused by flux through the laser passage windows. This would require that the beams pass through a solid material between the probes and the measurement volume. Research should be conducted to determine how laser passage through a solid material would affect probe volume formation, data acquisition and power losses.

10. Turbulence generated at the test plate leading edge most likely had two sources: the wedge-like test plate leading edge geometry and the presence of riblets at the leading edge. A new test plate with a rounded or elliptical leading edge and more gradual flow direction changes could reduce the generation of turbulence (Buter, 1996). Re-location of the riblet starting point downstream of the leading edge could also reduce turbulence generation.

11. The Burstware® program exhibited problems with velocity units, the uncommanded shifting of center frequencies, the sporadic display of real-time histograms and a non-functional software coincidence filter. To facilitate robust, trouble-free data acquisition, new data acquisition software should be acquired. Weissman (1996) indicated that improved versions of the Burstware® program are currently available.

12. The Burstware® program provided only a primitive vector plot capability. A more advanced graphics post-processing program could greatly enhance interpretation of vortex size, shape and strength data and would ease 2-D mapping of the flow inside riblet valleys.

13. The measured fiber optics line losses could be significantly reduced through replacement of the lines or a thorough cleaning of the cable end-tips. Reduced line losses would significantly increase data acquisition rates and facilitate use of software coincidence filters and other options for data quality improvement.

14. Data acquisition near the riblet surface was impeded by strong surface reflections. A test plate fabricated without highly reflective flat spots at the peak and valley locations would enhance data acquisition near the test surface.

15. A detailed characterization of the new test section should be conducted to determine the source and magnitude of suspected spanwise pressure gradients.

Bibliography

1. Barlow, R. S. and J. P. Johnston. "Roll-Cell Structure in a Concave Turbulent Boundary layer," AIAA paper 85-0297, AIAA 23rd Aerospace Sciences Meeting, Reno, January, 1985.

2. Bechert, D. W. and M. Bartenwerfer. "The Viscous Flow on Surfaces with Longitudinal Riblets," Journal of Fluid Mechanics, vol. 206, pp. 105-129

3. Bowman, Jerry W. Associate Professor, Air Force Institute of Technology, Wright-Patterson AFB OH. Personal Interview. 12 November 1996.

4. Branam, Richard D. "Velocity Profiles and Skin Friction on a Ribletted Flat Plate in Adverse Pressure Gradient," MS These GAE/ENY/97D-01. School of Engineering, Air Force Institute of Technology (AU), Wright-Patterson AFB OH, December 1997.

5. Bushnell, Dennis M. "Introduction," Viscous Drag Reduction in Boundary Layers. vol. 123, Progress in Astronautics and Aeronautics, edited by Dennis M. Bushnell and Jerry N. Heffner, Washington: AIAA 1990.

6. Buter, Thomas A. Assistant Professor, Air Force Institute of Technology, Wright-Patterson AFB OH. Personal Interview. 22 October 1996.

7. Coustols, M. and A. M. Savill. "Turbulent Skin-Friction Reduction by Active and Passive Means," Special Course on Skin Friction Drag Reduction, AGARD report no. 786, Loughton, Essex: Specialized Printing Services Limited, 1992.

8. DANTEC Measurement Technology A/S. "User's Guide: 57N20/57N35 BSA Enhanced." Skovlunde, Denmark: DANTEC, Inc.

9. DANTEC Measurement Technology A/S. "User's Guide: 60X Series FiberFlow®." Skovlunde, Denmark: DANTEC, Inc.

10. DANTEC Measurement Technology A/S. "Burstware 2.0® User's Manual." Skovlunde, Denmark: DANTEC, Inc.

11. Debisschop, J. R., and F. T. M. Nieuwstadt. "Turbulent Boundary Layer in an Adverse Pressure Gradient: Effectiveness of Riblets," AIAA Journal, vol. 34, no. 5, AIAA, NY, May 1996, pp. 932-937.

12. Djenidi, L. and R. A. Antonia. "Laser Doppler Anemometer Measurements of Turbulent Boundary Layer over a Riblet Surface," AIAA Journal, vol. 34, no. 5, AIAA, NY, May 1996, pp. 1007-1012.

13. Floryan, J. M. "Görtler Instability of Boundary Layers," National Aerospace Laboratory Technical Report, TR-1120-T, Tokyo: National Aerospace Laboratory, 1991.

14. Hooshmand, D., R. Youngs, J. M. Wallace. "An Experimental Study of Changes in the Structure of a Turbulent Boundary Layer Due to Surface Geometry Changes," AIAA Paper 83-0230, Jan. 1983.

15. Luker, Joel J. "Experimental Investigation of a Supersonic Boundary Layer including Favorable Pressure Gradient Effect," MS These GAE/ENY/95D-16. School of Engineering, Air Force Institute of Technology (AU), Wright-Patterson AFB OH, December 1995.

16. Kalburgi, V. S. M. Mangalam, J. R. Dagenhart. "Görtler Instability on an Aerofoil: Comparison of Marching Solution With Experimental Observations," AGARD-CP-438, paper no. 8, Specialized Printing Services Limited, Essex, England, 1989.

17. Kramer, Stuart C. Class handout, MECH 423, Dynamics of Aerospace Systems. School of Engineering, Air Force Institute of Technology, Wright-Patterson AFB OH, July 1995.

18. Nakagawa, H. and I. Nezu. "Coherent Structures in Open-Channel Flow," Structure of Turbulence in Heat and Mass Transfer, edited by Z. P. Zaric, Hemisphere, Washington, DC, 1982, pp. 431-450.

19. Park, S. R. and J. M. Wallace. "Flow Alteration and Drag Reduction by Riblets in a Turbulent Boundary Layer," AIAA Journal, vol. 32, no. 1, AIAA, NY, January 1994, pp. 31-38.

20. Rioux, Dan. Aero/Astro Lab Technician, Air Force Institute of Technology, Wright-Patterson AFB OH. Personal Interview. 12 September 1996.

21. Roberson, John A. and Crowe, Clayton T. Engineering Fluid Mechanics. Boston: Houghton Mifflin Company, 1985.

22. Rothenflue, J. A. and P. I. King. "Vortex Development Over Flat Plate Riblets in a Transitioning Boundary Layer," AIAA Journal, vol. 33, no. 8, AIAA, NY, August 1995, pp. 1526-1526.

23. Rothenflue, James A. Executive Officer, AFRL Directed Energy Directorate, Kirtland AFB NM. Telephone Interview. 12 September 1996.

24. Rothenflue, James A. Riblet Effects on Görtler Vortex Development over a Concave Surface. Air Force Institute of Technology (AU), Wright-Patterson AFB OH, February 1996.

25. Spalding, D. B. "A Single Formula for the Law of the Wall," <u>Journal of Applied Mechanics</u>, vol. 28, pp. 455-457.

26. Sundaram, S., P. R. Viswanath and S. Rudrakumar. "Viscous Drag Reduction Using Riblets on NACA 0012 Airfoil to Moderate Incidence," <u>AIAA Journal</u>, vol. 34, no. 4, AIAA, NY, April 1996, pp. 676-682.

27. Suzuki, Y. and N. Kasagi. "Turbulent Drag Reduction Mechanism Above a Riblet Surface," <u>AIAA Journal</u>, vol. 32, no. 9, AIAA, NY, September 1994, pp. 1781-1790.

28. Thompson, Scott. Service Technician, Ion Laser Technology, Inc., Salt Lake City UT. Telephone Interview. 11 September 1996.

29. Vukoslavcevic, P., J. M. Wallace and J. L. Balin. "Viscous Drag Reduction Using Streamwise-Aligned Riblets," <u>AIAA Journal</u>, vol. 30, no. 4, AIAA, NY, April 1992, pp. 1119-1122.

30. White, Frank M. <u>Viscous Fluid Flow</u>. New York: McGraw-Hill, Inc., 1991.

31. White, Frank M. <u>Heat and Mass Transfer</u>. Reading: Addison-Wesley, 1988.

32. Walsh, Michael J. "Riblets," <u>Viscous Drag Reduction in Boundary Layers</u>. vol. 123, Progress in Astronautics and Aeronautics, edited by Dennis M. Bushnell and Jerry N. Heffner, Washington: AIAA 1990.

33. Walsh, Michael J. "Turbulent Boundary Layer Drag Reduction Using Riblets," AIAA Paper 82-0169, January 1982.

34. Weissman, Cliff. National Sales Manager, DANTEC Measurements, Inc., Mahwah, NJ. Personal interview. 31 October 1996.

35. Weissman, Cliff. National Sales Manager, DANTEC Measurements, Inc., Mahwah, NJ. Telephone interview. 29 August 1996.

36. Young, Alec D. <u>Boundary Layers</u>. Washington, D.C.: American Institute of Aeronautics and Astronautics, 1989.
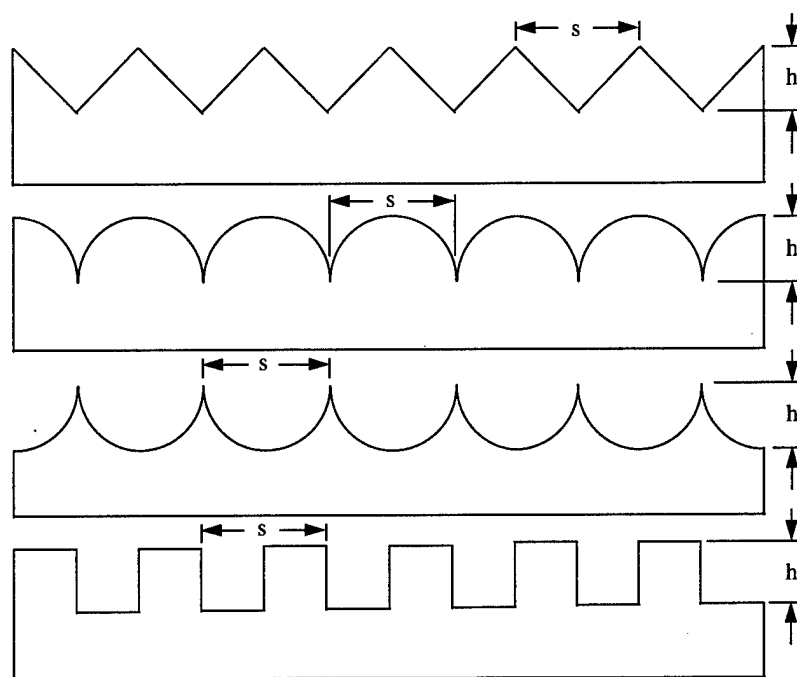
Figure 1. Common Riblet Shapes.
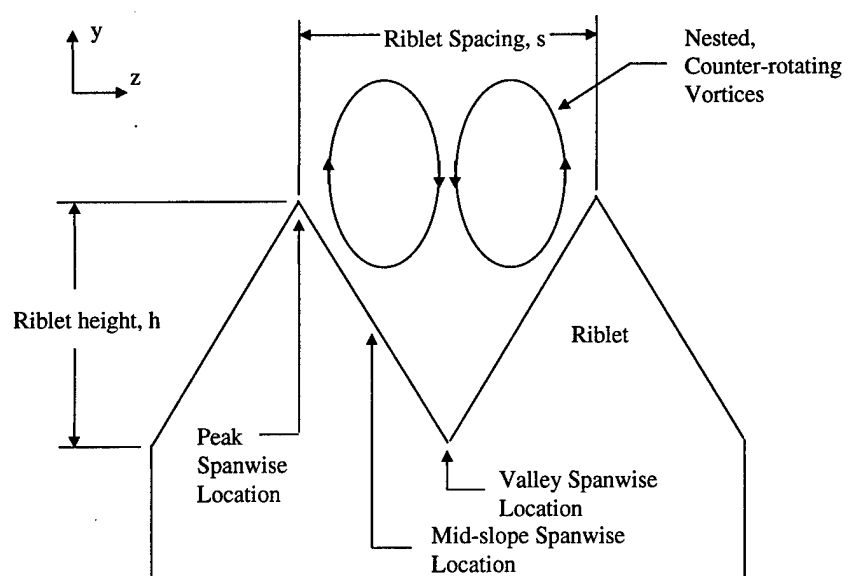
Figure 2. Riblet Cross-Section with Nested Counter-Rotating Vortices.
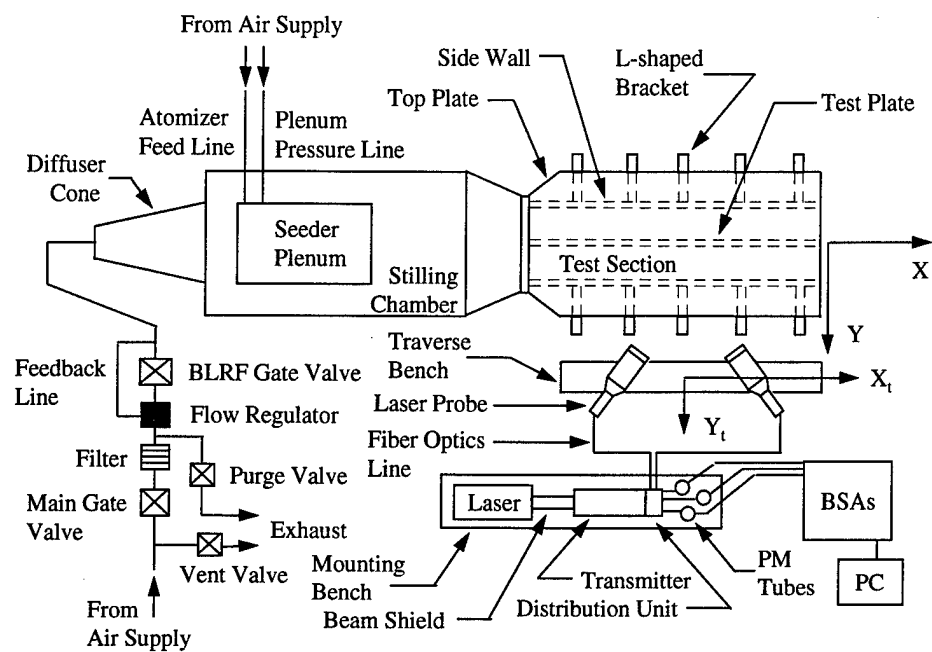
Figure 3. BLRF Schematic (Top View)

Top View

Leading Edge Detail
Top View

Leading Edge Detail
Side View

Leading Edge Detail
Front View
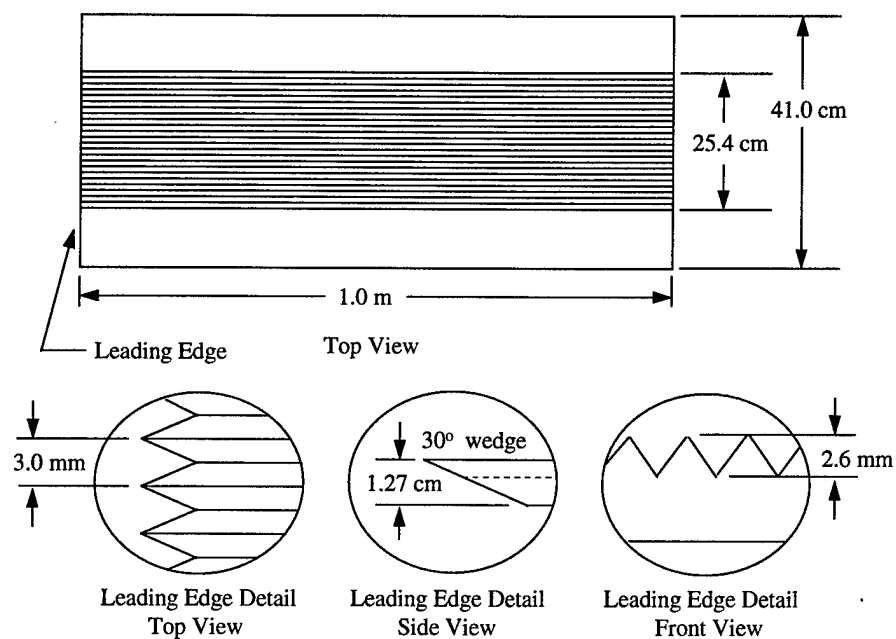
Figure 4. Riblet Test Plate
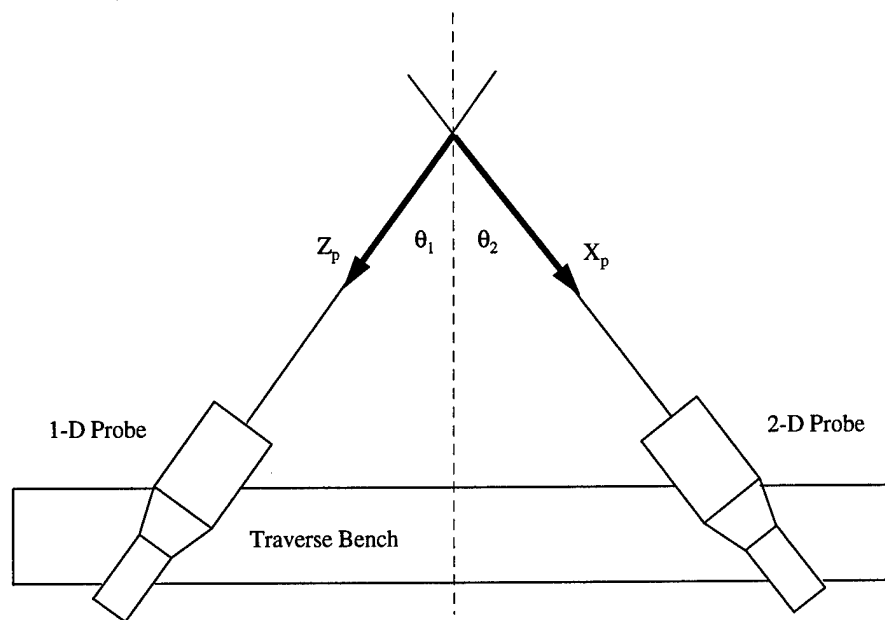
Figure 5. Probe Coordinate System
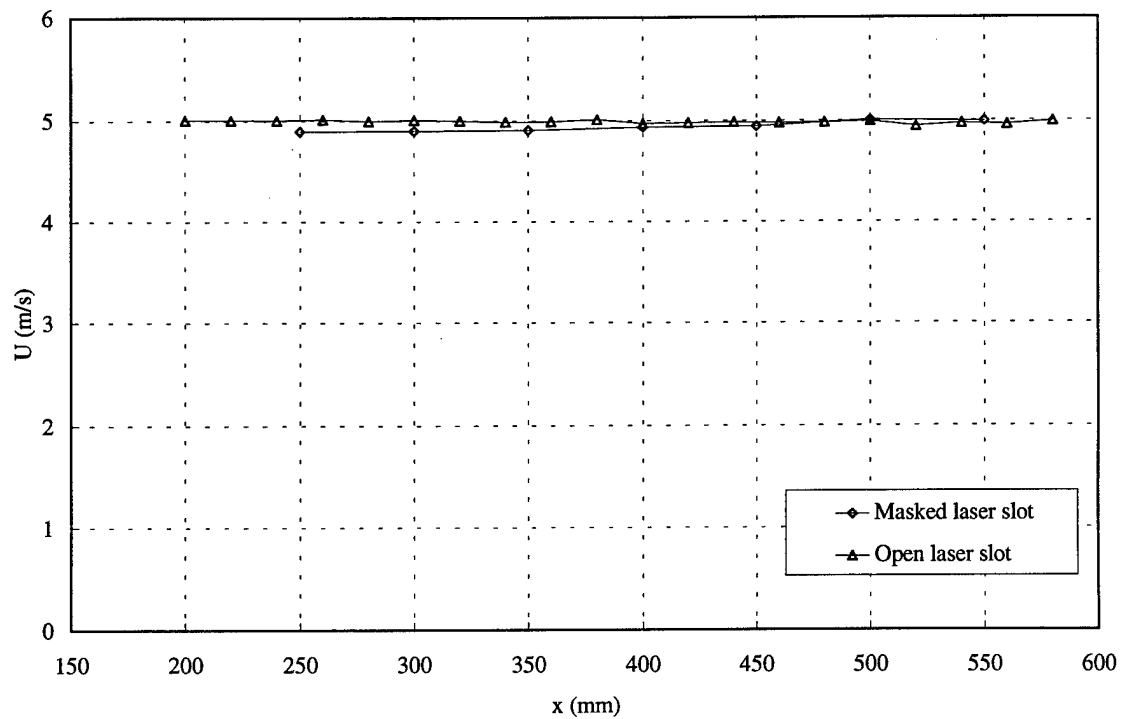
Figure 6. Freestream velocity, smooth, ZPG, y = 30 mm
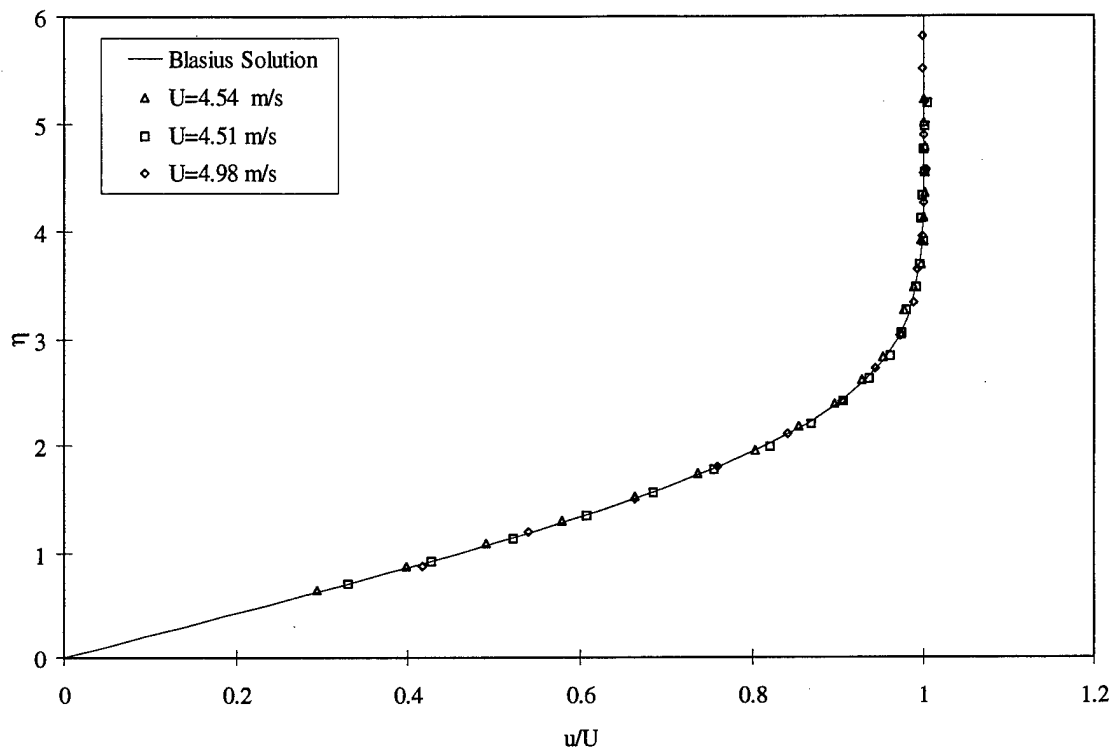
Figure 7. Blasius solution duplication, smooth, ZPG, 200 mm, open slot
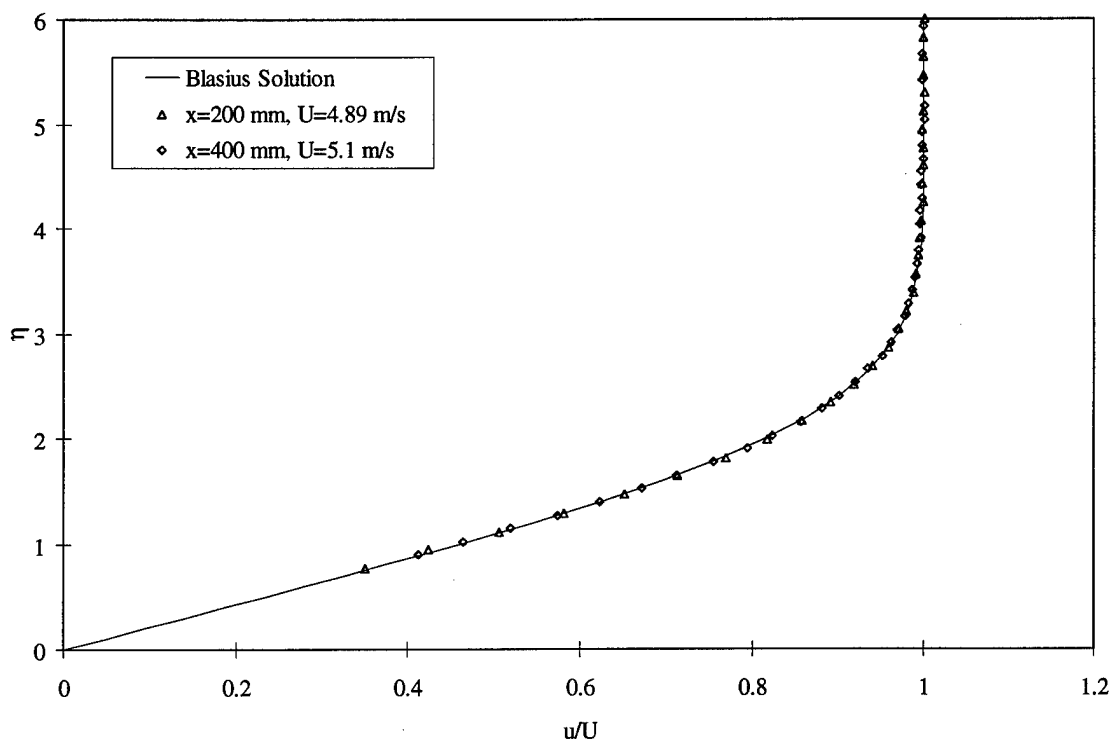
Figure 8. Blasius solution duplication, smooth, ZPG, masked slot
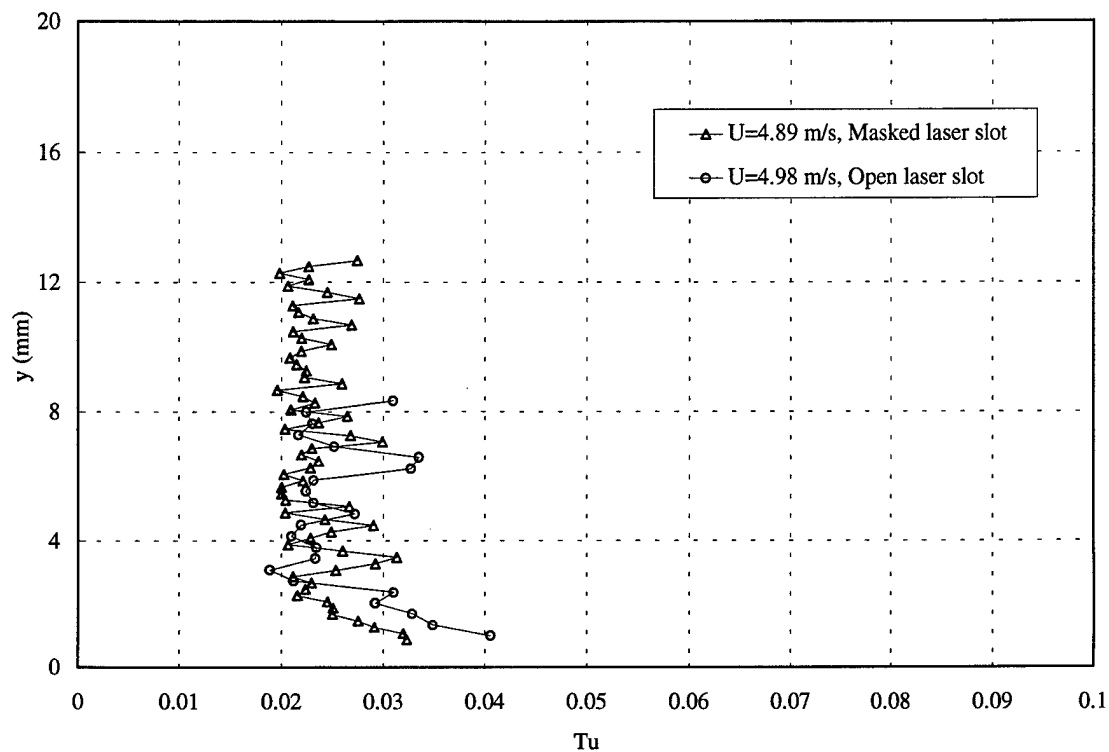
Figure 9. Turbulence intensity, smooth, ZPG, 200 mm
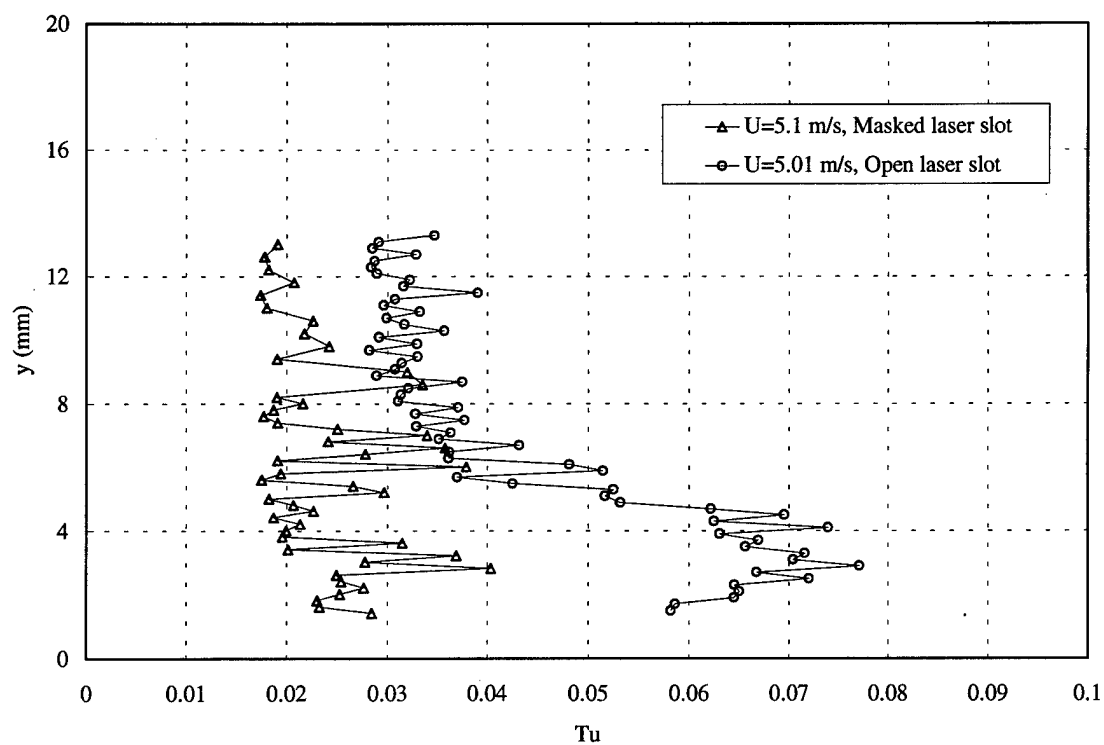
Figure 10. Turbulence intensity, smooth, ZPG, 400 mm
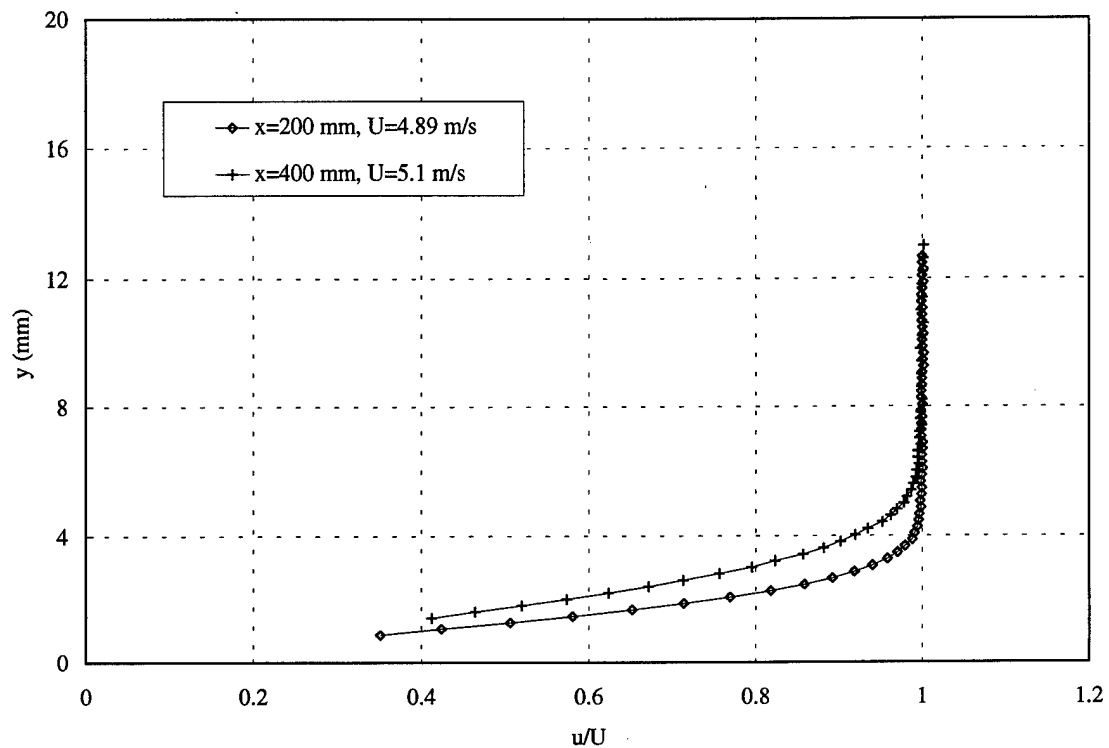
Figure 11. u profile, normal direction, smooth, ZPG
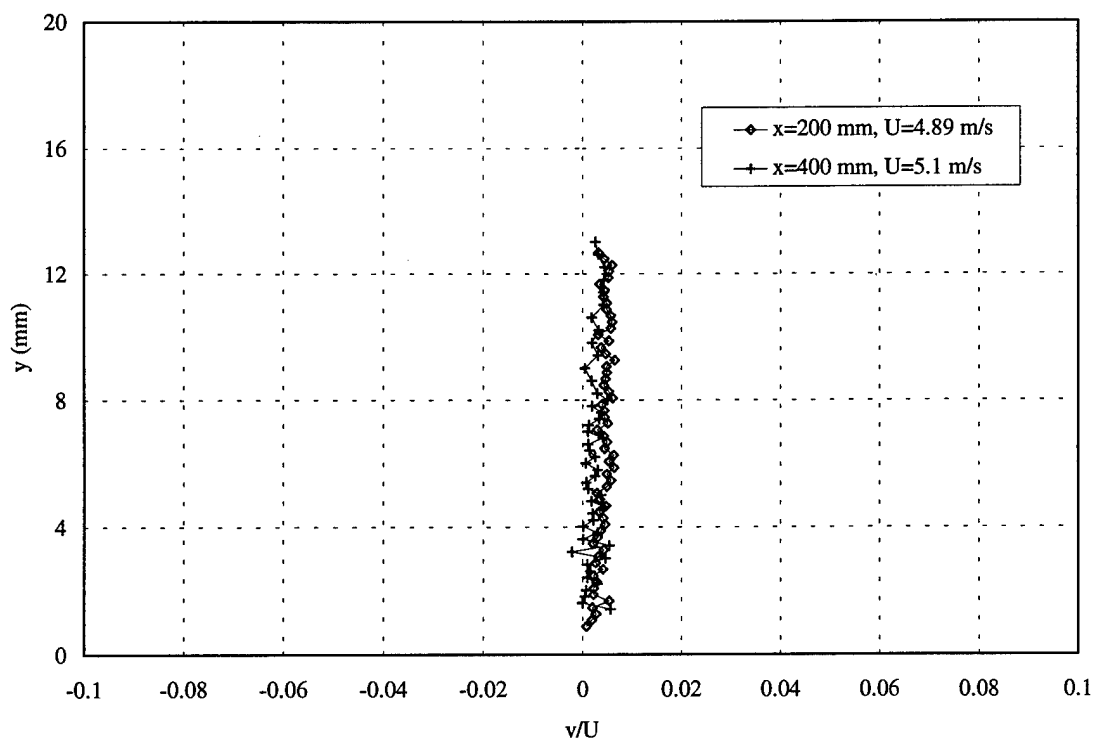
Figure 12. v profile, normal direction, smooth, ZPG

99
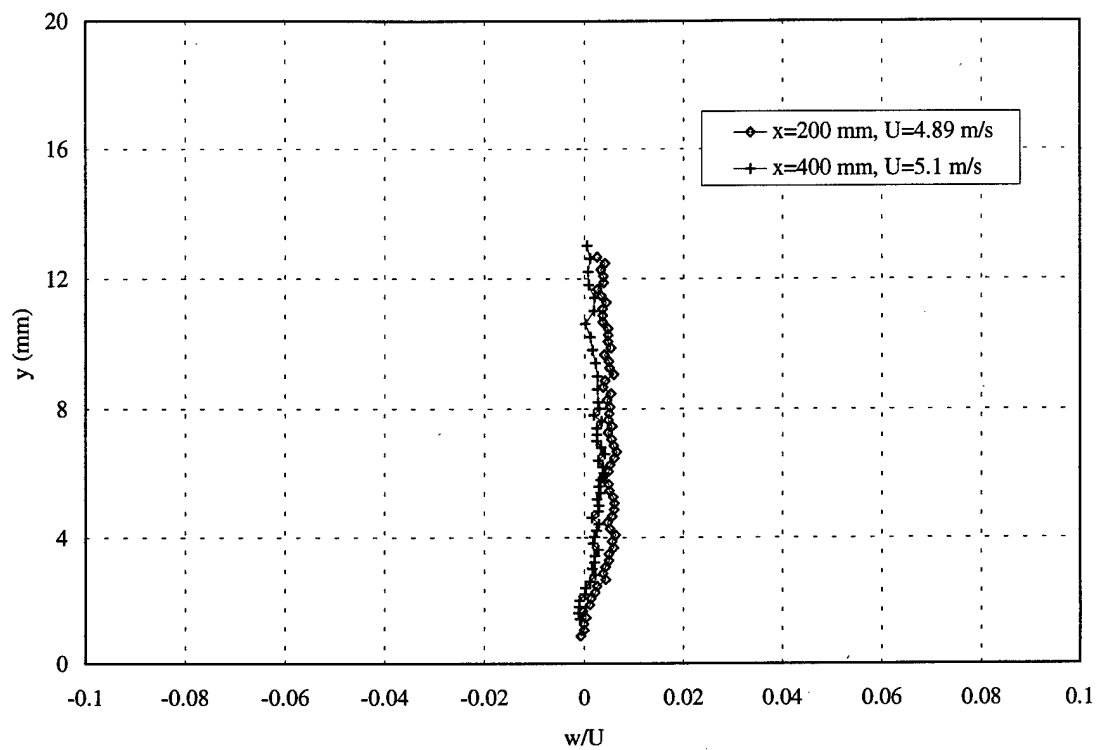
Figure 13. w profile, normal direction, smooth, ZPG
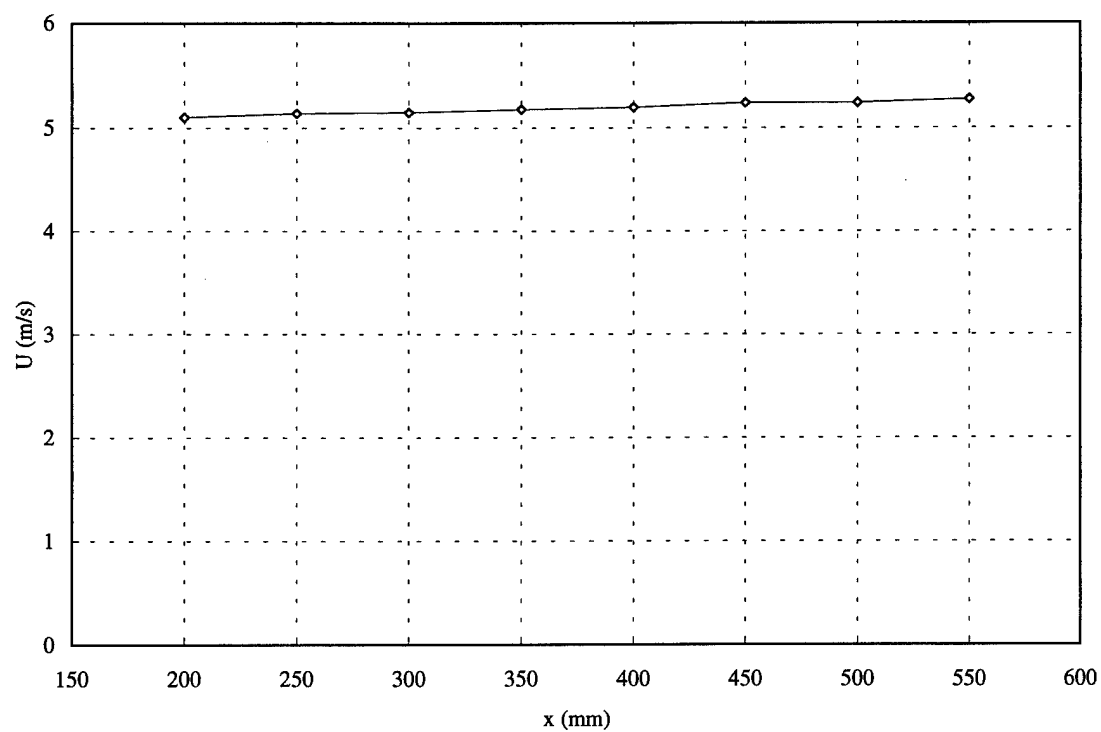
Figure 14. Freestream velocity, riblet, FPG, y = 30 mm
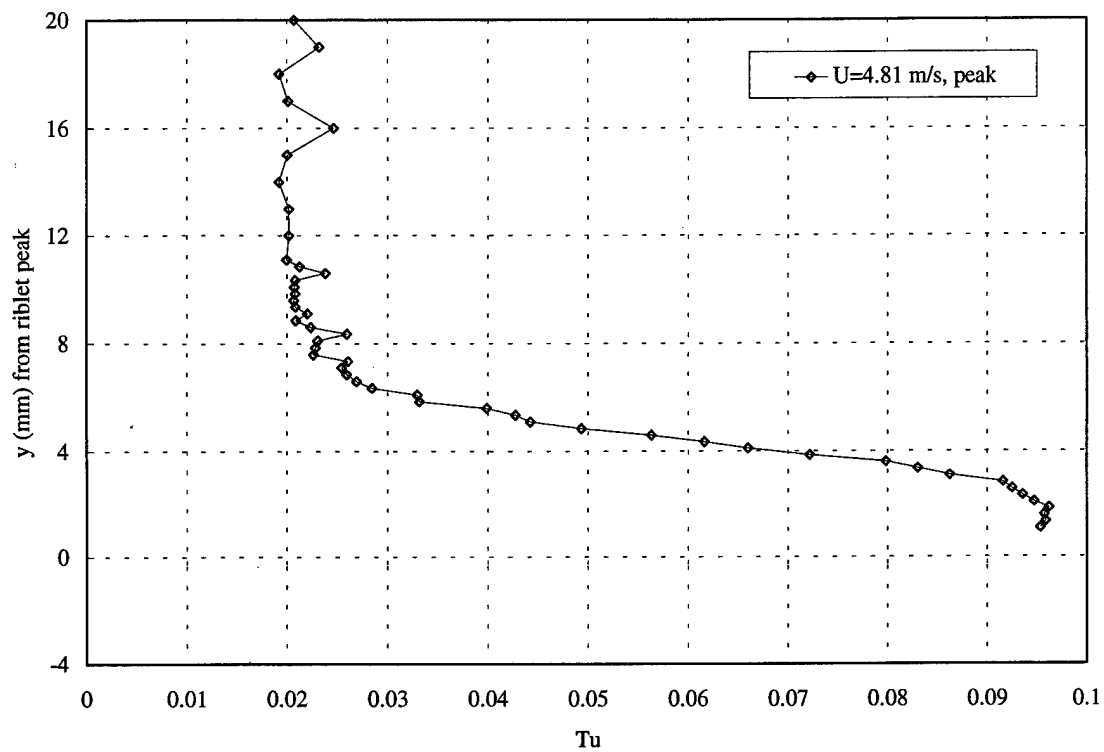
Figure 15. Turbulence intensity, riblet, FPG, 200 mm
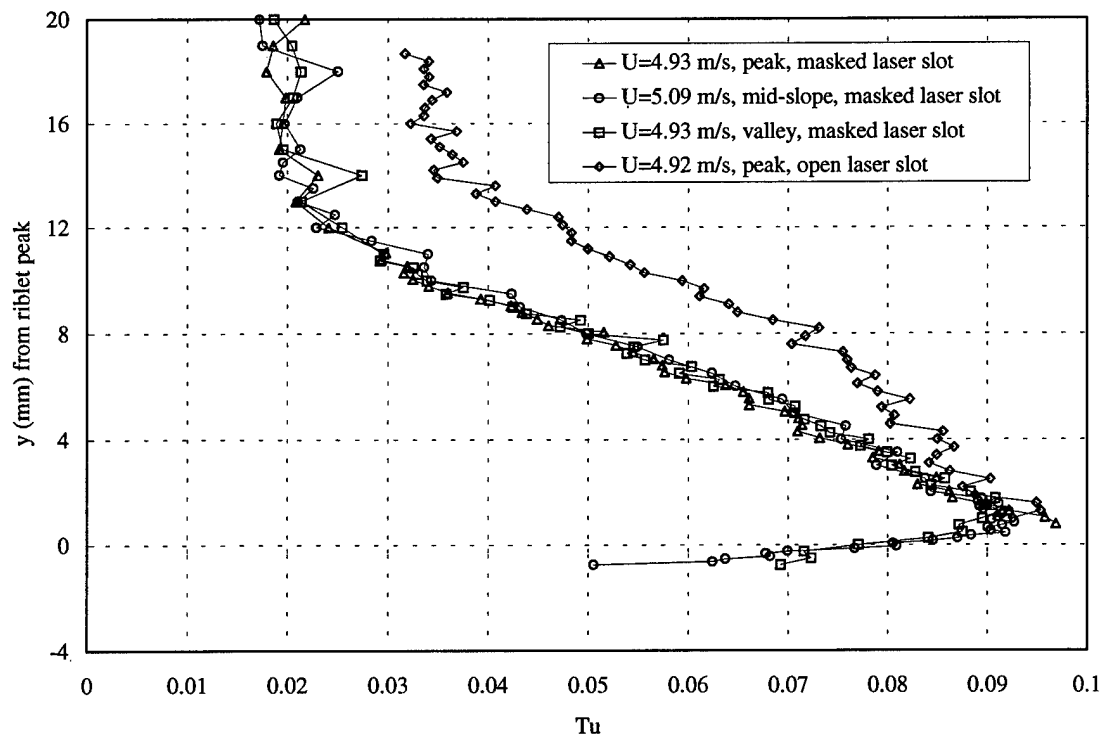
Figure 16. Turbulence intensity, riblet, FPG, 400 mm
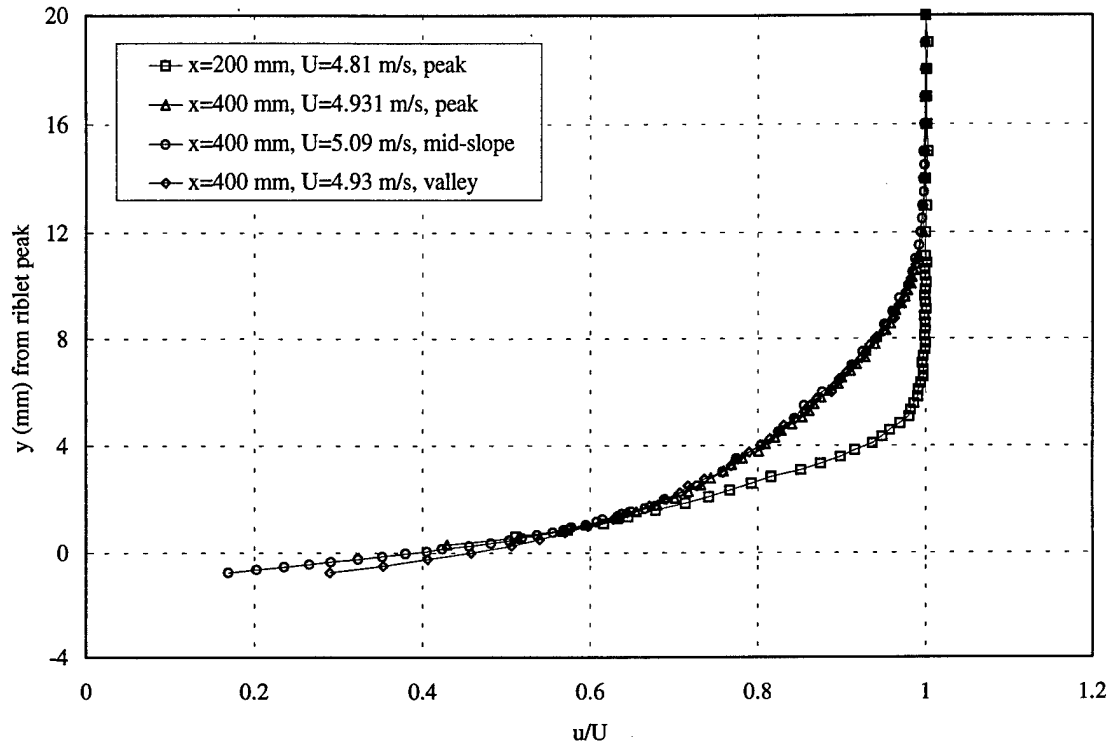
Figure 17. u profile, normal direction, riblet, FPG
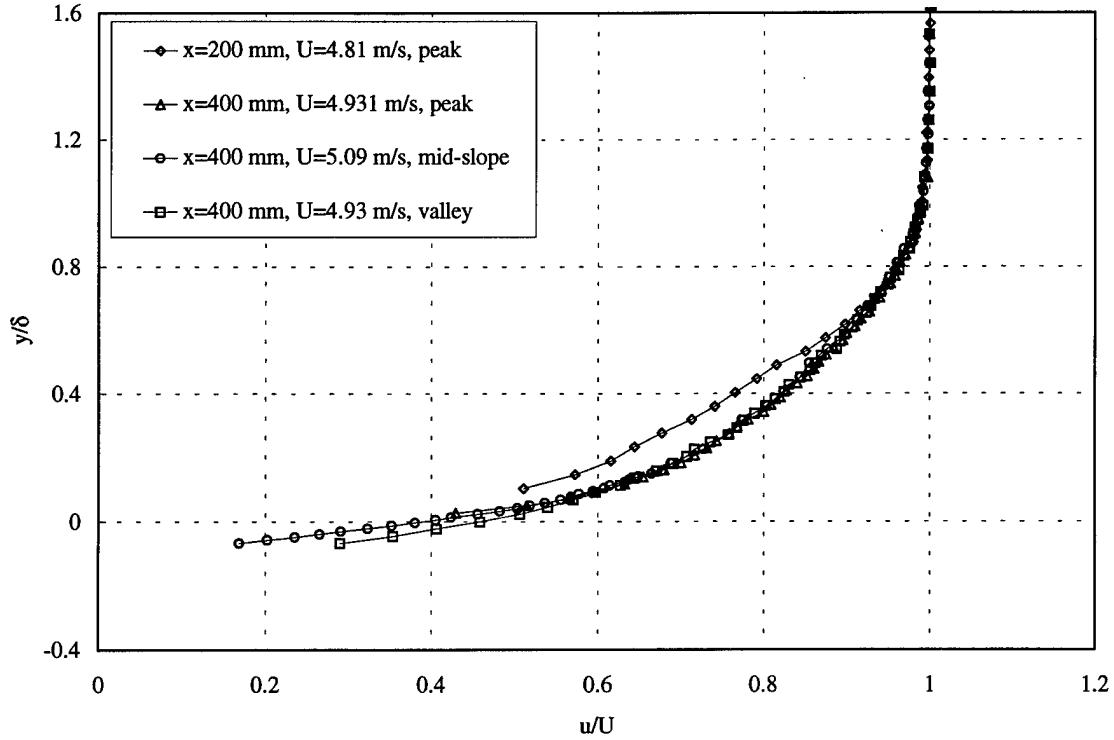
Figure 18. Velocity ratio profile, riblet, FPG
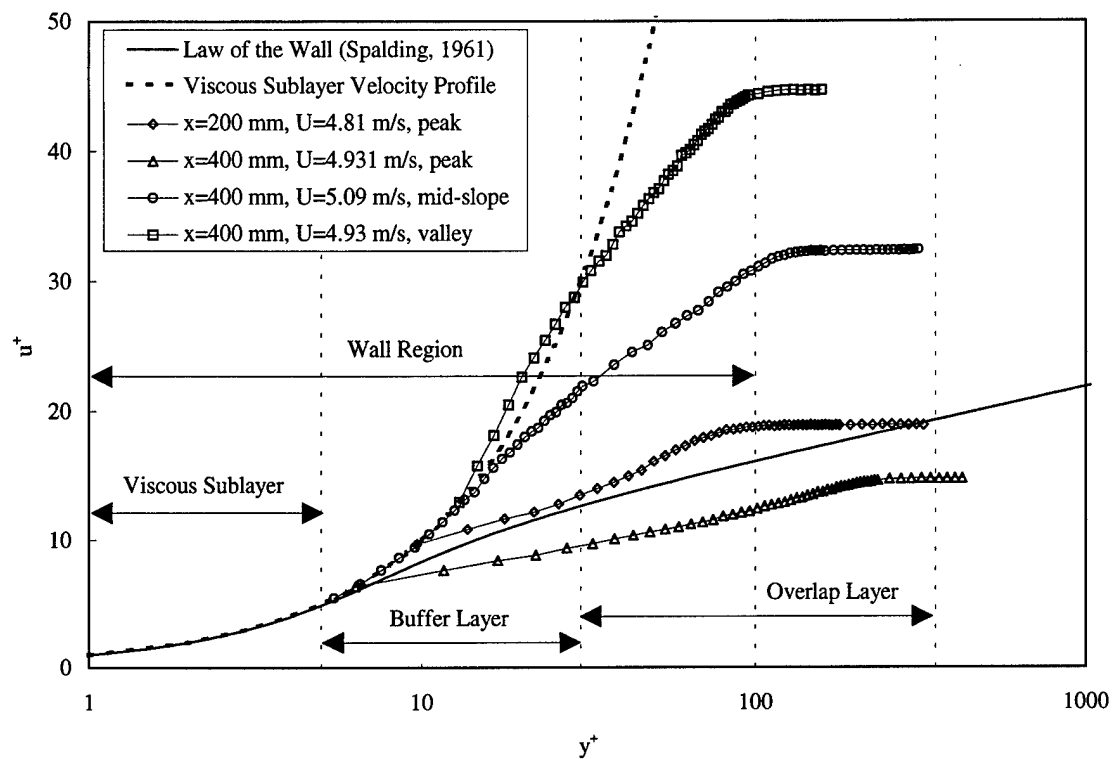
Figure 19. u^+ profile, riblet, FPG
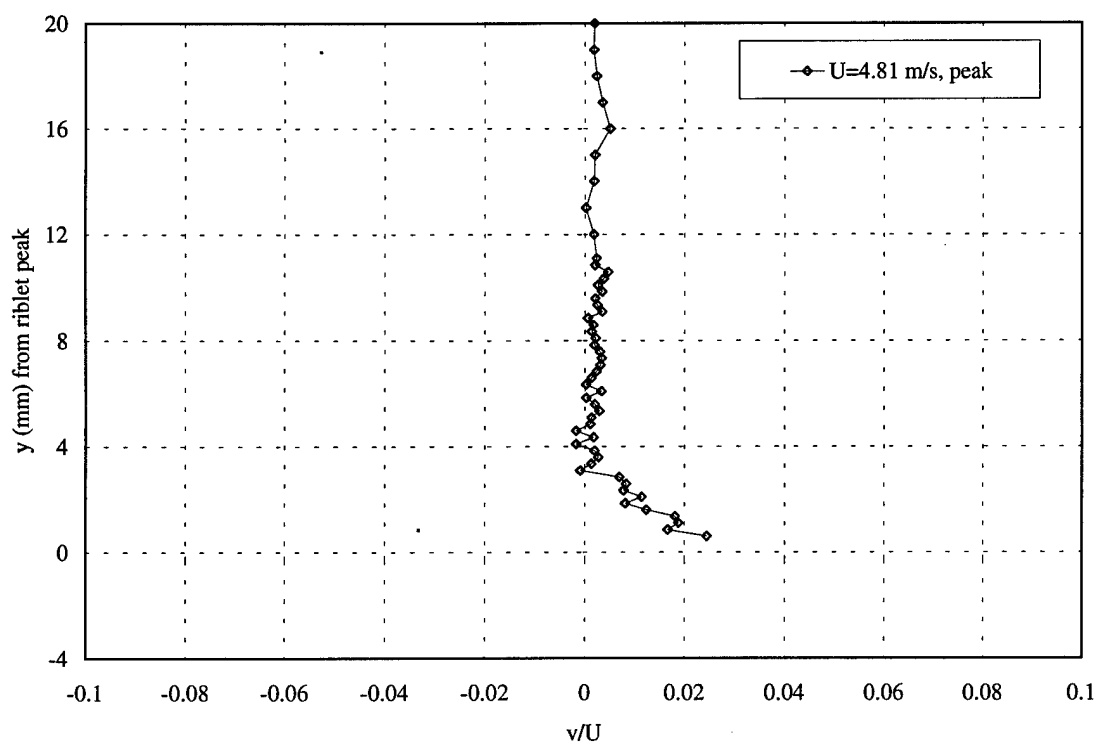
Figure 20. v profile, normal direction, riblet, FPG, 200 mm, peak
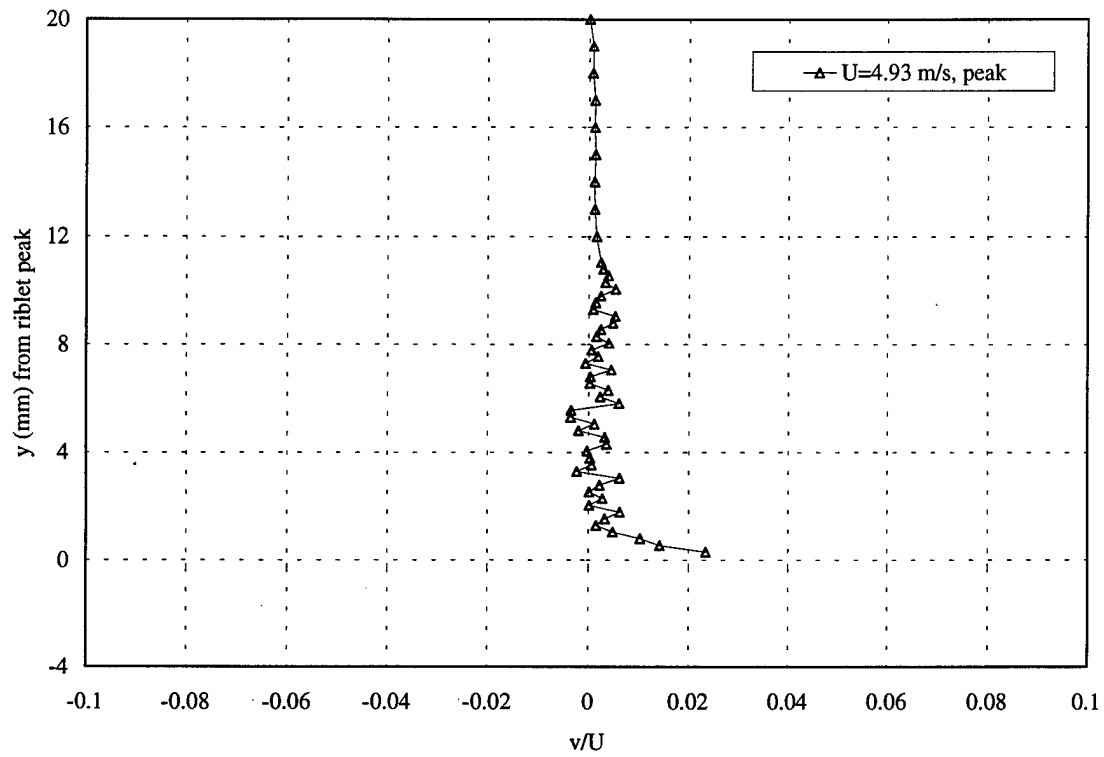
Figure 21. v profile, normal direction, riblet, FPG, 400 mm, peak
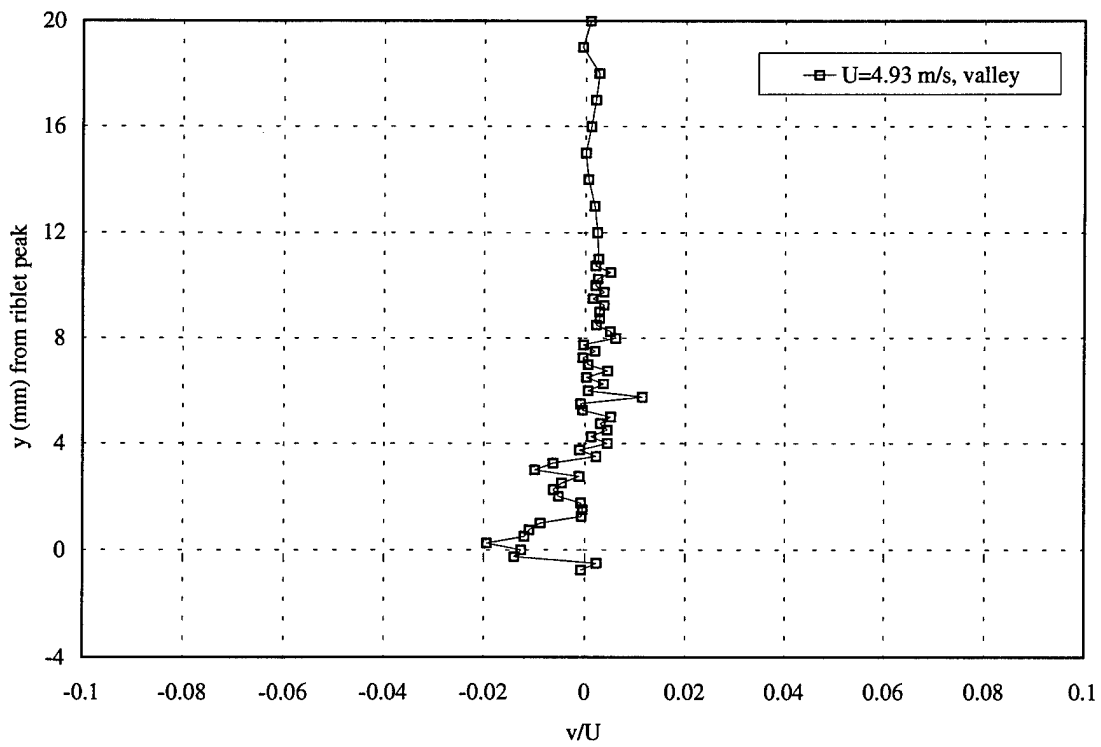
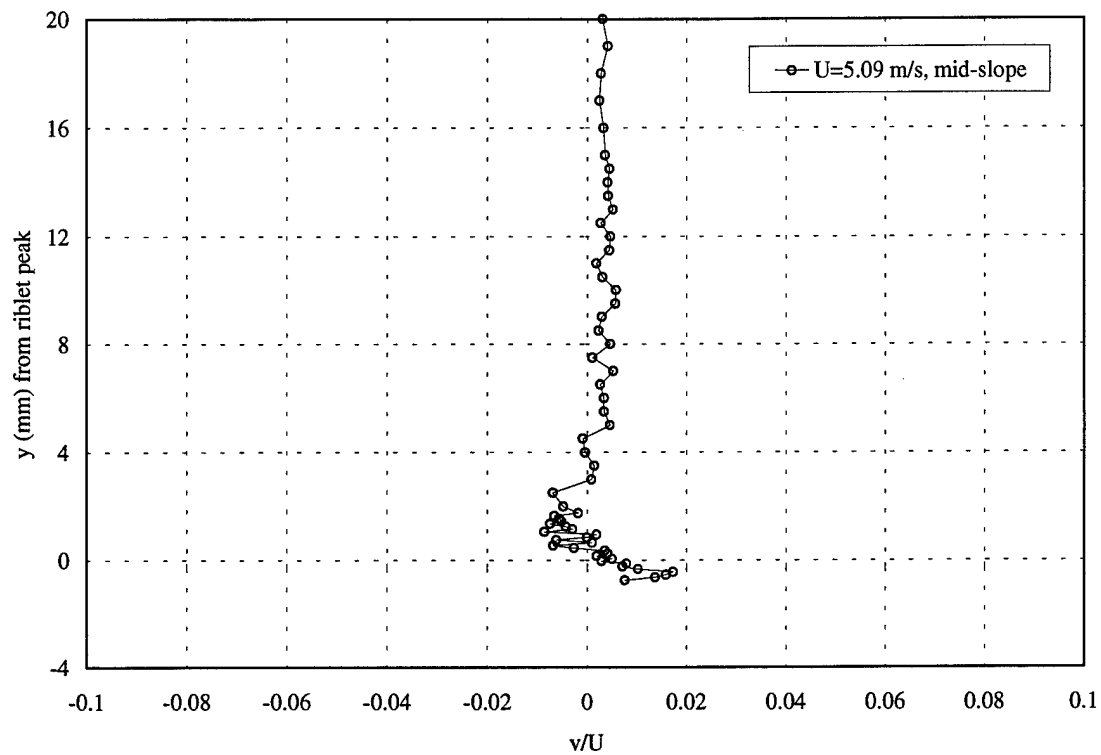Figure 22. v profile, normal direction, riblet, FPG, 400 mm, valley

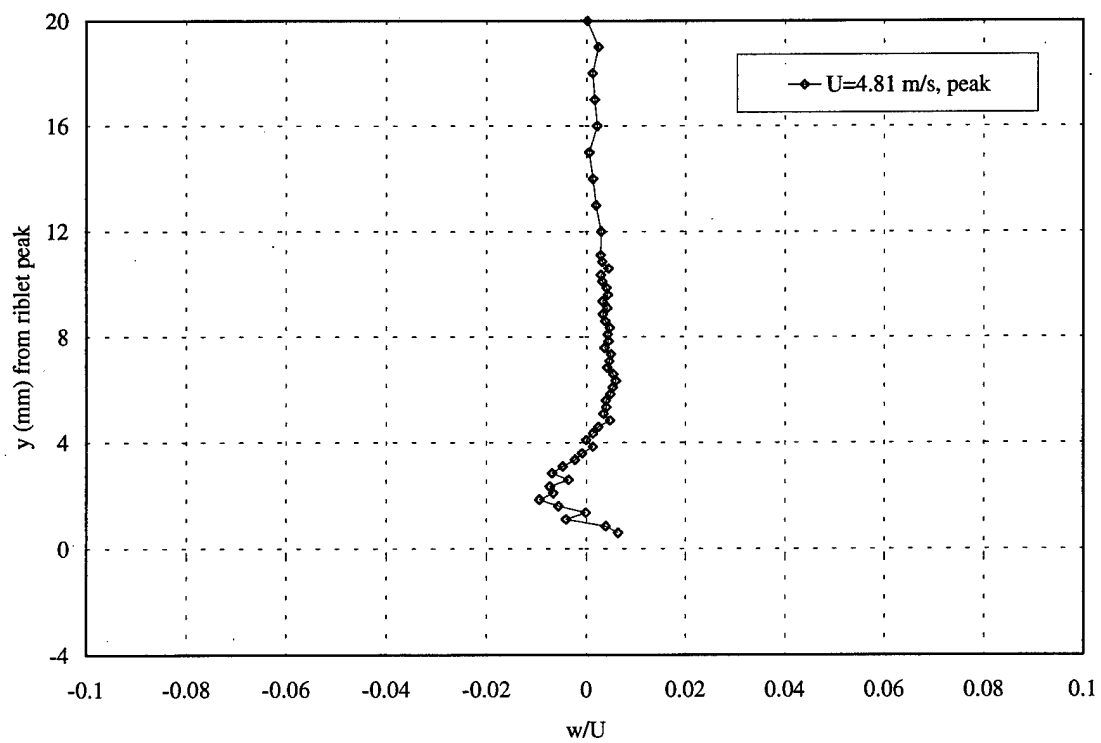Figure 23. v profile, normal direction, riblet, FPG, 400 mm, mid-slope

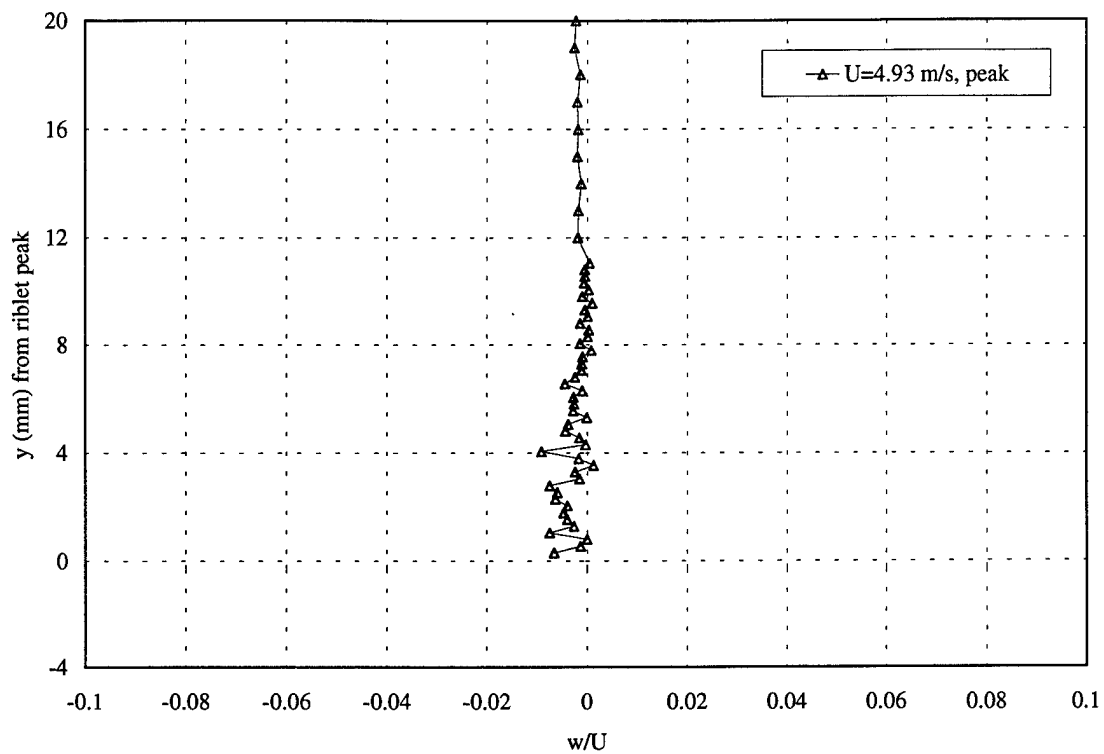Figure 24. w profile, normal direction, riblet, FPG, 200 mm, peak

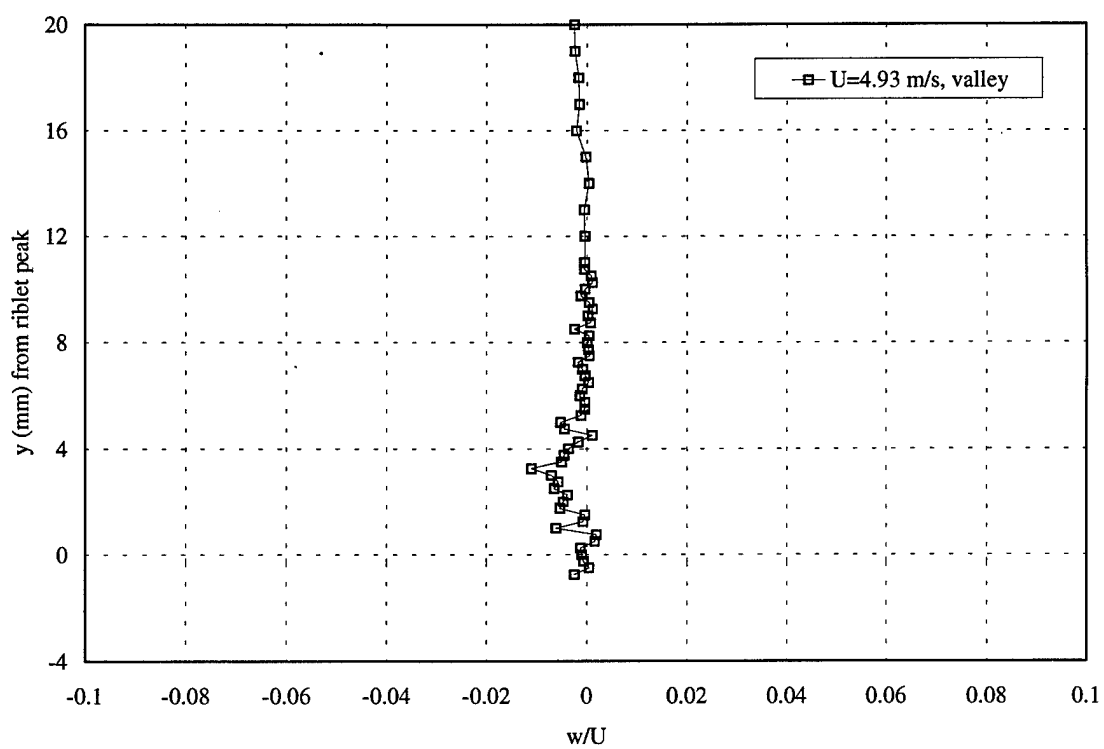Figure 25. w profile, normal direction, riblet, FPG, 400 mm, peak

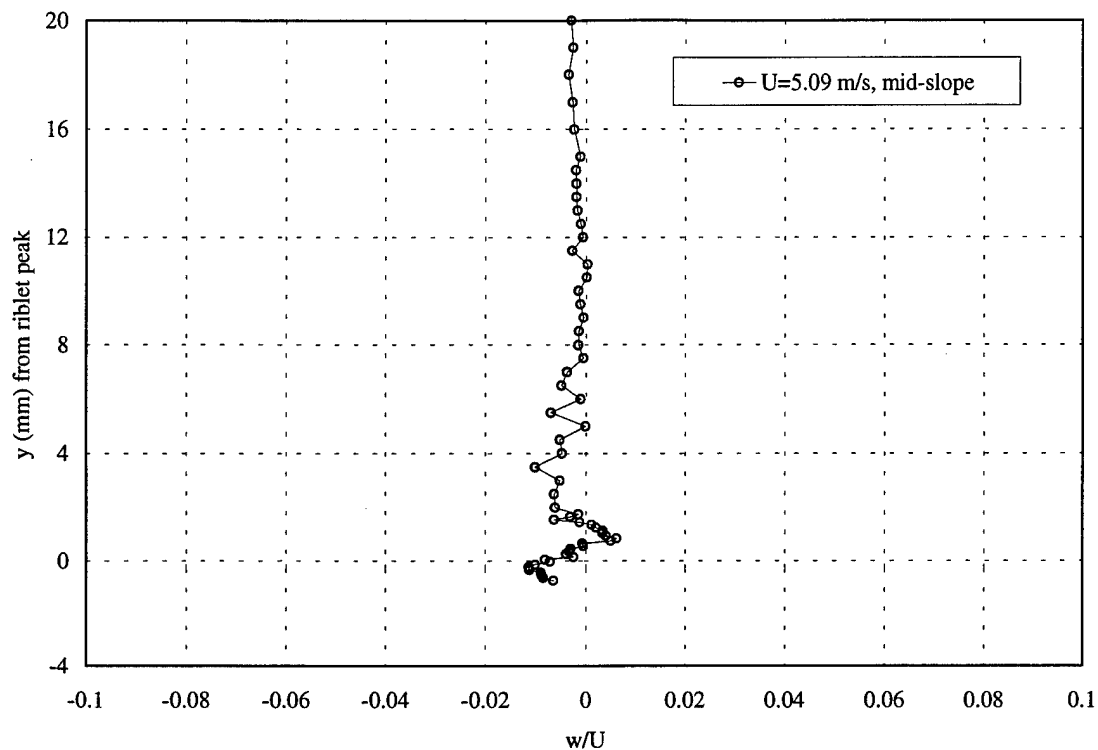Figure 26. w profile, normal direction, riblet, FPG, 400 mm, valley

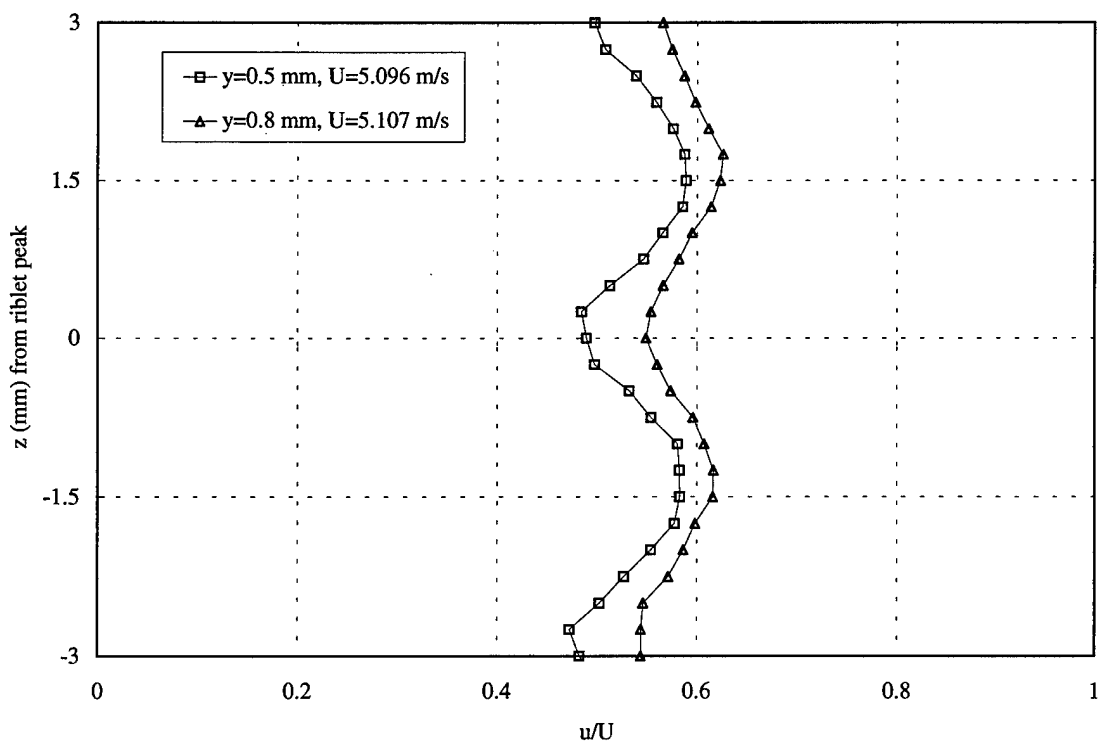Figure 27. w profile, normal direction, riblet, FPG, 400 mm, mid-slope

Figure 28. u profile, spanwise direction, riblet, FPG, 200 mm
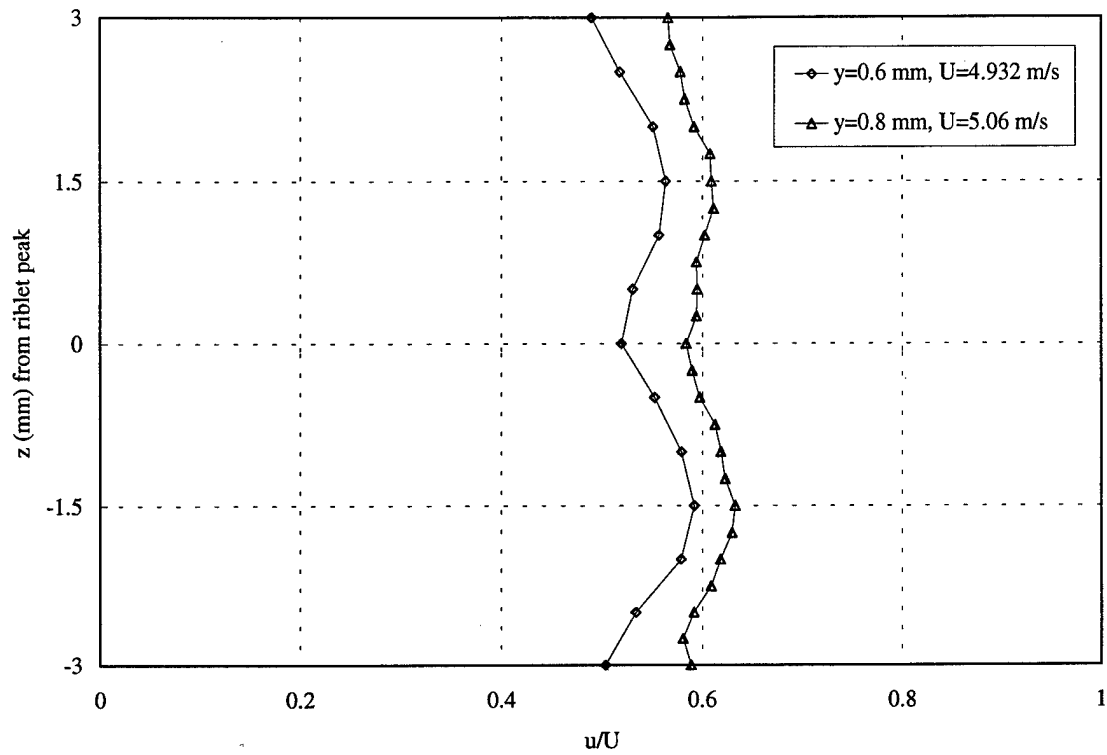
Figure 29. u profile, spanwise direction, riblet, FPG, 400 mm

Figure 30. v profile, spanwise direction, riblet, FPG, 200 mm
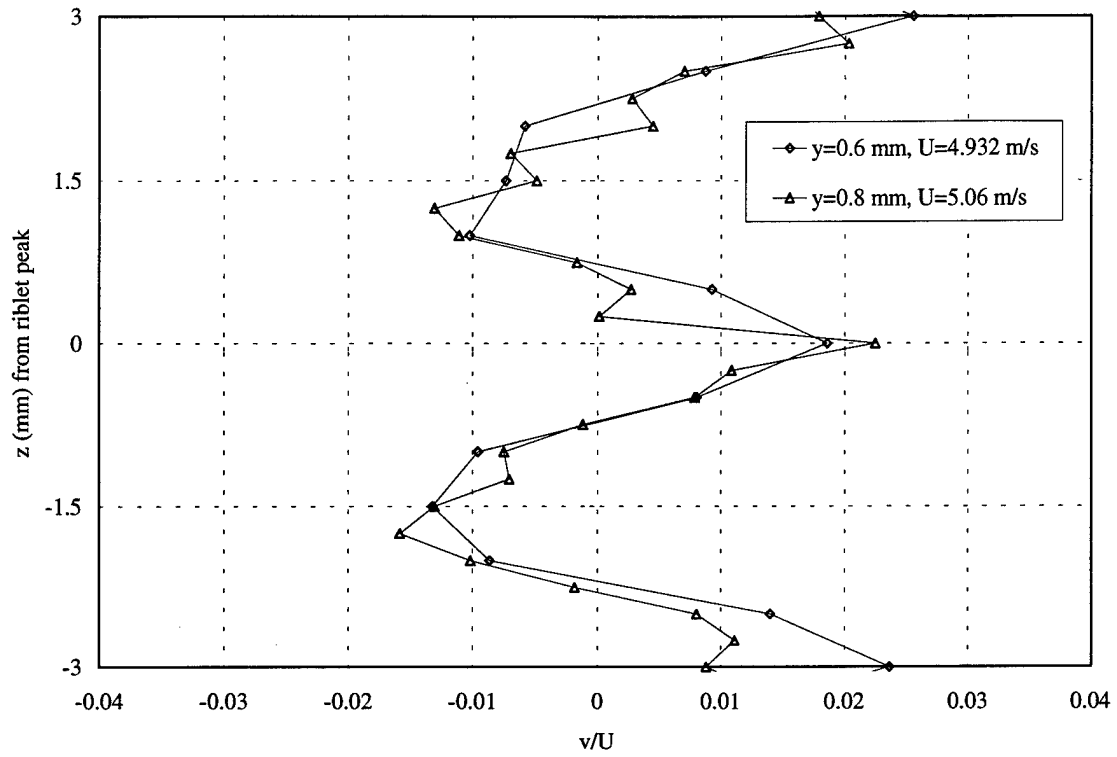
Figure 31. v profile, spanwise direction, riblet, FPG, 400 mm

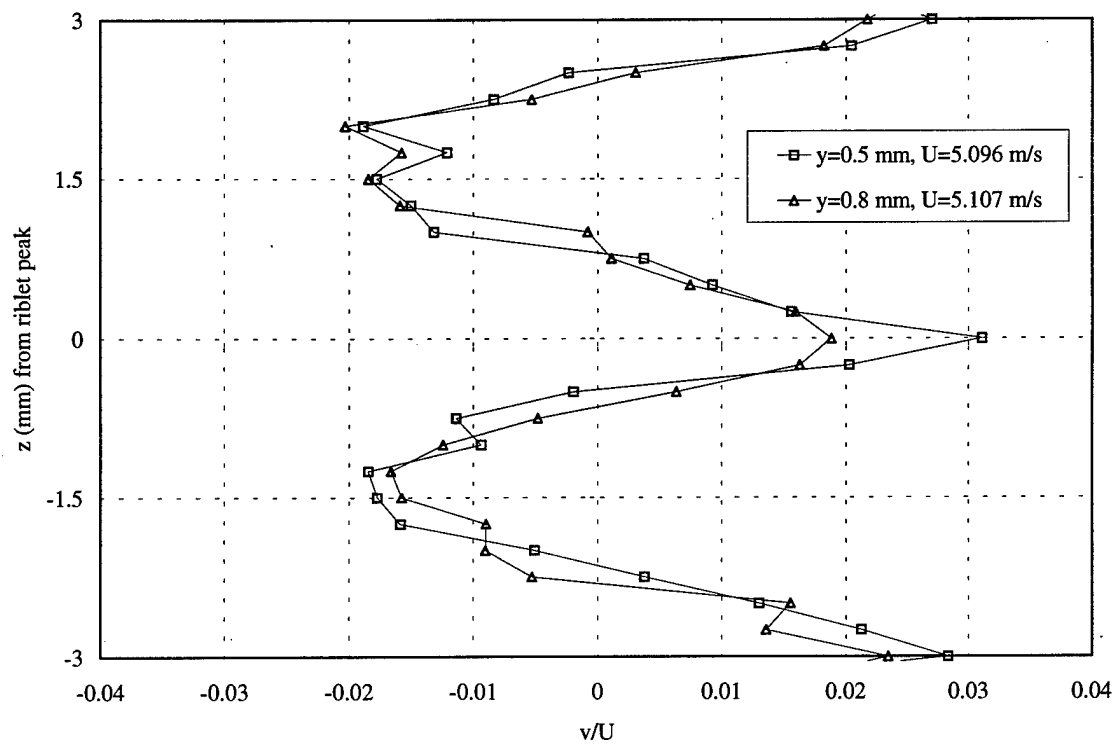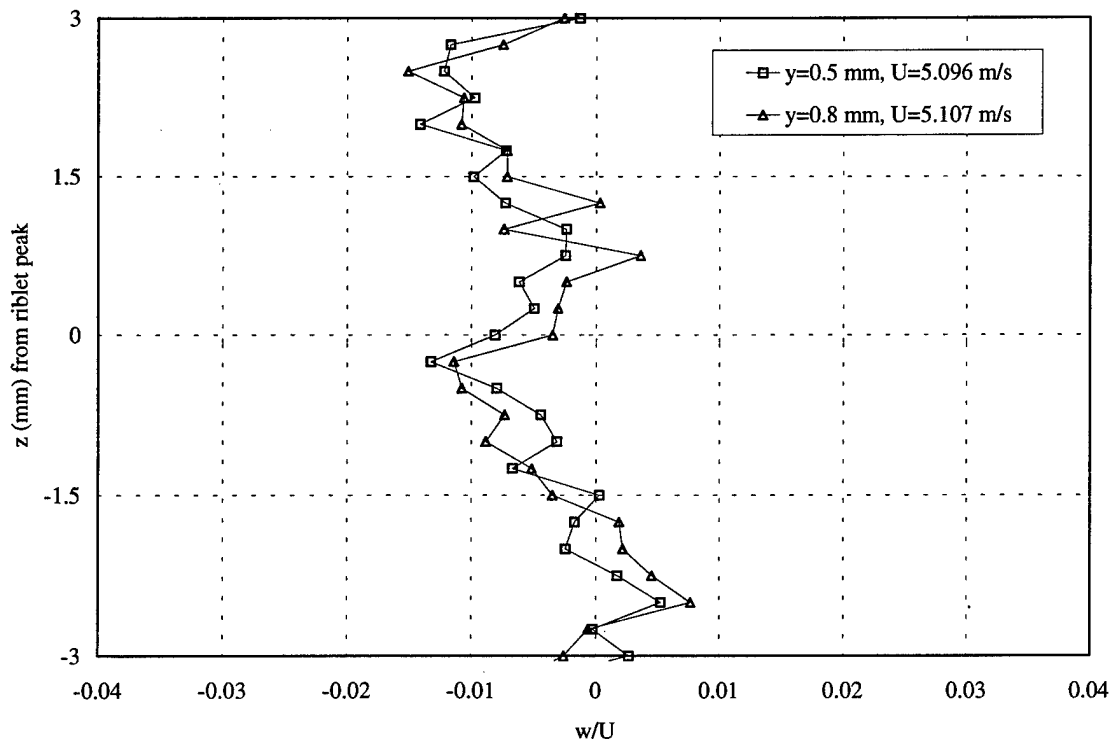Figure 32. w profile, spanwise direction, riblet, FPG, 200 mm

109

Figure 33. w profile, spanwise direction, riblet, FPG, 400 mm
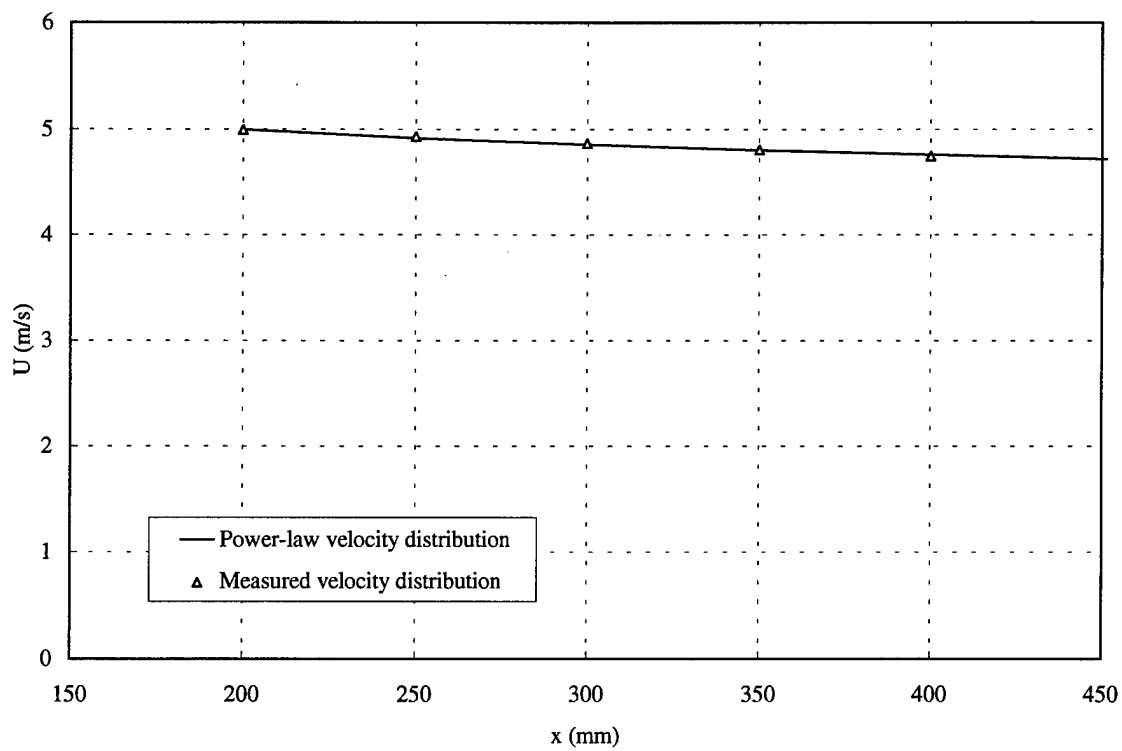
Figure 34. Freestream velocity, riblet, APG, y = 30 mm
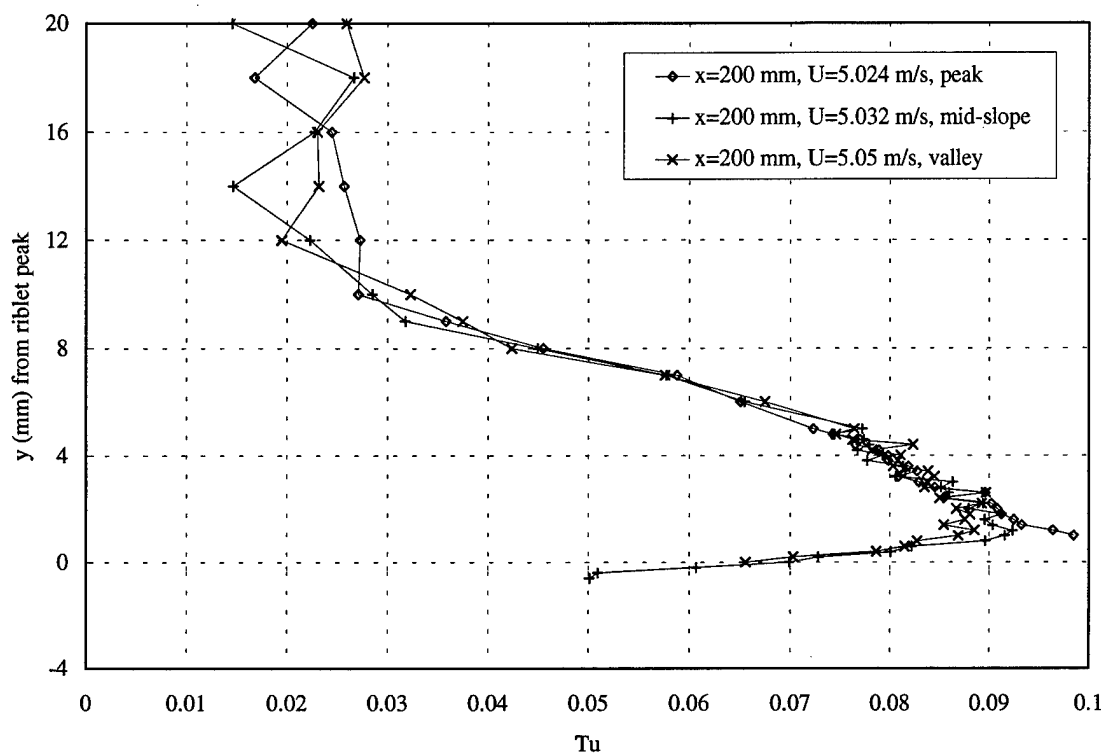
Figure 35. Turbulence intensity, riblet, APG, 200 mm
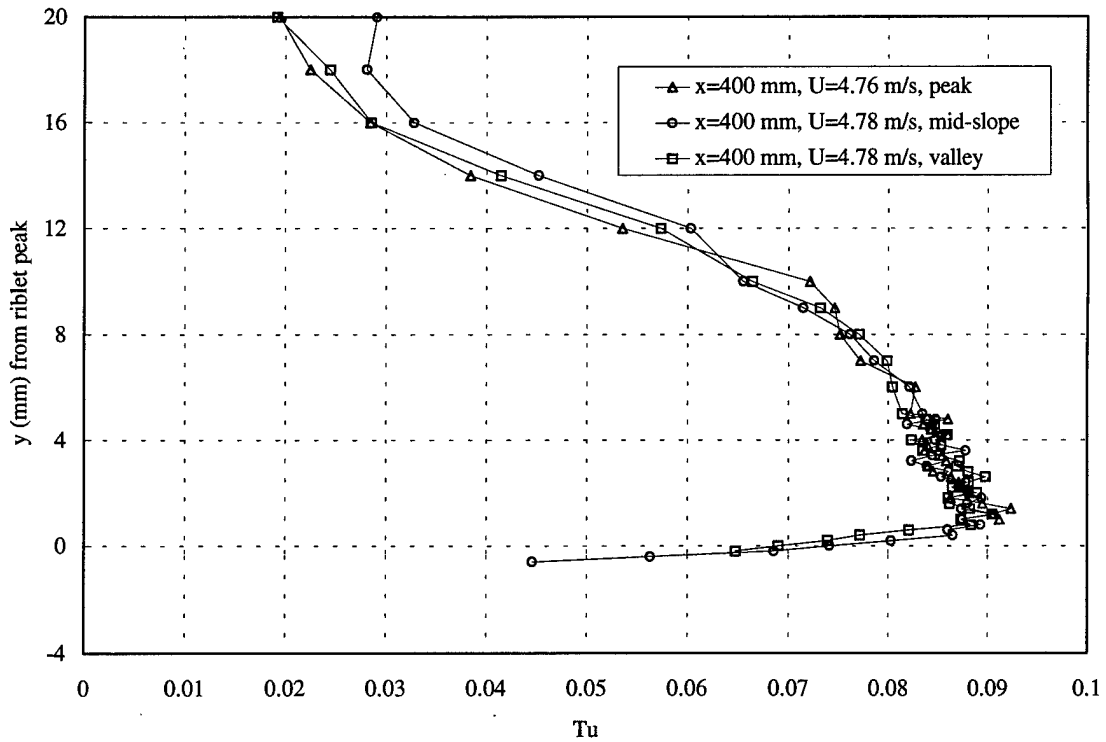
Figure 36. Turbulence intensity, riblet, APG, 400 mm
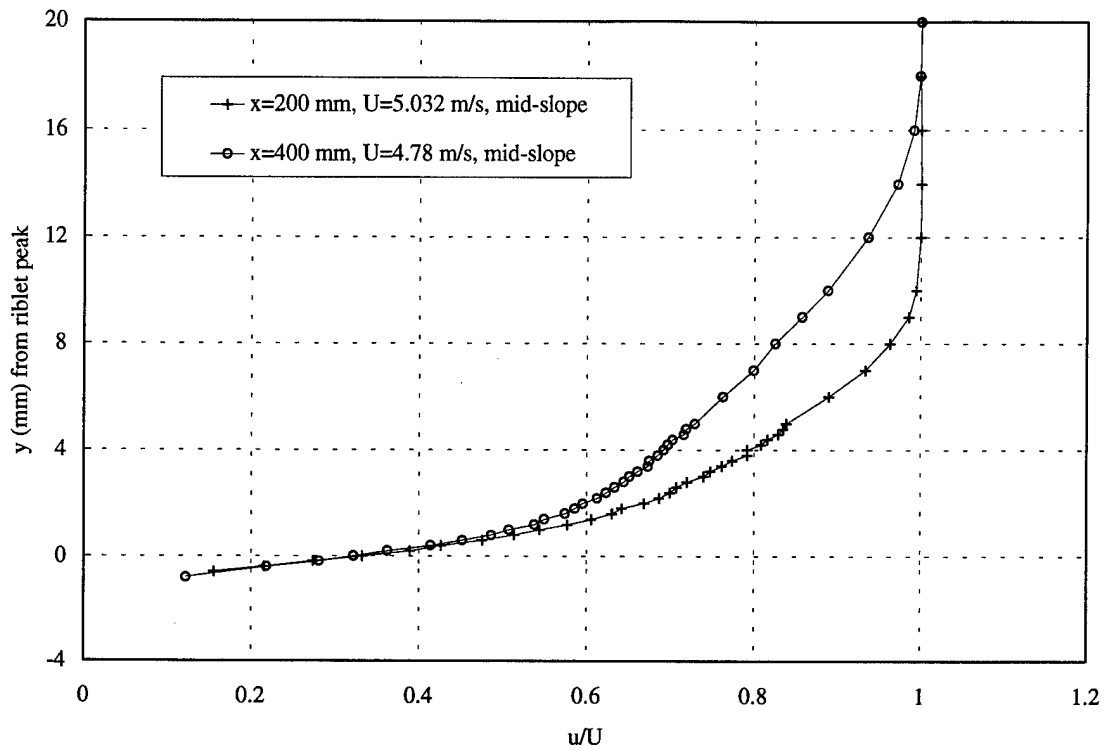
Figure 37. u profile, normal direction, riblet, APG
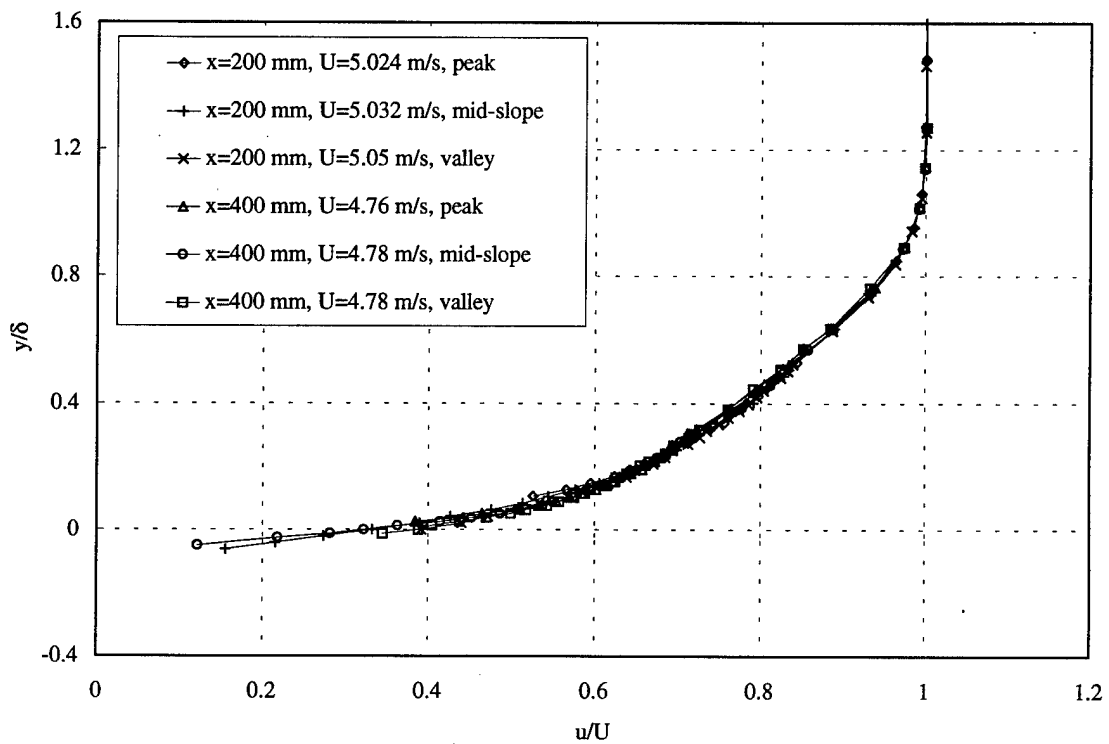
Figure 38. Velocity ratio profile, riblet, APG

112
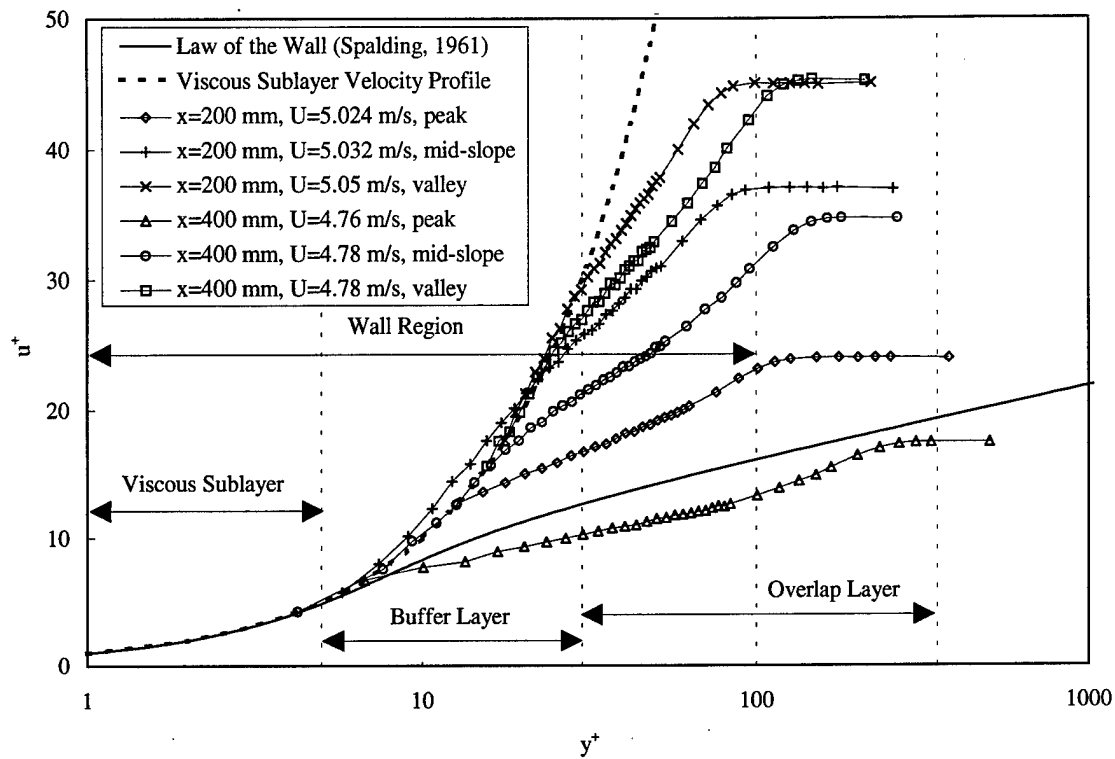
Figure 39. u+ profile, riblet, APG
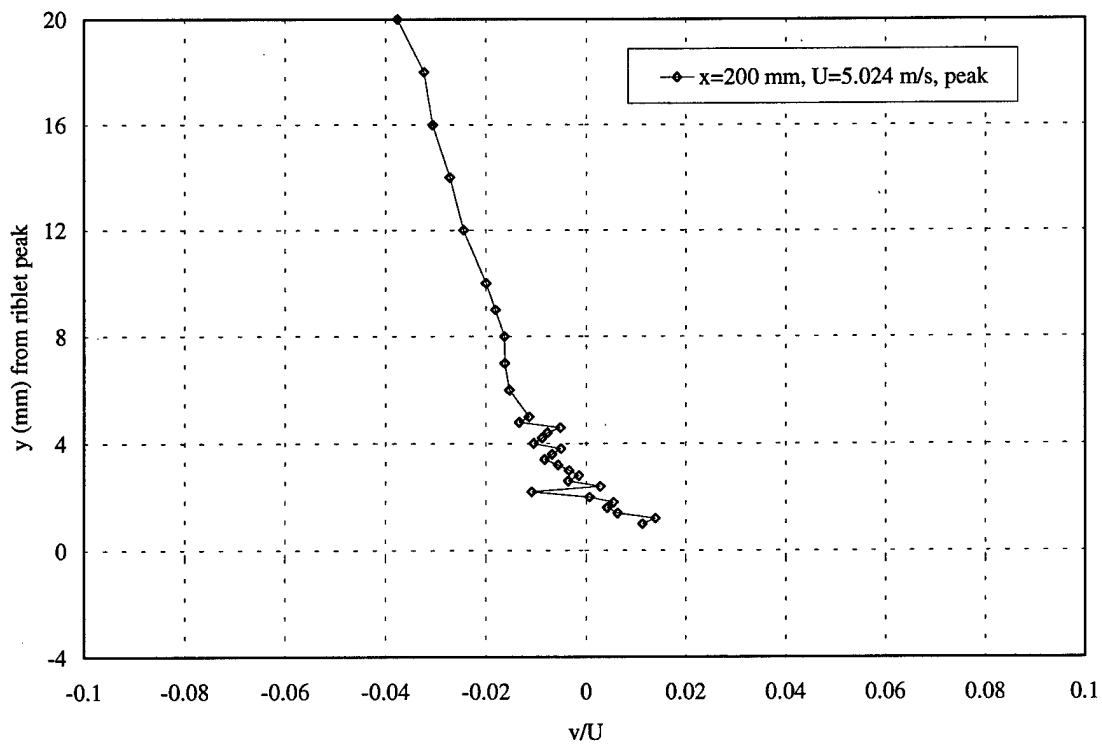
Figure 40. v profile, normal direction, riblet, APG, 200 mm, peak
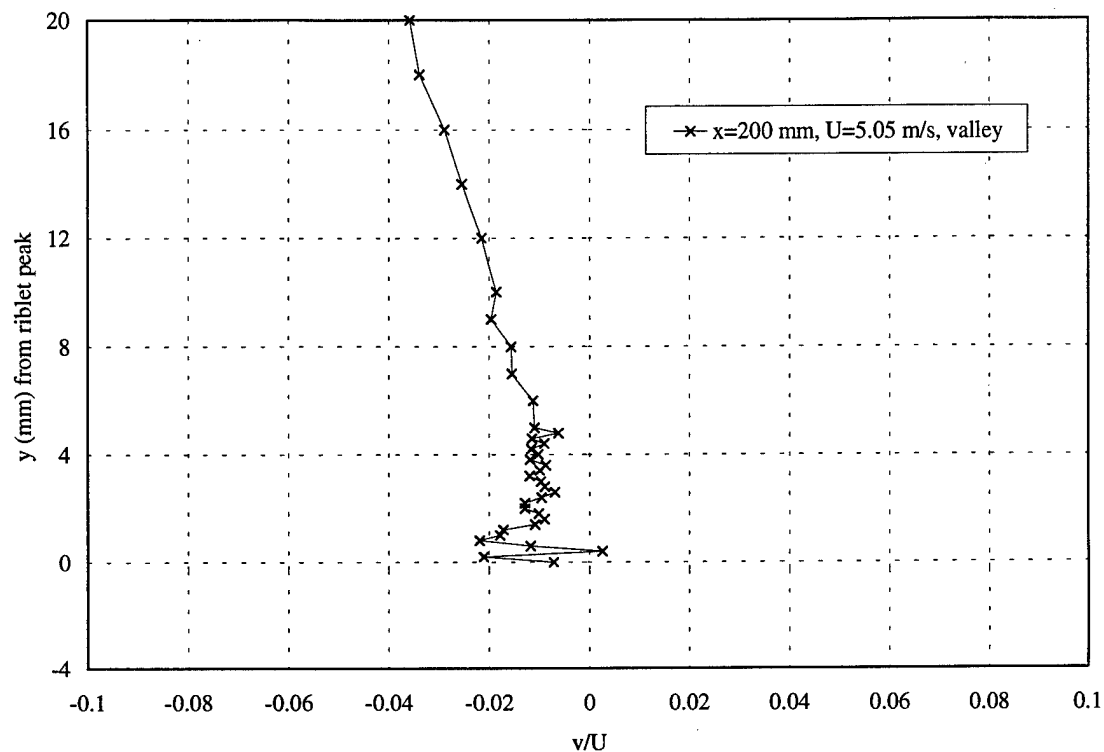
Figure 41. v profile, normal direction, riblet, APG, 200 mm, valley
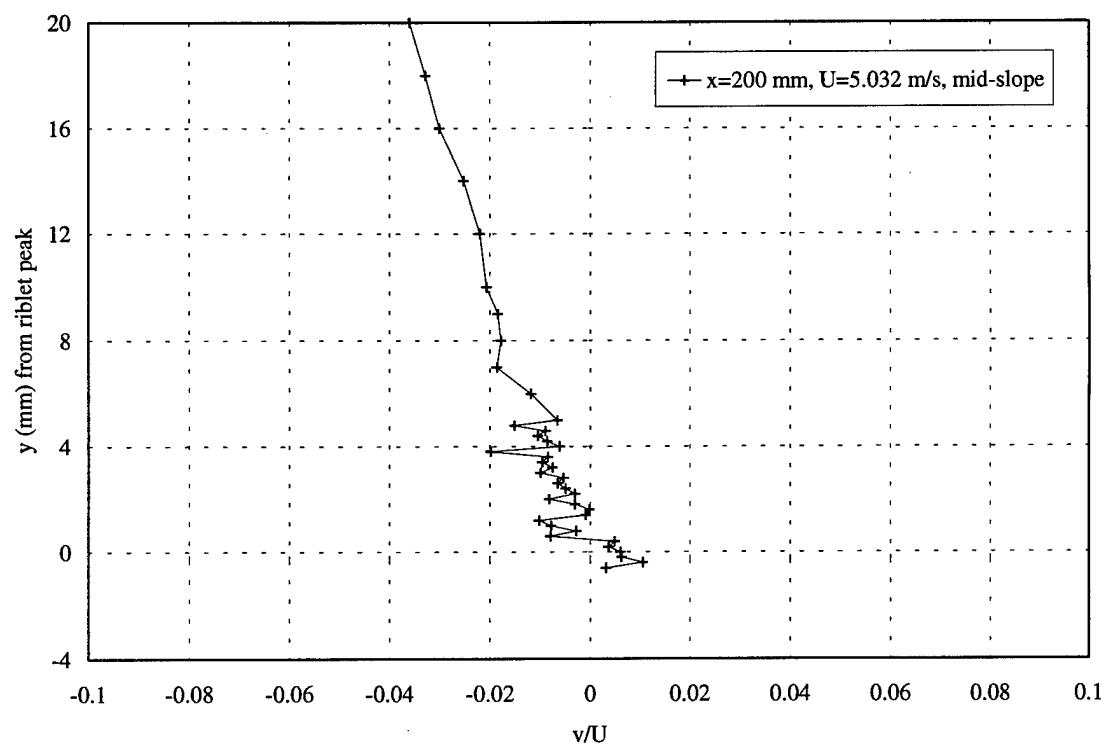
Figure 42. v profile, normal direction, riblet, APG, 200 mm, mid-slope

114
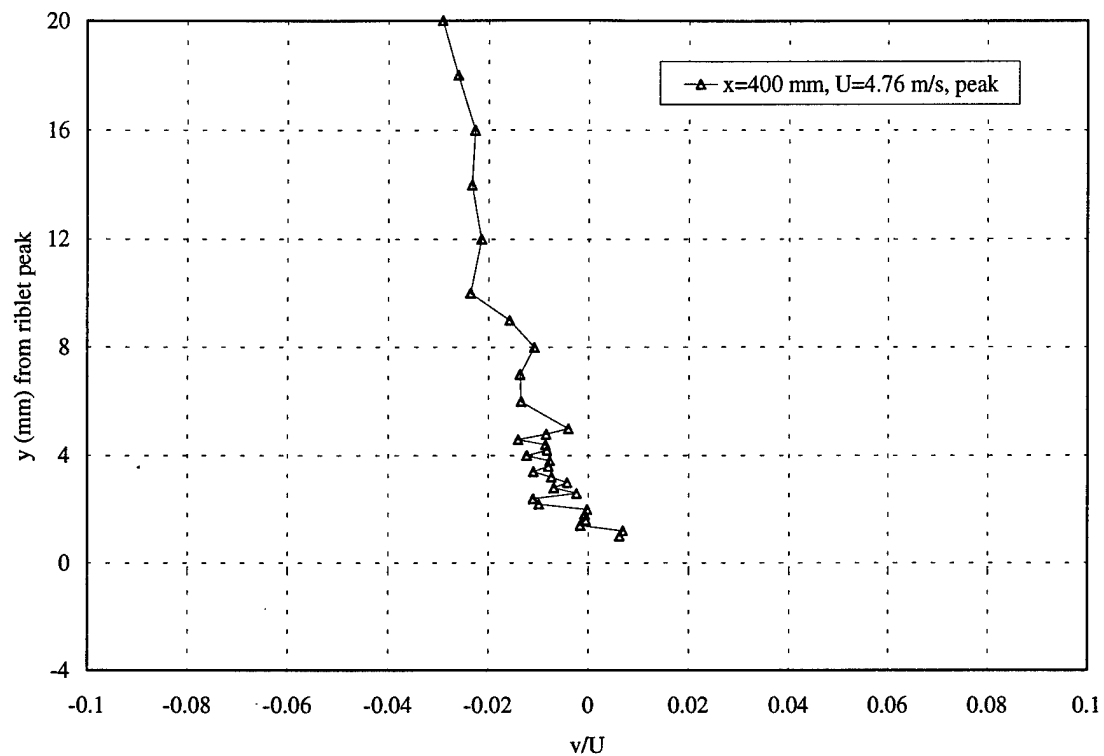
Figure 43. v profile, normal direction, riblet, APG, 400 mm, peak
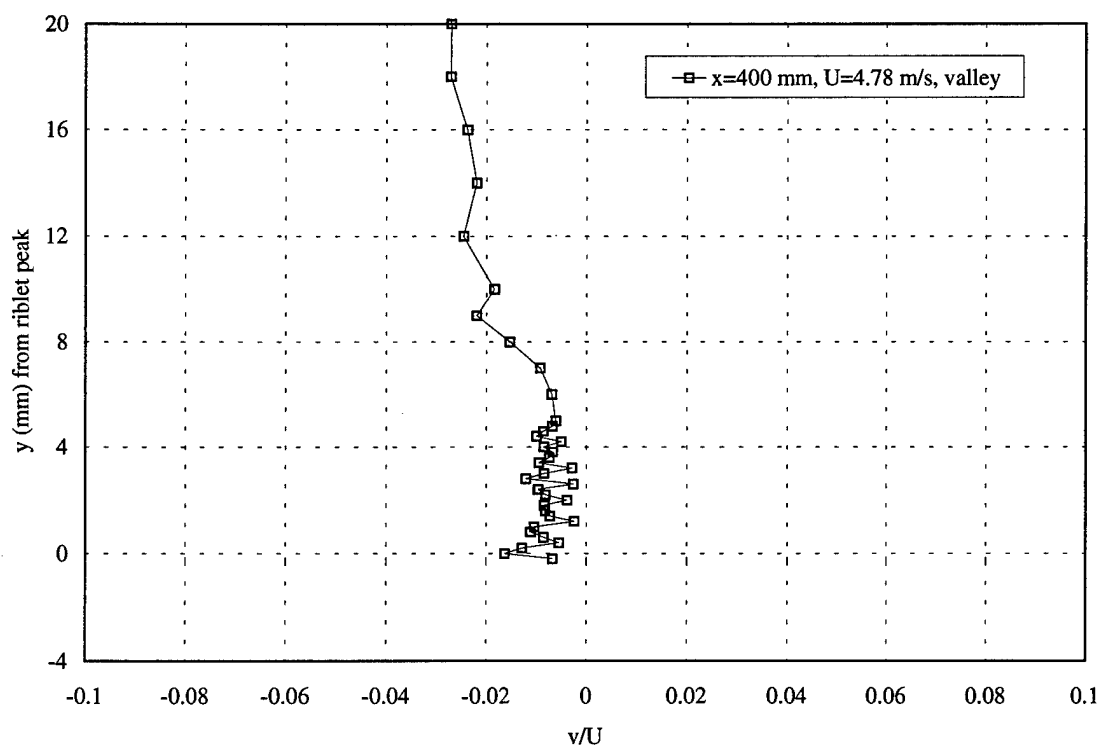
Figure 44. v profile, normal direction, riblet, APG, 400 mm, valley

115
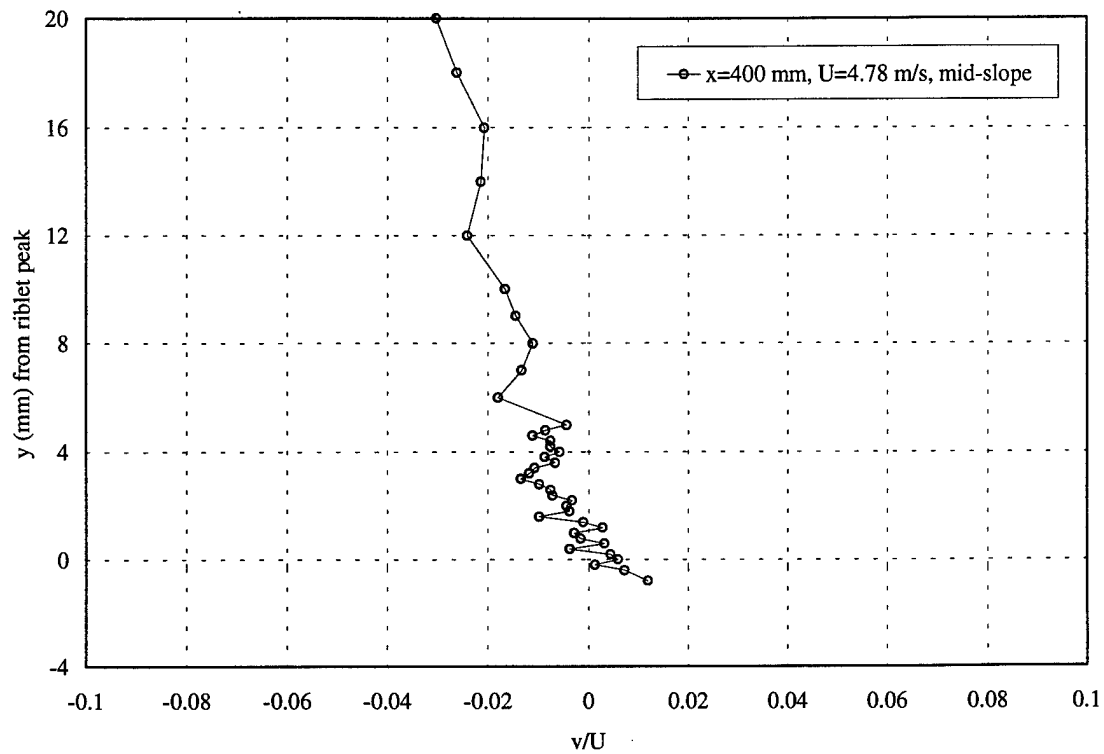
Figure 45. v profile, normal direction, riblet, APG, 400 mm, mid-slope
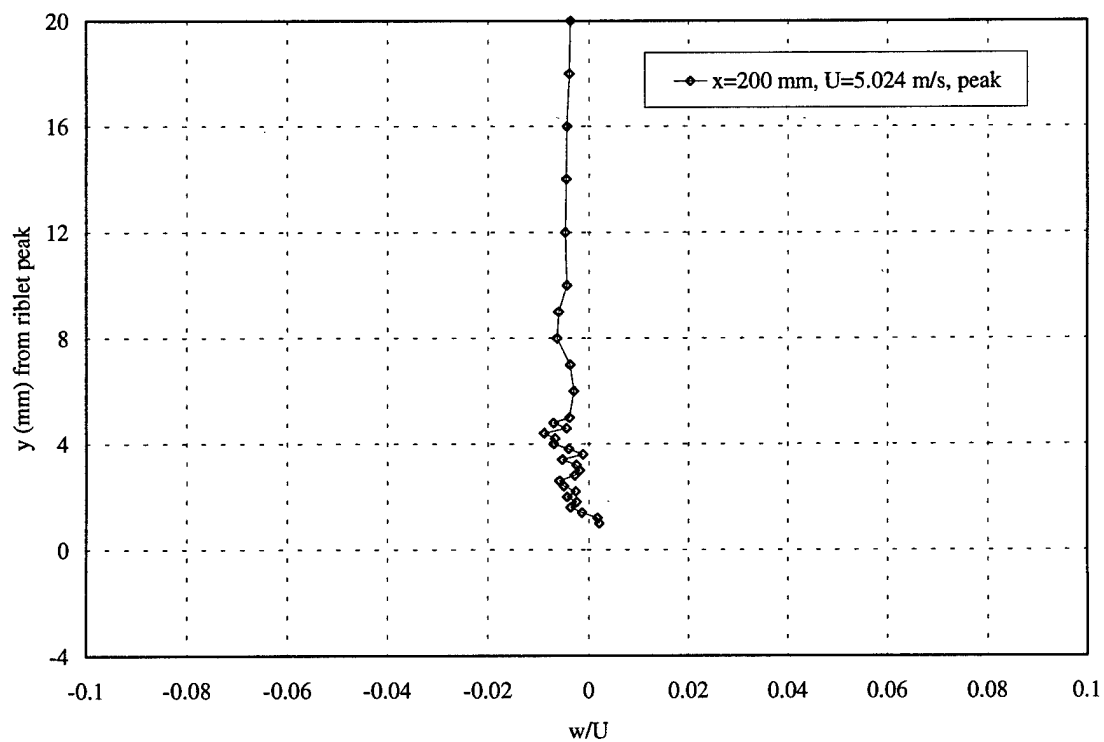
Figure 46. w profile, normal direction, riblet, APG, 200 mm, peak
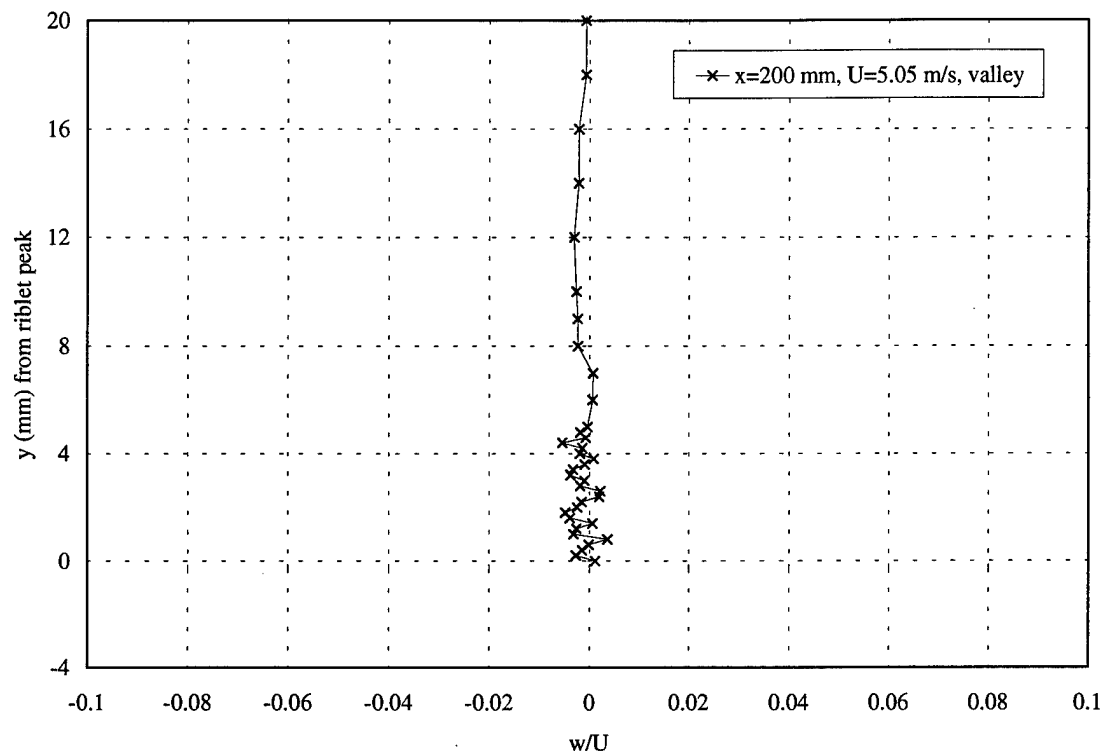
Figure 47. w profile, normal direction, riblet, APG, 200 mm, valley
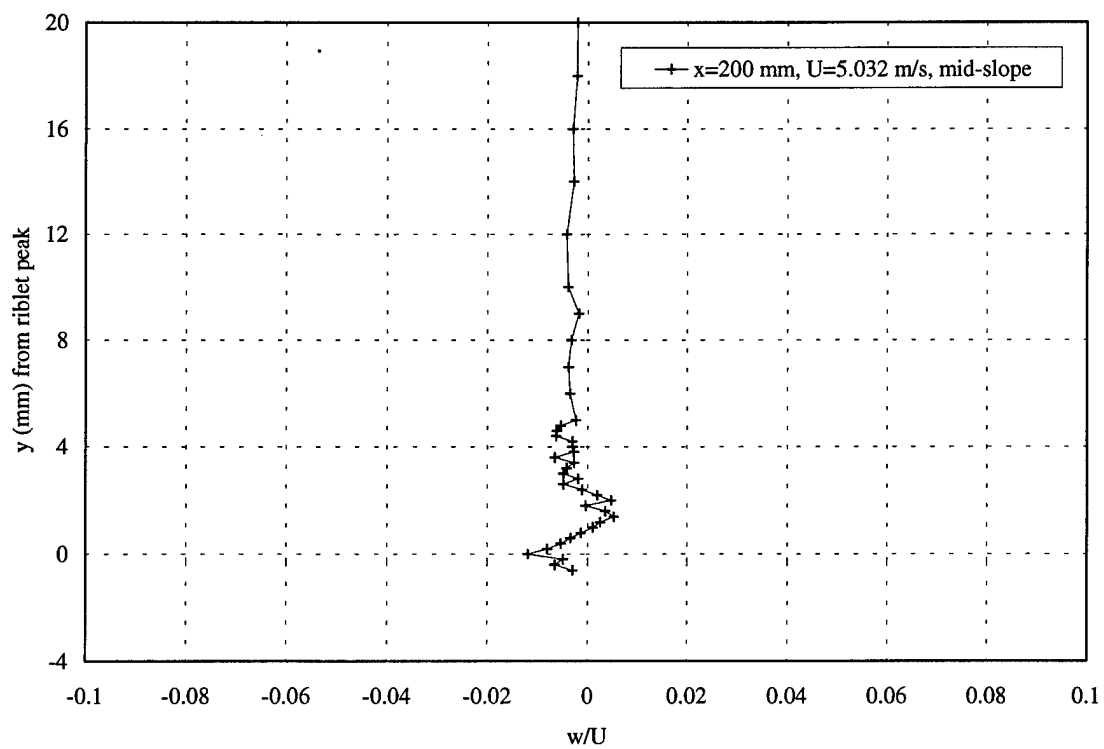
Figure 48. w profile, normal direction, riblet, APG, 200 mm, mid-slope

117
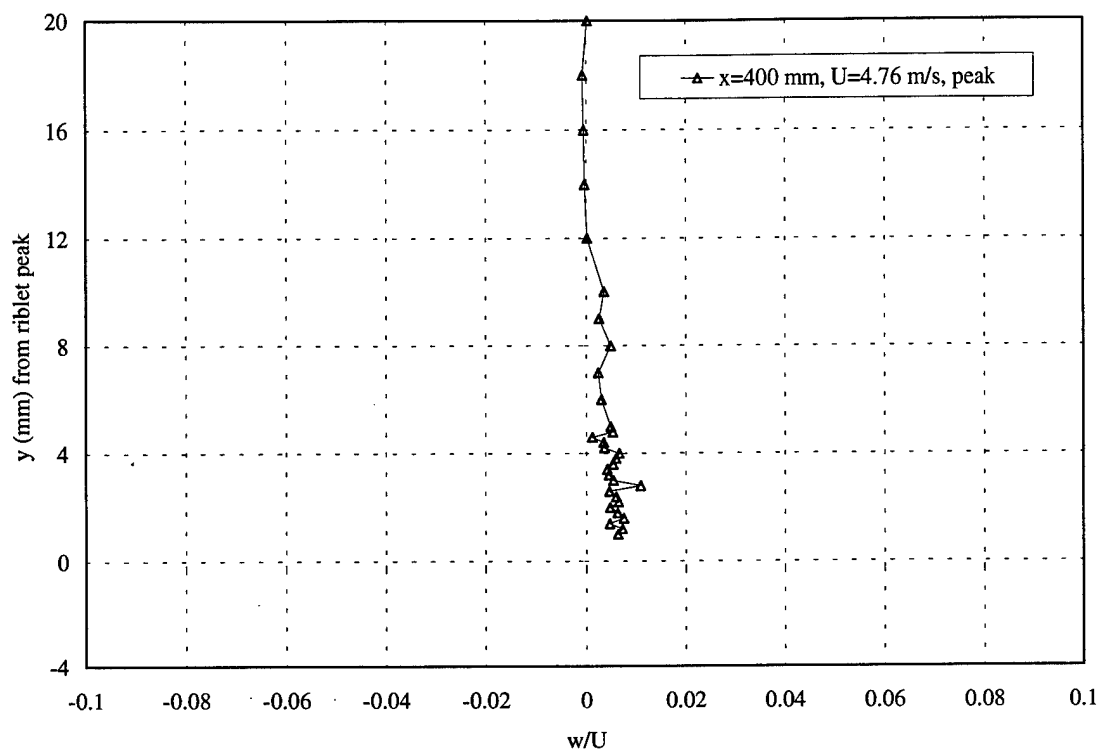
Figure 49. w profile, normal direction, riblet, APG, 400 mm, peak
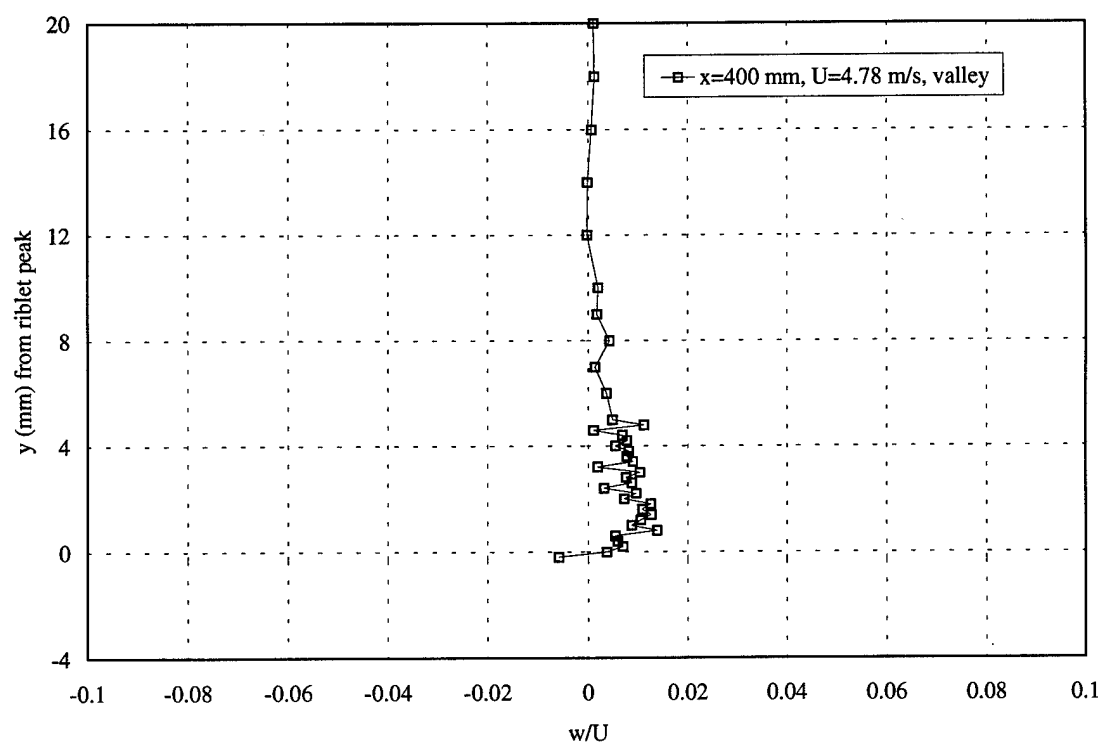
Figure 50. w profile, normal direction, riblet, APG, 400 mm, valley

118
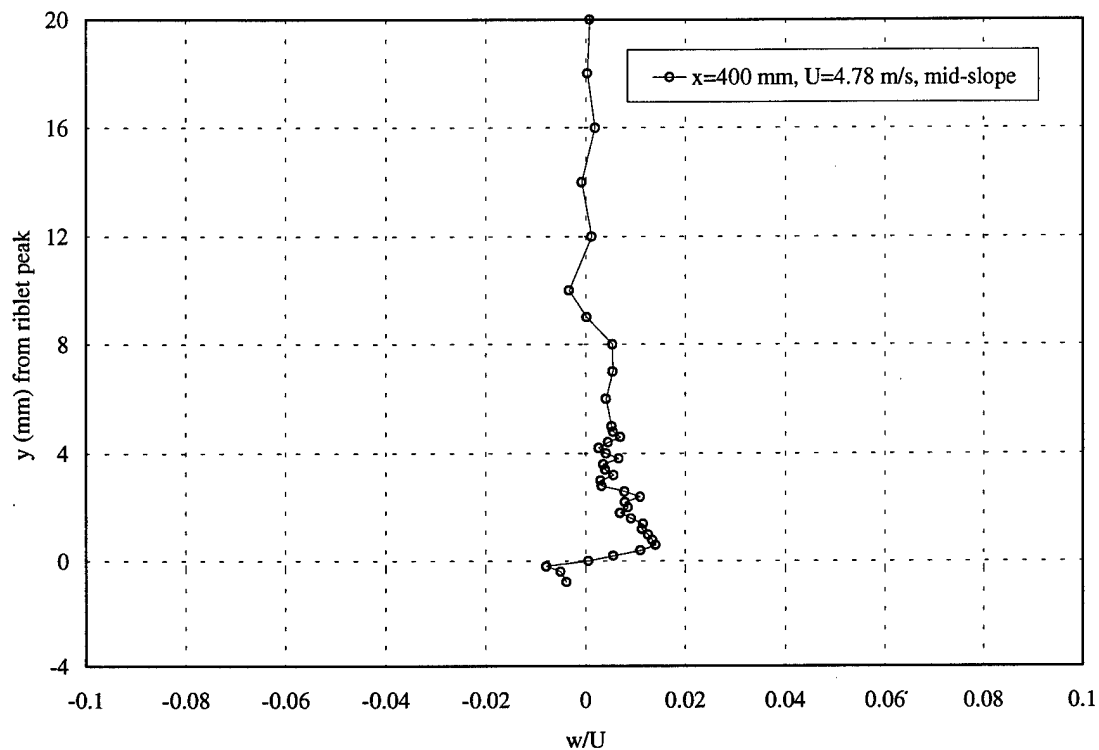
Figure 51. w profile, normal direction, riblet, APG, 400 mm, mid-slope
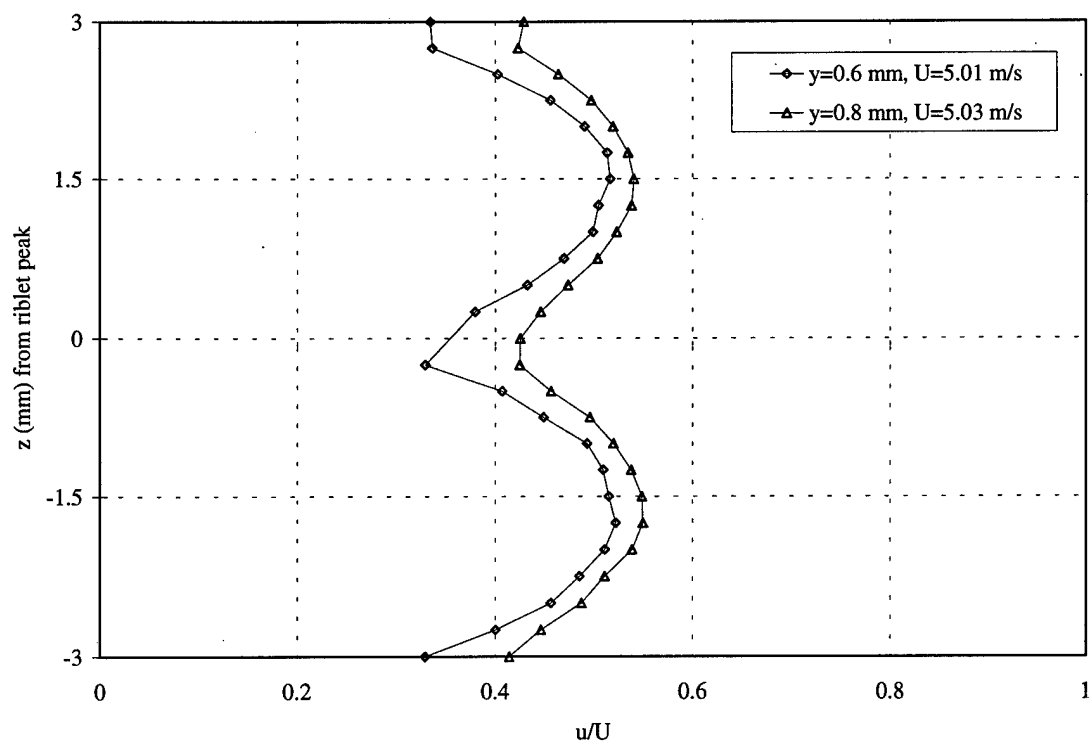
Figure 52. u profile, spanwise direction, riblet, APG, 200 mm
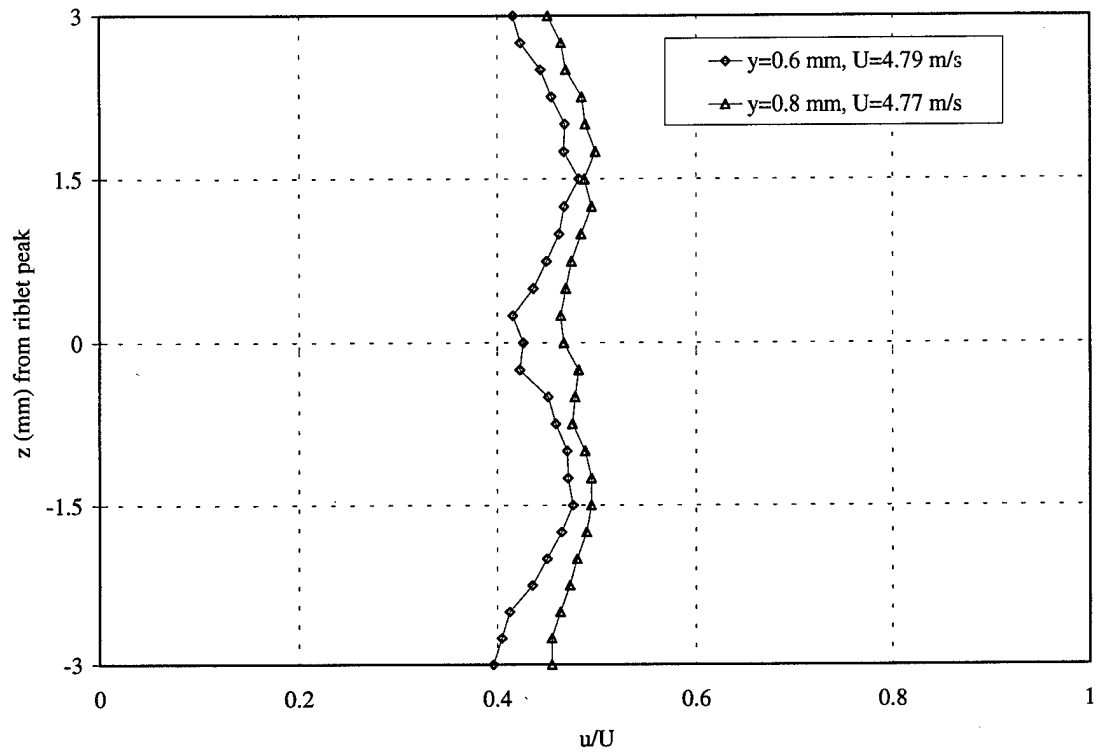
Figure 53. u profile, spanwise direction, riblet, APG, 400 mm
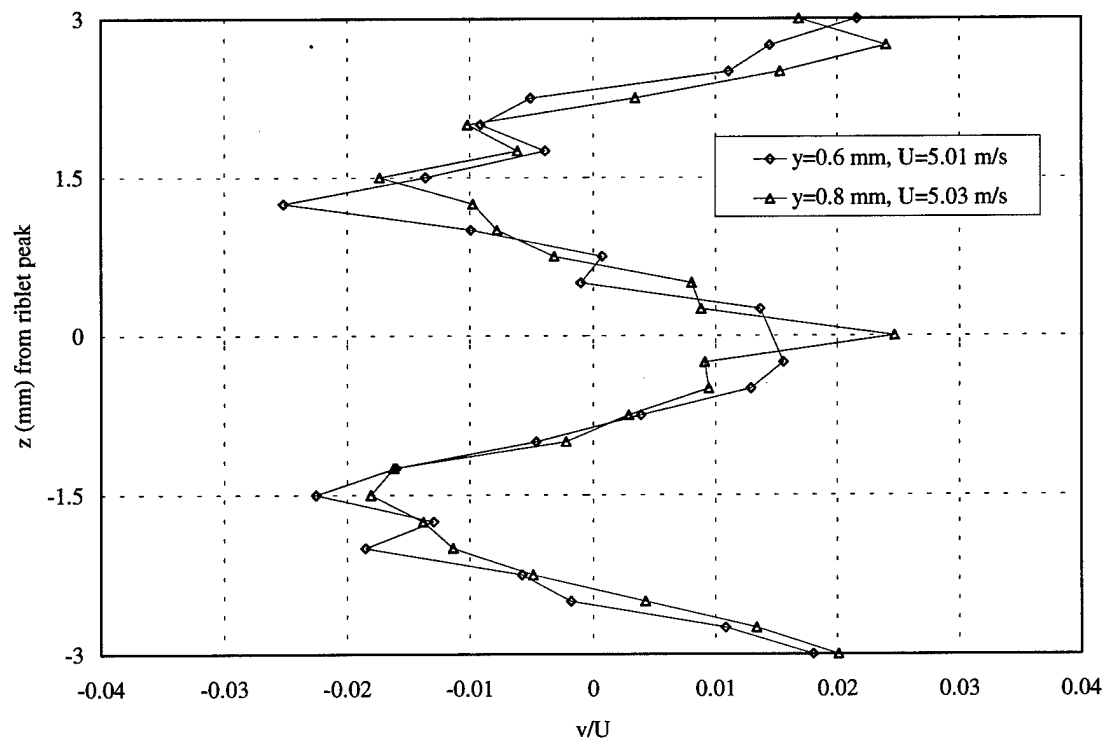
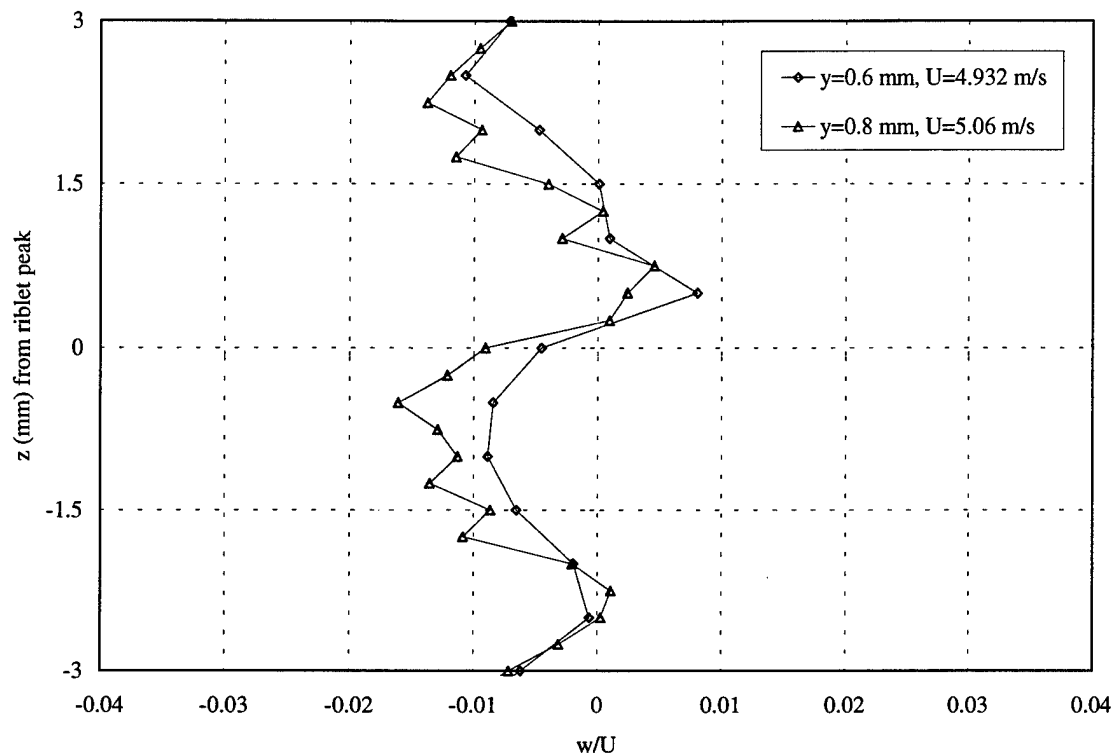Figure 54. v profile, spanwise direction, riblet, APG, 200 mm
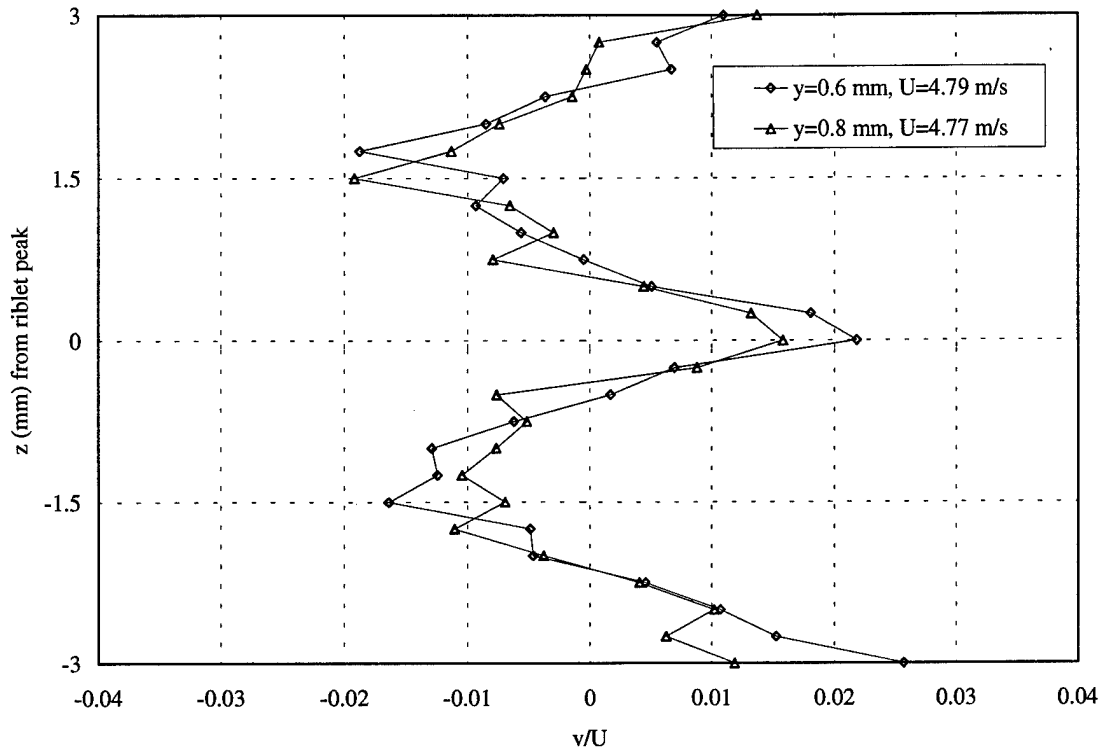
Figure 55. v profile, spanwise direction, riblet, APG, 400 mm
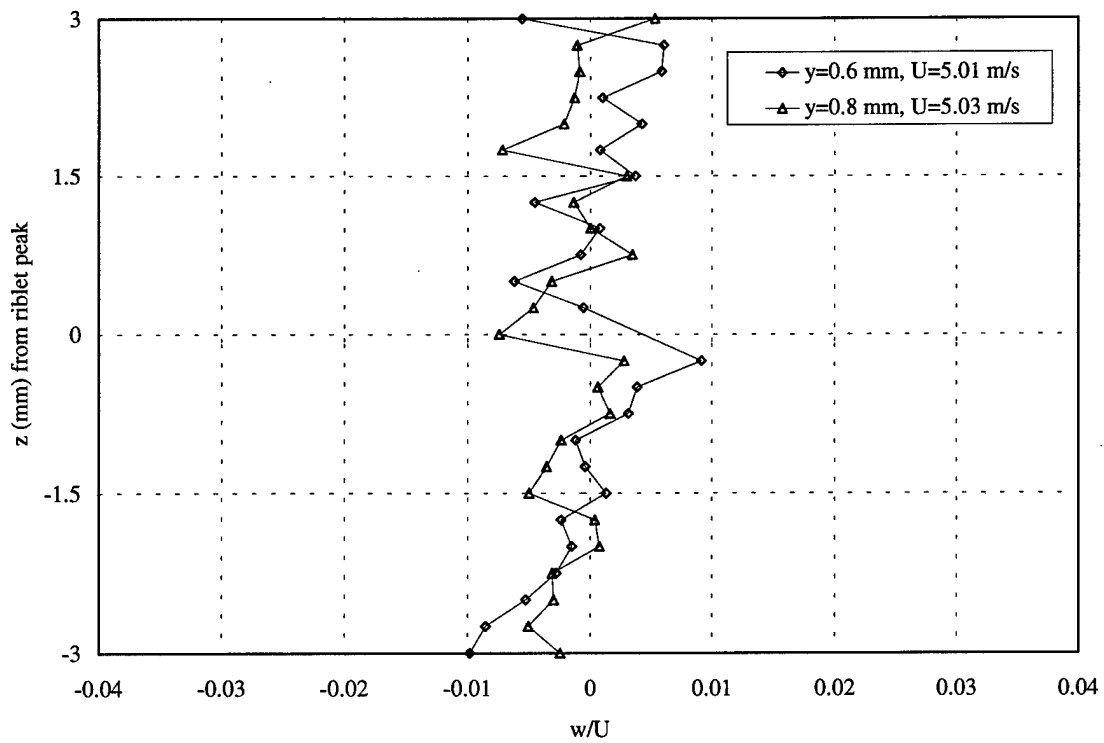
Figure 56. w profile, spanwise direction, riblet, APG, 200 mm
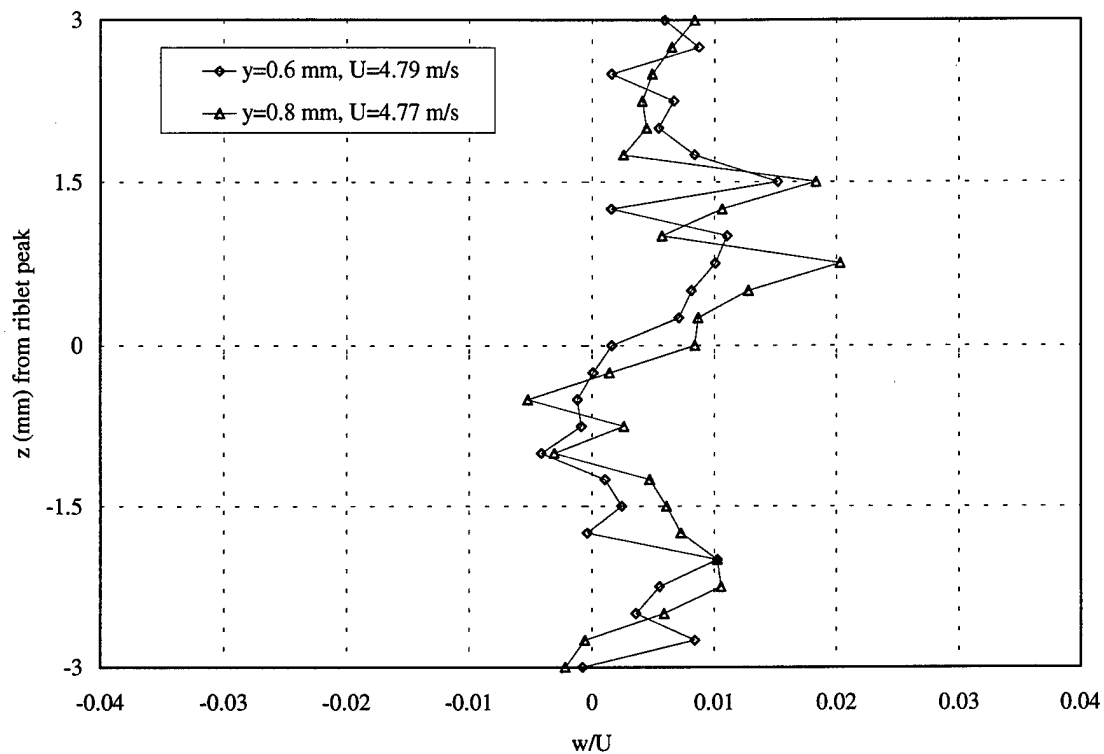
Figure 57. w profile, spanwise direction, riblet, APG, 400 mm

Table 3. Test Apparatus

Component	Model
Mass Flow Regulator	Grove Model 83
Control Regulator	Grove Model 829 Pilot
Feedback Pressure Gage	American Inst. Corp. 25 x 0.25 psi
Particle Generator	TSI Model 9306 6-jet atomizer
Laser (Argon-Ion)	Ion Laser Technology Model 5500A-00
Laser beam safety cover	DANTEC 60X33
Laser alignment plate	DANTEC 9055X9551
Transmitter	DANTEC FiberFlow® 60X41
Beam Manipulators (x6)	DANTEC 60X24
Laser power meter	Coherent Fieldmaster Power/Energy Meter
1-D Laser Probe	DANTEC 60X60
1-D Probe Support	DANTEC 60X361 (3 axis adjustable)
2-D Laser Probe	DANTEC 60X61
2-D Probe Support	DANTEC 60X361 (1 axis adjustable)
Beam Expanders (x2)	DANTEC 55x12
Main Aperture Optics (x2)	600 mm focal length lenses
Color Separator	DANTEC 55X35
Photomultipliers (x3)	DANTEC Photomultiplier 57X81
BSA1 (514.5 nm)	DANTEC 57 N 20 Enhanced
BSA2 (488 nm)	DANTEC 57 N 35 Enhanced slave
BSA3 (476.5 nm)	DANTEC 57 N 35 Enhanced slave
Computer	Gateway 2000 486DX/33
Traverse	DANTEC 55X81

Appendix B: Impacts of the Air Filter

The cleanliness of the air filter significantly impacted the flow regulator's ability to create and maintain test conditions. Unfortunately, this fact was not fully appreciated until late in the project. Consequently, the original filter, which consisted of several stacked coffee filters, was used in all tests except the riblet, APG case. With this filter, steady flow was difficult to achieve for an extended duration. Typically, no more than one hour of testing would pass before a upstream pressure fluctuation or drop occurred that changed flow velocity and subsequently required a test re-start. At the time, these upstream pressure fluctuations were thought to be a normal occurrence during BLRF operation. This situation was further exacerbated by low data acquisition rates.

Late in the project, an abrupt significant degradation in available mass flow rate made the required 5 m/s test section inlet velocity impossible to achieve. As part of the subsequent investigation, the filter joint was disassembled. The original filter was found clogged with rust particles. The movement of these rust particles on the upstream face of the filter is believed to be the cause of the previously observed upstream pressure fluctuations that resulted in unsteady flow in the test section. Replacement of the filter increased the maximum steady flow test section inlet velocity from 5.0 m/s to 6.5 m/s.

The filter change also increased the flow regulator's ability to dampen upstream pressure fluctuations since the regulator no longer had to be at its maximum setting to create a 5 m/s test section inlet velocity. Typical upstream pressure fluctuations for a steady flow condition were approximately ± 6.9 kPa (± 1 psi). Observation of feedback pressure, a direct indicator of steady flow in the test section, showed that the flow

regulator easily damped this level of fluctuation. During every observed upstream pressure fluctuation with a fresh filter, feedback pressure held constant. With the original filter, a ±6.9 kPa (±1 psi) upstream pressure fluctuation would cause a slight, but noticeable change in feedback pressure and thus an unsteady flow condition in the test section. As a result of the increased damping capability obtained with a fresh filter, steady flow could be maintained in the test section almost indefinitely. This significantly reduced the number of required test re-starts.

Filter replacement required close monitoring of upstream pressure during the establishment of test conditions. For the maximum flow regulator setting, a clean filter allowed the BLRF to pass all the flow from the air supply's compressors and produced a continuous drop in upstream pressure. This was not possible with the original filter without excessive venting. A drop in upstream pressure below 468.8 kPa (68 psi), as unfortunately discovered early in the project, damaged the compressors.

Appendix C: Stilling Chamber and Test Section Leveling

As part of the initial hardware configuration, the stilling chamber and the test section were leveled and aligned with each other. This was accomplished to ensure that inlet flow was parallel to the test plate riblets. Parallel flow eliminated undesirable spanwise and normal velocity components and thus ensured vortex formation was not artificially hindered or accelerated.

To level the stilling chamber, the horizontal surface of the test section mounting flange was leveled. This surface was assumed to be parallel to the chamber's outlet flow. Leveling was accomplished by the adjustment of the feet of the chamber until the measured inclinations in the streamwise and normal directions were equal to or less than 0.01°. Inclination measurements were taken with a digital inclinometer. To prevent excessive structural loads on the diffuser cone during this process, the inlet plumbing joints were disconnected.

Test section leveling was accomplished with the adjustment of the test section support stand's legs. Only the test section bottom plate was installed for this process. Streamwise and normal inclinations of the bottom plate were reduced to 0.05° or less. It was impossible to completely eliminate all inclinations since the bottom plate was not completely flat. Periodic checks through the course of the project showed that the test section and stilling chamber required no additional adjustments to ensure flow parallel to the test plate riblets.

A TSI 6-jet atomizer was chosen as the seeding particle generator for this experiment. Two factors influenced this decision. First, the Rosco fog generator initially used to generate seeding particles failed to produce acceptable data acquisition rates and data quality despite the fact that Rothenflue (1996) successfully used a similar device. Variation of the type and brand of fog fluid used with the fog generator failed to produce any changes in rates or quality.

The second reason for the use of the TSI 6-jet atomizer was the fortuitous observation that the LDA system could acquire quality data with no seeding particles injected into the flow. This was the result of the water, rust and compressor oil particles normally present in the flow produced by the AFIT shop air system. This observation led to the conclusion that the characteristics of the seeding particles produced by the fog generator were at least partly responsible for the unacceptable rates and quality. The significant increases in data quality and acquisition rates observed after the switch in seeding particle generators verified this conclusion.

It is of interest to note that Rothenflue (1996) originally considered the TSI 6-jet atomizer for flow seeding. He, however, was unable to achieve acceptable data acquisition rates with the device. Rioux (1996) indicates that Rothenflue (1996) used flow visualization oil with the atomizer that tended to dissipate quickly. In addition, the cascade facility's blower port was the particle injection location used by Rothenflue (1996). This location was far upstream of the test section and resulted in thorough mixing of the particles with the flow prior to entry into the test section. These two factors

are believed to be the reasons behind the poor acquisition rates Rothenflue (1996) observed with the atomizer.

The atomizer provided maximum freestream data acquisition rates for the 514.5 nm, 488.0 nm and 476.5 nm wavelengths of approximately 250 Hz, 50 Hz and 50 Hz, respectively. Unfortunately, these peak rates are 4 to 5 times less than those observed by Rothenflue (1996). The differences in available laser power between the two experiments, as discussed in Appendix F, Reduced Laser Power Levels, are believed to be the underlying factor for the reduced acquisition rates. Combined with the improvement achieved with the change in particle generators, it is believed that nominal laser power would have produced data acquisition rates far in excess of those observed by Rothenflue (1996).

As part of the initial hardware configuration process, the laser was aligned with the centerline of the mounting bench. This was required to facilitate proper beam entry into the transmitter for maximum transmitted beam intensity. A DANTEC alignment plate with a hole in the same plane as the centerline of the bench was used for this process. The feet of the laser were adjusted until the laser's output beam passed through the hole in the alignment plate. A more detailed discussion of the procedure can be found in the FiberFlow® User's Guide. Periodic alignment checks through the course of the project showed that no additional adjustments were required.

Transmitter alignment consisted of three main steps. The first step was to minimize laser power output. Although transmitter alignment is a normal and well-documented part of the initial LDA system configuration process, minimization of laser power was not explicitly required. Minimum laser power prevented damage to the ends of misaligned fibers, prevented operator eye injury from bright reflections at the alignment port and allowed precise alignment of the transmitter in less than five minutes. Laser power was minimized with counter-clockwise rotation of the laser power control potentiometer located on the laser head. Repeated clicking of the potentiometer indicated minimum power. Initial alignment attempts at full power, with the accompanying intense alignment port reflections, took significantly longer with less assurance of precise results and greater risk to the operator's eyesight.

The second step in the process was to configure the transmitter for alignment. This was accomplished with a switch on top of the transmitter. This switch, when moved

to the reference set-up position, shifted a translucent glass pane with a transparent glass alignment port into the transmitter's input aperture. The switch also deactivated the transmitter Bragg cell and altered the internal beam path so that the input beam was reflected from the far end of the transmitter back to the entry port.

The last step in the process was to adjust the transmitter position and orientation with respect to the input beam from the laser. Proper alignment of the transmitter was achieved when the reflected beam coincided with the input beam in the transparent alignment port. This was verified visually and required the removal of the transmitter beam shield. Adjustment of the transmitter's position and orientation was accomplished with the five lateral and vertical thumb wheels located on the transmitter's base.

The input aperture end of the transmitter was adjusted first so that the input beam passed through the center of the transparent glass alignment port. This ensured that the input aperture end of the transmitter was correctly aligned. In conjunction with this step, the transmitter was rotated about its longitudinal axis until its lateral inclination matched that of the optical bench. A digital inclinometer was used to measure the lateral inclination of the bench and the transmitter.

After the input aperture end of the transmitter was properly aligned, the opposite end of the transmitter was adjusted until the internally reflected beam was centered on the transparent alignment port. The five thumb wheels were then locked into place and the beam shield re-installed. Periodic checks during the project showed that no additional transmitter alignment adjustments were required.

As a part of the initial hardware configuration process, the available laser power was measured and maximized. Two methods were used to measure laser power. The first was a direct measurement of the overall, approximate power of the laser output beam. This required removal of the transmitter beam shield and the placement of the power meter sensor head in line with the laser output beam. The power meter is programmed for a particular wavelength; in this case 500 nm was chosen. Weissman (1996) indicated that approximately 80% of the laser's output power could be measured at this wavelength. This method yielded only an approximation of the true output power level since the output beam consisted of several coincident wavelengths different from 500 nm. The measured power of the laser from various sources is shown in Table 4.

Table 4. Laser Power Levels.

Source	Method	Laser Power (mW)
Rothenflue (1996)	Direct Measurement	300
Luker (1995)	Direct Measurement	275
Dement (1996)	Direct Measurement	215
Dement (1996)	Laser Head Voltage	225
Weissman (1996)	Direct Measurement	185

Measurement of the DC voltage potential across the laser voltage test jacks on the laser head was the second method. According to Thompson (1996), the variation of voltage across the test jacks is linear with laser power output, with the constant of proportionality for this linear relationship equal to 0.0166 VDC/mW. DC voltage

potential was measured with a digital multi-meter. The results of this method are also shown in Table 4. This method was used to daily monitor laser output power.

As indicated by the data in Table 4, the laser could not produce its nominal 300 mW power level. The major result of reduced laser power was a drop in data acquisition rates of almost two orders of magnitude compared to those routinely obtained by Rothenflue (1996). The nominal acquisition rate obtained by Rothenflue (1996) for the 514.5 nm wavelength was up to 1000 Hz. Despite the fact that the same seeding particle generator, hardware coincidence filtering and seeding material were initially used along with higher signal gains and PM tube voltages, the maximum freestream data acquisition rate for the 514.5 nm wavelength for this project was initially less than 50 Hz. Maximum freestream data acquisition rates for the 488 nm and 476.5 nm wavelengths were initially less than 10 Hz. These rates were unacceptable given the thousands of bursts (1000-2000) required for each of the hundreds of test locations combined with the initial inability to maintain steady flow for an extended duration.

A significant amount of time and effort was invested to uncover the source of the reduced laser power. Extensive testing and consultation with Weissman (1996), Rothenflue (1996) and Thompson (1996) revealed that the laser's internal mirrors were contaminated with particulates. This was verified on-site by Weissman (1996). Further research revealed that the laser had failed to achieve its nominal power level for at least one year prior to this project (Luker, 1995). In retrospect, the contamination of the laser's mirrors and subsequent reduced power level was inevitable since the air-cooled unit was used extensively in projects where large amounts of particles were deposited directly into laboratory air.

Three courses of action were pursued to correct the power deficiency: refurbishment, replacement and optimization. Refurbishment of the laser was not accomplished due to the unavailability of funds (discovery of the deficiency coincided with the end of the fiscal year). A water-cooled, 5 W argon-ion laser at the USAF Flight Dynamics Laboratory was identified as a possible replacement unit. However, the unit was non-functional and its power supply and cooling system could not be readily supported by the AFIT laboratory. The final option was to maximize the output of the laser and seek other methods to boost data acquisition rates. This option, while eventually successful, did consume a significant amount of project time.

The first step in the optimization process was to maximize laser power output. This was accomplished with laser mirror re-alignment and beam-walking, as described by Thompson (1996). Mirror re-alignment refers to the adjustment of the mirrors in the front and rear ends of the laser head in order to correctly align them with each other and maximize power output. Beam-walking refers to the movement of the aligned mirrors so that the beam exits the laser head correctly. Movement of the laser mirrors for both of these procedures was accomplished with the two Allen screws located on each end of the laser head. To prevent mirror damage, care was taken not to turn the screws more than 90°. Both processes were complete when a maximum output power was achieved. Unfortunately, neither process resulted in any overall increase in laser power.

Despite the fact that mirror re-alignment and beam-walking did not result in an increase in overall power, these techniques were useful in the redistribution of power between the three wavelengths. Through redistribution, Weissman (1996) was able to increase the power of the weak, 476.5 nm wavelength by approximately 10%. The

capability to redistribute power had been previously observed. Due to the use of Rosco fog fluid as the seeding particle material at the time, however, the initial redistribution resulted in no increase in data acquisition rates. With the change to olive oil as the seeding material, Weissman's (1996) power redistribution resulted in increased data acquisition rates for all three wavelengths. This innovative power redistribution scheme to increase data acquisition rates was not presented in any of the DANTEC user's guides.

The peak freestream data acquisition rates observed with the redistribution of laser power were approximately 100-200 Hz for the 476.5 nm and 488 nm wavelengths and 300-600 Hz for the 514.5 nm wavelength. These rates were still significantly less than those of Rothenflue (1996) and frequent test re-starts were common due to the inability to maintain steady flow for an extended duration. In addition, the peak rates tended to degrade significantly with time as well as with proximity to the test plate surface.

Appendix G: Beam Focusing, Tuning and Balancing

Beam focusing, tuning and balancing was required to ensure the maximum, balanced power for each wavelength pair was transmitted through the measurement probes to the probe volume. Each of the six beams were focused, tuned and balanced daily as well as after transmitter alignment. Daily focusing, tuning and balancing was required to compensate for misalignments and the associated power losses caused by thermal effects on the FiberFlow® components. The tuning process is discussed thoroughly in the FiberFlow® User's Guide. Focusing and balancing, however, are only briefly mentioned in the user's guide. The need to accomplish these two activities daily was derived from discussions with Rothenflue (1996) and Weissman (1996) and through observations in the laboratory.

Since it was a relatively coarse adjustment to beam intensity, beam focusing was always accomplished first. Focusing was accomplished with the focusing ring on each fiber plug. Due to focus sensitivity and focusing ring stiction, focusing was generally accomplished by rotation of the focusing ring in one direction only, typically counterclockwise. The focusing process was complete once the intensity of each beam had been maximized. Beam intensity was measured at the measurement probe output with a power meter programmable to individual wavelengths.

After beam focusing, each beam was tuned with its set of manipulator knobs. Each knob was adjusted, in turn, until maximum beam intensity was achieved. The knobs were adjusted in a circular pattern with the lower pair of knobs adjusted first. As discussed in the FiberFlow® User's Guide, the lower pair of knobs controlled the entry

location of the beam into the fiber and the upper pair of knobs controlled the beam in-coupling angle. Typically, several repetitions of the pattern were required to achieve maximum power.

During daily beam tuning, laser output power was left at its maximum value. For beam tuning after transmitter alignment, however, laser power was initially minimized. This was done to avoid fiber end damage from initial beam and fiber misalignment. Also, the manipulator knobs were reset to their neutral position for tuning that immediately followed transmitter alignment. A scribed line on the knob body indicated the neutral position.

After tuning was completed, beam focusing was re-accomplished for each beam. If no significant increases in power were observed, the focusing and tuning process was complete. If significant power gains with beam focusing were observed, beam tuning was accomplished again. This process was repeated until no further gains in individual beam power were observed.

After focusing and tuning, beam balancing was accomplished. For the 514.5 nm (green) and 488.0 nm (blue) pairs, this was simply the process of de-focusing the maximum strength beam of each wavelength pair to match the power level of the weaker beam. This was accomplished with the focusing rings. Typically, the two beams of each pair were easily balanced to within a $\pm$ 0.02 mW difference. This was well within the $\pm$ 20% recommended by Weissman (1996).

Power balancing for the 476.5 nm (purple) wavelength pair was more involved. This pair had the lowest power levels and was the critical factor for data acquisition rates with the hardware coincidence filtering scheme employed in this experiment. Instead of

de-focusing with the focusing rings, the power levels for this pair were balanced with the transmitter's Bragg cell. Rotation of the Bragg cell power potentiometer, located on the side of the transmitter, transferred power between the shifted and unshifted beams for all three wavelengths. This method produced higher balanced power levels for this pair than would have been possible with the de-focusing process. The approximate 10% increase in balanced power for the 476.5 nm (purple) pair, as discussed in Appendix F, Reduced Laser Power Levels, resulted in higher data acquisition rates for all three wavelengths as a consequence of the coincidence filtering option employed. In general, daily power balancing required little, if any, Bragg cell adjustment.

Note that the initial power balancing of the 476.5 nm (purple) beam pair with the Bragg cell resulted in a transfer of power between the shifted and unshifted beams of the remaining two beam pairs. To ensure that power balancing for the 476.5 nm pair did not adversely affect the other two pairs, fiber plugs were initially swapped between manipulators so that the direction of power transfer required for the 476.5 nm (purple) pair would result in power transferred to the weak beam for all three beam pairs. This swapping of plugs was accomplished only once since the differences in beam intensity between the shifted and unshifted beams was mainly due to line losses downstream of the plugs. This original technique of fiber plug swapping to maximize available data acquisition rates was not presented in the FiberFlow® User's Guide.

The results of the focusing, tuning and balancing processes are shown in Table 5 along with those of Rothenflue (1996) and Luker (1995). Despite the comparatively low values and the difficulty of data acquisition with power levels near 2.0 mW (Rothenflue, 1996), acquisition of quality data, albeit slow, was successfully accomplished. Note that

137

reduced power levels did not adversely affect Luker (1995) due to his use of the 2-D off-axis, forward-scatter mode and no hardware coincidence filtering. As a result of this system configuration, Luker's (1995) probe volume was roughly 120 times larger than that of this experiment and consequently produced significantly larger data acquisition rates.

Table 5. Maximum, Balanced Beam Powers.

Wavelength (nm)	Balanced Power Output (mW)	Luker (1995) Power Output (mW)	Rothenflue (1996) Power Output (mW)
514.5 (green)	6.5	8.0	30
488 (blue)	7.3	6.75	12
476.5 (purple)	2.2	2.0	3

The decreased power levels shown in Table 5 are also indicative of high line losses. Comparisons of power levels at the manipulator exit ports with power levels at the measurement probe outlets showed line losses of up to 78%. Weissman (1996) indicated that line losses of 50% should be expected. Damage from movement of the system between laboratories, violation of minimum optical fiber bend radii and crushing loads (feet and equipment) is believed to be the cause of the higher-than-expected line losses.

Appendix H: Probe Volume Formation

The goal of the probe volume formation process was to precisely intersect the focal points of the three pairs of beams. A well-formed probe volume, as discussed in the BSA User's Guide, maximizes data acquisition rates. Maximum rates were critical to the quick, efficient acquisition of data, especially in light of the steady flow problems initially encountered. On a daily basis, fine tuning adjustments of the probe volume were required to compensate for misalignments induced by thermal effects on FiberFlow® components. Initial formation of the probe volume, as discussed below, was a more involved process.

The first step in the initial formation of the probe volume formation was to position the probes on the traverse optical bench. To produce a symmetrical configuration with a 70° included angle, each probe was rotated on its base 35°. A symmetrical probe configuration was recommended by the FiberFlow® User's Guide. With these angles set, the probes were positioned on the traverse bench so that the intersection of the beams roughly coincided.

The next step in the initial formation process was to properly orient the beam pairs. The desired orientation included the 476.5 nm (purple) pair and the 514.5 nm (green) pair in the test section streamwise-normal, or x-y, plane. This beam orientation was recommended by the FiberFlow® User's Guide and used by Rothenflue (1996). In this orientation, velocity components measured by these two wavelengths could be transformed and combined to determine velocity components in the test section's normal and streamwise directions. Also, this orientation simplified the post-acquisition

coordinate transformation process, produced the best velocity resolution according to the FiberFlow® User's Guide and, due to the design of the 2-D probe, resulted in the direct measurement of test section spanwise velocity components by the 488.0 nm (blue) beam pair. To achieve this orientation, the probes were rotated within their retaining collars until the green and purple beams were parallel with the surface of the bottom plate. The surface of the bottom plate, as discussed in Appendix C, <u>Stilling Chamber and Test Section Leveling</u>, was parallel with the flow direction.

After the beams had been properly oriented, the translation, rotation and tilt micrometer knobs on the 1-D probe base were used to move the beam focal points until they were verified visually to be coincident. Visual observation of the focal points was done through the transparent test section top plate from a vantage point above the test section. Visualization of the beams and their focal points was accomplished by the injection of a small amount of seeding material into the test section.

Fine tuning adjustments of the probe volume with the micrometer knobs was accomplished with the actual seeded test flow. For this process, the measurement volume was positioned in the test section freestream and the Burstware® program was programmed to display real-time data acquisition rates for each wavelength. To observe real-time rate changes from micrometer knob adjustments, a monitor connected to a closed circuit television camera focused on the Burstware® personal computer screen was positioned near the traverse bench. The measurement volume was adjusted with the micrometer knobs until maximum data acquisition rates were obtained for each wavelength. To facilitate precise adjustments, the micrometer knob bearing surfaces were lubricated and the knobs were turned with a small pair of pliers.

The fine tuning process consisted mostly of adjustments in the z direction with the tilt micrometer knob. Daily visual checks of the probe volume showed that little or no adjustment of the focal points in the x or y directions was required. Since fine tuning consisted mostly of adjustments in the z direction, the process was virtually a binary phenomenon. The probe volume was either precisely aligned and acceptable data acquisition rates were observed or the probe volume was misaligned and one or more wavelengths had a zero data acquisition rate.

The probe volume formation process differed substantially from that of Rothenflue (1996). For this experiment, the procedure consisted only of coarse alignment of the beams focal points verified with visual observation and fine tuning with the seeded test flow. Rothenflue (1996) followed a three step process: coarse alignment with a 100 micron hole, fine tuning with a seeded flow outside the test section and additional fine tuning in the actual test flow.

Initial experimentation showed that coarse alignment by the passing of all six beams through a 100 micron hole did not guarantee the coincidence of the central focal point area of the three pairs. The coincidence of this central area for the three pairs was required for an optimal probe volume. As a consequence, this introductory tool, as the 100 micron hole was described by Weissman (1996), was not used past the early familiarization stage of the project. Initial probe volume formation was accomplished more accurately and much faster with visual observation and subsequent adjustments. Weissman (1996) concurred with this method and indicated it as standard practice for initial probe volume formation.

Fine tuning outside the test section, as done by Rothenflue (1996), was initially accomplished. For this process, both the 6-jet atomizer and a humidifier were used. No benefit beyond that achieved with probe volume fine tuning in the actual seeded flow was observed. It is believed that this process proved beneficial for Rothenflue (1996) due to his use of a different seeding particle material.

Appendix I: Traverse Positioning and Alignment

As part of the initial set-up of the test hardware, the traverse was positioned and aligned with the test section. The traverse was placed on the right side of the test section as shown in Figure 3. The traverse was positioned so that the probe volume could traverse the entire length and width of the sidewall laser slot without mechanical interference with the BLRF.

Alignment of the traverse with the test section consisted of the rotation of the traverse on its base until the traverse x-axis, as shown in Figure 3, coincided with that of the test section. This coincidence ensured that the actual data acquisition point was close to the desired point and reduced the complexity and error in the transformation of raw velocity data. Coincidence of the axes was achieved when the traverse bench was parallel to the edge of the bottom plate. Previous dial caliper measurements showed that the edge of the bottom plate was parallel to the test plate surface. The parallel condition between the traverse bench and bottom plate edge was assessed with a template at several stations along the length of the test section. Periodic checks showed that the traverse required no additional adjustments after initial alignment was accomplished.

The Burstware® program used a variety of programmable parameters to control the data acquisition process. These parameters were divided into optical, front panel, soft key and program sets. The significant parameters for each set are discussed below, in turn. A thorough description of all acquisition parameters can be found in the DANTEC BSA User's Guide and the Burstware 2.0® User's Manual.

The optics parameters described the probe optics and were used to convert Doppler bursts into raw velocity data. Table 6 shows the optics parameters and their respective values used for this experiment. Wavelength refers to the unshifted wavelength processed by each BSA. Beam separation refers to the distance across the probe front lens between the two beams of a single color. The focal length parameter refers to the focal length of the probe front lens. A thorough description of how these parameters were used to convert frequency data to velocity data can be found in the DANTEC BSA User's Guide.

Table 6. Optics Parameters.

Parameter	BSA #1	BSA #2	BSA #3
Wavelength (nm)	514.5	488.0	476.5
Beam separation (mm)	38	38	38
Focal length (mm)	600	600	600

The front panel parameters controlled BSA data processing. Specifically, these parameters controlled the range of measurement, the frequency of sampling and signal amplification. The values and interaction of the front panel parameters were highly

critical to the acquisition of quality velocity data. Values for each parameter were derived from expected flow velocities, the data quality observed in real-time velocity histograms and from preliminary tests conducted in the on-axis probe configuration. The typical values used in this experiment are shown in Table 7. The complete set of front panel parameters is thoroughly discussed in the DANTEC BSA User's Guide.

Table 7. Front Panel Parameters.

Parameter	BSA #1	BSA #2	BSA #3
Velocity units	m/s	m/s	m/s
Bandwidth (m/s)	$\cong 8$	$\cong 8$	$\cong 8$
Center frequency (m/s)	$\cong 2$	$\cong 0$	$\cong 2$
Record length (# of samples)	32	32	32
Signal gain (dB)	45	45	45
High voltage (V)	1800	1800	1800

Velocity units refer to the units used by the BSAs to describe the center frequency (f_c) and bandwidth (BW) for velocity processing. Available choices for units were m/s and kHz. Units of m/s were used until a software problem that caused unprompted f_c changes required a switch to kHz. No source of the software problem was discovered.

Bandwidth refers to the frequency range over which each BSA processed signals from potential Doppler bursts. As recommended by Rothenflue (1996), BW was kept as small as possible and selected to encompass the expected velocity range. Smaller bandwidths produced greater frequency resolution and more precise velocity measurements, as discussed in the DANTEC BSA User's Guide. The 8 m/s BW shown in Table 7, combined with the appropriate f_c, spanned the entire expected range of flow velocities for this experiment. Although little spanwise velocity variation was expected,

145

this BW was also used for BSA #2. (Recall that, as discussed in Appendix H, <u>Probe Volume Formation</u>, BSA #2 measured spanwise velocities directly.) This was done in order to have the common record interval (R_i) for all three BSAs required for hardware coincidence filtering. The interaction of BW with record length (N) and R_i is discussed in Appendix L, <u>Interaction of Bandwidth and Record Length</u>. The BW value, which varied slightly between BSAs due to wavelength differences, was not typically changed in the course of the experiment.

Center frequency refers to the location of the center of the selected bandwidth. Combined together, BW and f_c defined the measurement range as discussed in the DANTEC BSA User's Guide. Since the streamwise velocity was expected to vary between 0 to 5 m/s as a function of y, f_c for BSA #1 and BSA #3 was set at approximately 2 m/s. This produced a measurement range from -2 m/s to 6 m/s. The center frequency of BSA #2 was set at 0 m/s, the expected median spanwise velocity component. The values of f_c, which varied slightly between BSAs due to wavelength differences, remained constant during the project because of the small range of flow velocities at all data acquisition locations.

The record length, N, is defined as the number of samples of a potential Doppler burst taken by each BSA. As recommended by the DANTEC BSA User's Guide, a large N was desired to increase the accuracy of the velocity measurements through increased sampling of Doppler bursts. Choices for N were limited by the Burstware[®] program to 8, 16, 32 and 64. An N value of 32 was typically used based on observed signal quality, the recommendations of Rothenflue (1996) and the effects on R_i caused by the selection of BW, as discussed in Appendix L, <u>Interaction of Bandwidth and Record Length</u>.

Signal gain and PM tube high voltage settings were used to obtain the best possible signal for processing, as discussed in the DANTEC BSA User's Guide. Specifically, these two parameters were used to enhance data quality and reduce signal noise. Signal gain refers to the amplification of PM tube voltage signals. The available signal gain range was from 0 to 53 dB. High voltage refers to the voltage applied to the PM tubes. The available range was from 0 to 2040 V. The gain and high voltage levels required to obtain quality data were interdependent, highly variable and depended in part on available laser power and probe volume alignment. The appropriate values were determined in preliminary tests prior to data acquisition for each profile. Simply stated, the largest possible signal gain and high voltage settings were used that would not produce excessive noise in the real-time histograms. Large values increased data acquisition rates at the expense of data validation. Data validation was reduced by the excessive amplification of noise signals that triggered the burst detectors too often, as stated in the DANTEC BSA User's Guide.

As a result of the low laser power available for this experiment, gain and PM tube high voltage values significantly higher than those of Rothenflue (1996) were typically used. In fact, PM tube high voltage settings above the 1500 V level had to be used to obtain quality data. Weissman (1996) stated that with nominal laser power, PM tube high voltage above 1500 V should not be required. Unfortunately, the larger values for these settings effectively increased the size of the probe volume since scattered light from particles outside the probe volume could be detected (Rothenflue, 1996). A larger probe volume resulted in greater particle location ambiguity and larger calculated turbulence levels.

The soft key parameters controlled the operational mode of each BSA. The

typical soft key parameter values used for this experiment are shown in Table 8. These

parameters are thoroughly discussed in the DANTEC BSA User's Guide.

Table 8. Soft Key Parameters.

Parameter	BSA #1	BSA #2	BSA #3
Timer clock	Master	Slave	Slave
Coincidence mode	Master	Master	Master
Collection mode	Burst	Burst	Burst

The timer clock parameter specified the BSA to be used as the reference timer for

the time-tagging of detected Doppler bursts by each BSA. Time-tagging was required in

order to employ hardware and software coincidence filtering. Time-tagging was made

possible through a timing cable that connected the three BSAs. For this experiment, the

internal clock of BSA #1 was selected as the reference timer.

Coincidence mode refers to the hardware coincidence filtering setting of each

BSA. Hardware coincidence filtering was the method through which the synchronization

of potential Doppler bursts from each BSA was checked. Three hardware coincidence

filtering settings were available: master, slave and private. For the master setting, a

potential Doppler burst was processed only if all BSAs with master coincidence settings

had simultaneously detected it. In this mode, data processing for all BSAs stopped as

soon as one BSA no longer detected the burst. In the slave coincidence setting, a BSA

was triggered to process data whenever a potential Doppler burst was detected by a BSA

in the master coincidence mode. A BSA programmed for the private coincidence setting

processed potential Doppler burst data independently.

Each hardware coincidence setting had advantages and drawbacks. With all three BSAs in the master coincidence mode, high confidence was obtained that the processed velocity data originated from a particle inside the probe volume. Consequently, particle location ambiguity was reduced and spatial resolution was enhanced. Due to the required synchronization of bursts from each BSA, this coincidence setting unfortunately produced the lowest data acquisition rates. The slave coincidence setting was useful for the triggering of data acquisition for a BSA with low acquisition rates. This mode produced higher acquisition rates than the master coincidence mode but the confidence that the location of the particle was within the probe volume was reduced. The private coincidence mode provided the highest data acquisition rates and the least confidence that the velocity data originated from a particle within the probe volume.

With the exception of preliminary tests, the data in this experiment was acquired with each BSA in the master coincidence mode. This mode was chosen, despite the reduced data acquisition rates, for reduced particle location ambiguity and the need for high spatial resolution within the boundary layer. The reduced data acquisition rates of this mode were exacerbated by low laser power levels, especially those of the 476.5 nm wavelength beam pair. The low power level of this pair, because of the synchronization requirement of the master coincidence mode, produced lower acquisition rates for the other two wavelengths. The redistribution of laser power to increase power to the 476.5 nm pair, as discussed in Appendix F, Reduced Laser Power Levels, compensated for this effect by increasing data acquisition rates for all wavelengths despite the loss of power to the remaining two wavelengths.

Although not explicitly a part of the soft key parameter set, the data validation filtering option was closely linked to BSA data processing. Validation was the process by which the simultaneous tracking of two particles in the probe volume was eliminated. As with Rothenflue (1996), the system was programmed to acquire validated data only. The simultaneous tracking of two particles was eliminated with a comparison of a potential Doppler burst's maximum intensity to its two smallest minima. A burst was validated and considered to be from only one particle when its local maxima was at least four times as great as its local minima. The validation process is further discussed in the DANTEC BSA User's Guide. Because of the need for higher signal gain and PM tube high voltage and the accompanying amplification of noise, low laser power resulted in lower validation percentages than observed by Rothenflue (1996).

The collection mode refers to the method used by the BSAs to collect data. There were three modes available: continuous, controlled dead time and burst. These modes are discussed thoroughly in the DANTEC BSA User's Guide. The continuous mode is useful for flows with a high density of seeding particles where at least one particle is expected to be within the probe volume at any time. The controlled dead time mode is useful for specific types of flows with low particle densities, such as reacting flows. The burst mode was also intended for sparsely seeded flows. In this mode, however, the BSAs process data on all detected bursts. As with Rothenflue (1996), the density of seeding particles within the flow for this experiment was relatively small and the burst option was the optimal collection mode choice.

The program parameters specified the amount and kind of data recorded at each acquisition location. Typical values of these parameters for this experiment are shown in Table 9.

Table 9. Program Parameters.

Parameter	BSA #1	BSA #2	BSA #3
Time-out (s)	20-300	20-300	20-300
Number of bursts	2000	2000	2000
Velocity	Yes	Yes	Yes
Transit time	Yes	Yes	Yes
Arrival time	Yes	Yes	Yes

Time-out refers to the amount of time for which a given BSA would record data at a given acquisition location. The selected value was based on the observed data acquisition rates at a given location and the number of bursts to be collected. Values varied from 20 seconds in the freestream to 300 seconds near the test surface. Relatively large time-outs were required near the test surface due to the associated lower flux of seeding particles. Larger time-out values also had to be used near the end of each profile, even for locations in the freestream, because of the depletion of seeding particles initially contained in the seeder plenum.

The Burstware® program was observed to operate in two different modes with regards to the time-out parameter. First, data acquisition at a given location would cease for a given BSA when either its time-out value was reached or its required number of bursts was collected. In the second mode, data acquisition at a given location would cease for all BSAs once the time-out value was reached or the required number of bursts was collected for any BSA. The Burstware® program vacillated between these two

modes without operator input. This phenomenon was attributed to a software error and complicated data acquisition due to the inequity of data acquisition rates between the three BSAs.

Number of bursts refers to the number of potential Doppler bursts to be collected by each BSA at each data acquisition location. Typically, 2000 bursts were collected at each acquisition location compared to the 1000 per location collected by Rothenflue (1996). The number of bursts was increased based on Rothenflue's (1996) recommendation and to ensure a more statistically meaningful number of bursts collected given the difficulties with time-out and low validation percentages.

The remaining parameters in Table 9 refer to the kind of data to be recorded for each potential Doppler burst. The recording of velocity data for each burst enabled the calculation of mean velocity components at a given location along with the corresponding turbulence intensities. The arrival times of particles in the probe volume and the transit times of each particle across the probe volume were required for residence time weighting. Arrival time was the time at which a potential Doppler burst first met the criteria for burst detection, as discussed in the DANTEC BSA User's Guide. Transit time was the time between the arrival time and the time at which the burst could no longer be detected. As a result of the burst detection thresholds, as discussed in the DANTEC BSA User's Guide, the recorded transit time did not necessarily correspond to the amount of time that the particle was actually inside the probe volume.

Appendix K: Coordinate System Transformation

The optical-to-test section matrix was used by the Burstware® program to convert the velocity components measured in the non-orthogonal probe coordinate system to the orthogonal test section coordinate system. To determine the values in the optical-to-test section transformation matrix, the matrix was decomposed as the multiplication product of two less complicated transformation matrices. These matrices were the laser probe alignment matrix and the optical misalignment matrix. The laser probe alignment matrix transformed the velocity components measured in the probe coordinate system to the traverse coordinate system. The optical misalignment matrix transformed the velocity components from the traverse coordinate system to the test section coordinate system. The test section and traverse coordinate systems are shown in Figure 3 and the probe coordinate system is shown in Figure 5.

The terms in the laser probe alignment matrix were found through the development of the transformation relationship between the probe and traverse coordinate systems. With the transformation techniques of Kramer (1995), this relationship was found to be

$$\left\{ \begin{matrix} x_p \\ y_p \\ z_p \end{matrix} \right\} = [C] \left\{ \begin{matrix} x_t \\ y_t \\ z_t \end{matrix} \right\} \tag{22}$$

where the transformation matrix, [C], is

$$[C] = \begin{bmatrix} -\cos(\theta_2) & \sin(\theta_2) & 0 \\ 0 & 0 & -1 \\ -\cos(\theta_2)\cos(\theta_1+\theta_2)- & \sin(\theta_2)\cos(\theta_1+\theta_2)- & 0 \\ \sin(\theta_2)\sin(\theta_1+\theta_2) & \cos(\theta_2)\sin(\theta_1+\theta_2) & \end{bmatrix} \tag{23}$$

153

The subscripts p and t in Equation (22) refer to the coordinate directions in the probe and traverse coordinate systems, respectively. The quantities θ_1 and θ_2, as shown in Figure 5, are the angles included between the probes and the traverse system y-axis. With Equations (22) and (23), the velocity components in the probe and traverse coordinate systems are thus related with

$$\begin{Bmatrix} u_t \\ v_t \\ w_t \end{Bmatrix} = [C]^{-1} \begin{Bmatrix} u_p \\ v_p \\ w_p \end{Bmatrix} \tag{24}$$

The matrix $[C]^{-1}$ is the laser probe alignment transformation matrix.

An important consideration in the numerical values used in the laser probe alignment matrix was the location of the shifted and unshifted beams with respect to the flow direction. Where possible, the beams for each wavelength pair were oriented so that the shifted beam lay in the positive flow direction and the unshifted beam lay in the negative flow direction. This orientation produced velocity signs consistent with observed flow behavior. Due to the need to swap fiber plugs to maximize balanced beam intensities as described in Appendix G, Beam Focusing, Tuning and Balancing, this orientation was not possible for the 488.0 nm wavelength pair. As a result, the sign of the term in the second row, third column of [C] was reversed for actual data reduction.

The terms in the optical misalignment matrix were found through the development of the transformation relationship between the test section and traverse coordinate systems. With the transformation techniques of Kramer (1995), this transformation relationship was found to be

$$\begin{Bmatrix} x \\ y \\ z \end{Bmatrix} = [D] \begin{Bmatrix} x_t \\ y_t \\ z_t \end{Bmatrix} \qquad (25)$$

where the transformation matrix, [D], is

$$[D] = \begin{bmatrix} \cos(\alpha)\cos(\beta) & \cos(\beta)\sin(\alpha) & \sin(\beta) \\ -\sin(\alpha)\cos(\gamma) - \sin(\gamma)\cos(\alpha)\sin(\beta) & \cos(\alpha)\cos(\gamma) - \sin(\gamma)\sin(\alpha)\sin(\beta) & \sin(\gamma)\cos(\beta) \\ -\sin(\alpha)\sin(\gamma) - \cos(\gamma)\cos(\alpha)\sin(\beta) & -\cos(\alpha)\sin(\gamma) - \cos(\gamma)\sin(\alpha)\sin(\beta) & \cos(\gamma)\cos(\beta) \end{bmatrix} \qquad (26)$$

The test section coordinate directions in Equation (25) are denoted by the lack of subscripts. The α, β, and γ angles define the rotation about the z_t, y_t, and x_t axes, respectively, to arrive at the test section coordinate system. The values for these angles were calculated from the coordinates of three non-collinear points located on the riblet test surface. With Equations (25) and (26), the velocity components in the traverse coordinate system were related to the velocity components in the test section coordinate system with

$$\begin{Bmatrix} u \\ v \\ w \end{Bmatrix} = [D] \begin{Bmatrix} u_t \\ v_t \\ w_t \end{Bmatrix} \qquad (27)$$

where the matrix, [D], is the optical misalignment matrix.

Equations (24) and (27) were combined to produce the optical-to-test section matrix. The velocity components in the probe coordinate system of Equation (24) were substituted for the traverse coordinate system velocity components in Equation (27) and simplified to yield

155

$$\begin{Bmatrix} u \\ v \\ w \end{Bmatrix} = [D] \begin{Bmatrix} u_t \\ v_t \\ w_t \end{Bmatrix} = [D][C]^{-1} \begin{Bmatrix} u_p \\ v_p \\ w_p \end{Bmatrix} = [E] \begin{Bmatrix} u_p \\ v_p \\ w_p \end{Bmatrix} \qquad (28)$$

From this equation, the optical-to-test section matrix was extracted as the matrix multiplication of the laser probe alignment and optical misalignment matrices:

$$[E] = [D][C]^{-1} \qquad (29)$$

The terms in the optical-to-test section matrix, [E], were calculated with Mathcad 5.0+®

and the measured values of θ_1, θ_2, α, β, and γ. Equation (29) also corrects the

typographical error in matrix multiplication order of the optical misalignment and laser

probe alignment matrices in Rothenflue (1996). Prior to correction, this typographical

error resulted in significant negative impacts during early data reduction efforts.

Appendix L: Interaction of Bandwidth and Record Length

The interaction of bandwidth (BW) and record length (N) was critical to the acquisition of quality velocity data. Specifically, the choices for BW and N had a direct bearing on the value of the total amount of sampling time, or record interval (R_i). The record interval (R_i) was related to BW and N through a series of relationships:

$$R_i = NT_s \qquad (30)$$

In this equation, the sampling time, T_s, is the inverse of the sampling frequency (f_s):

$$T_s = \frac{1}{f_s} \qquad (31)$$

From the BSA User's Guide, each BSA calculated the sampling frequency based on the selected BW:

$$f_s = 1.5(BW) \qquad (32)$$

Combined together, Equations (30) through (32) yield

$$R_i = \frac{N}{1.5(BW)} \qquad (33)$$

From this equation, it can be seen that the large N and small BW needed for accurate velocity measurements required a relatively long total sampling time.

The total sampling time available, however, was constrained by the transit time of the fastest particles. Specifically, the record interval was limited because sampling could not continue after a given particle had exited the probe volume. Sampling past the particle exit time caused noise to be generated at the end of the particle's data record, which subsequently caused the record to be rejected. Thus, an excessively large R_i caused rejection of data from high speed particles and artificially biased the calculated

mean velocities toward a smaller value. To avoid this problem, N and BW were chosen so that R_i was no greater than 75% of the expected transit time of the fastest particle (Rothenflue, 1996). Several combinations of BW and N were available that could meet this R_i constraint. Preliminary tests were conducted to find an appropriate BW and N combination that produced quality velocity data.

Vita

Capt Franklin L. Dement, Jr. was born on 04 November 1966 in Memphis, Tennessee. He graduated from Milton High School in Milton, Florida in 1984 and then entered undergraduate studies at the University of Alabama in Tuscaloosa, Alabama. He graduated with a Bachelor of Science of Aerospace Engineering degree in May 1989. He received his commission on 13 May 1989 through the Air Force Reserve Officer Training Corps.

Capt Dement's first assignment was to Space Systems Division, Los Angeles AFB. There, he held a variety of jobs: project officer in the SDI Directed Energy Weapons SPO, launch vehicle component structural analyst in the select Education with Aerospace program, and test manager, launch vehicle engineer and mission management branch chief in the Space Test and Transportation SPO's Small Launch Vehicle (Pegasus) program. In May 1995, Capt Dement entered the School of Engineering, Air Force Institute of Technology. After AFIT, he was assigned to McClellan AFB. There, he served as an A-10A structures engineer, an advanced composites structures engineer and an A-10A and F-117A aircraft battle damage repair engineer.

Permanent Address: 1109 Berryhill Rd
                             Milton FL 32570

REPORT DOCUMENTATION PAGE

Public reporting burden for this collection of information is estimated to average 1 hour per response, including the time for reviewing instructions, searching existing data sources, gathering and maintaining the data needed, and completing and reviewing the collection of information. Send comments regarding this burden estimate or any other aspect of this collection of information, including suggestions for reducing this burden, to Washington Headquarters Services, Directorate for Information Operations and Reports, 1215 Jefferson Davis Highway, Suite 1204, Arlington, VA 22202-4302, and to the Office of Management and Budget, Paperwork Reduction Project (0704-0188), Washington, DC 20503.

1. AGENCY USE ONLY (Leave blank)	2. REPORT DATE March 1999	3. REPORT TYPE AND DATES COVERED Master's Thesis

4. TITLE AND SUBTITLE
EFFECTS OF PRESSURE GRADIENTS ON TURBULENT BOUNDARY LAYER FLOW OVER A FLAT PLATE WITH RIBLETS

5. FUNDING NUMBERS

6. AUTHOR(S)

Franklin L. Dement, Jr., Capt, USAF

7. PERFORMING ORGANIZATION NAME(S) AND ADDRESS(ES)

Air Force Institute of Technology
2750 P Street
WPAFB OH 45433-7765

8. PERFORMING ORGANIZATION REPORT NUMBER

AFIT/GAE/ENY/99M-9

9. SPONSORING/MONITORING AGENCY NAME(S) AND ADDRESS(ES)
Dr. Richard Rivir (937) 255-8212
AFRL/PRTT
Bldg 18, Area B
WPAFB OH 45433-7251

10. SPONSORING/MONITORING AGENCY REPORT NUMBER

11. SUPPLEMENTARY NOTES
Dr. Paul I. King (937) 255-3636
paul.king@afit.af.mil

12a. DISTRIBUTION AVAILABILITY STATEMENT

Approved for public release; distribution unlimited

12b. DISTRIBUTION CODE

13. ABSTRACT (Maximum 200 words)

The Air Force Institute of Technology Boundary Layer Research Facility test section was modified to create controlled non-zero streamwise pressure gradients. The capability of the modified facility to reproduce theoretical laminar boundary layer velocity profiles and to create a self-preserving flow with an adverse streamwise pressure gradient was verified with three-dimensional laser Doppler anemometry. The effects of streamwise adverse and favorable pressure gradients on turbulent boundary layer flow characteristics (velocity profiles, turbulence and skin friction) and vortex formation over a flat plate with riblets at low speed ($U = 5$ m/s) were studied.

Normal and spanwise velocity profiles for both pressure gradients showed the presence of paired counter-rotating vortices nested within the riblet valleys. These flow structures increased drag and significantly altered near-wall flow compared to a smooth plate turbulent boundary layer. The adverse pressure gradient tended to degrade these vortices as the flow progressed.

14. SUBJECT TERMS
riblets, boundary layer, counter rotating vortices, LDA system, skin friction, adverse pressure gradient

15. NUMBER OF PAGES
175

16. PRICE CODE

17. SECURITY CLASSIFICATION OF REPORT Unclassified	18. SECURITY CLASSIFICATION OF THIS PAGE Unclassified	19. SECURITY CLASSIFICATION OF ABSTRACT Unclassified	20. LIMITATION OF ABSTRACT UL